The Dissertation Committee for Youthachack Landry Khounlavong
certifies that this is the approved version of the following dissertation:

Coarse-Grained Simulations to Predict Structure and Properties of Polymer Nanocomposites

Committee:

Venkat Ganesan, Supervisor

Isaac C. Sanchez

Benny D. Freeman

Thomas M. Truskett

Pengyu Ren

Coarse-Grained Simulations to Predict Structure and Properties of Polymer Nanocomposites

by

Youthachack Landry Khounlavong, B.S.; Ch.E.

Dissertation

Presented to the Faculty of the Graduate School of

The University of Texas at Austin

in Partial Fulfillment

of the Requirements

for the Degree of

Doctor of Philosophy

The University of Texas at Austin

December 2010

Dedicated to my loving parents, Phanh and Evelyn Khounlavong

Acknowledgments

I would like to first thank my adviser, Prof. Venkat Ganesan, for the guidance and education he has provided me during my time at The University of Texas at Austin. The completion of this work would not have been possible without his knowledge, direction and support. Also, I would like to thank him for the opportunity to attend multiple conferences and allowing me to collaborate with scientists at the U.S. Army Research Laboratories; these were invaluable experiences. Prof. Ganesan, I truly appreciate everything you have done for me and your patience. Thank you for this opportunity! I'd also like to thank Prof. Thomas Truskett, Prof. Isaac Sanchez, Prof. Benny Freeman, and Prof. Pengyu Ren for serving on my dissertation committee and for their advice.

I'd also like to thank the following for funding support, this research could not have been undertaken without it: the Robert A. Welch Foundation, the U.S. Army Research Office and the American Chemical Society Petroleum Research Fund. In addition, I'd like to thank the University of Texas at Austin graduate school office for a fellowship they granted me in my last year of graduate school. I also want to thank the Texas Advance Computing Center for their supercomputing resources and support.

I'd like to thank Dr. Jan Andzelm for giving me the opportunity to work alongside him at the U.S. Army Research Laboratories (ARL). Also, many thanks to Chris Rinderspacher and Tanya Chantawansri for kindly sharing their office during my stay at ARL, helping me get acquainted with the facilities and showing me around Maryland. I'd also like to thank Dr. Marc Nyden for

allowing me to visit NIST, and for the informative discussions we had.

Within the chemical engineering department, there are many people I'd like to thank. First of all, Dr. Victor Pryamitsyn, thank you for the discussions on polymer physics, general advice and many memorable quotes. I'd also like to thank Dr. Manas Shah for the afternoon breaks at Jamba Juice to calm my nerves when my programs were going awry. I'd like to thank David Trombly, Chetan Mahajan, Thomas Lewis, and Dr. Paresh Chokshi as well as the above members of the Ganesan group for a friendly research group environment. Outside of this group of people, I'd like to thank: Dr. Bill Krekelberg for answering my many computer programming questions and the debates over the best college football teams; Prof. Jeetain Mittal for his contagious enthusiasm for science and daily research discussions; Dr. Devina Pillay and Dr. Jason Cheung for their witty humor; and "T" Stockman and Kay Costales-Swift for their general help. Also, a special thanks to the The Lunch Group (Dr. Manas Shah, Dr. Mehul Patel, Dr. Gaurav Goel, Dr. Guarav Gupta, Dr. Amogh Prabhu, and Dr. Reken Patel) for the daily jokes, advice and all around good times. I'd like to also acknowledge and thank my friends and teammates who were on the 2009 graduate division intramural champion basketball team: Ross Dugas (the captain), Jason Davis, Bryan McCloskey, Joe Dekker, Hao Ju, David Kryscio, and Collin Beal.

A big part of my success I attribute to the unselfish support of my family, and I would like to whole-heartedly thank them all for this. Mom and Dad, though there are many things to thank you for, I'd like to thank you most for your love, support and trust. I would not be where I am today without your care and guidance, and delicious food that always kept me full. Thank you a million times over! Candice, thank you for being a very caring sister;

your thoughtfulness has always been touching. Jeremy, my brother, thanks for all the laughs when I needed them the most. My cousins (who I really consider my older brothers and sisters) Mo, Phoutie, Eck, Jimmy and Viviane for teaching me many life lessons; your determination and achievements always pushed me to be better and I was fortunate to have you to look up to. My little cousin, Tyler, for teaching me how to snowboard and keeping me current on all dance moves. A very important thank you to my grandmothers, the late Mrs. Ha Khounlavong and Ms. Freda Salyers, for being an inspiration to me throughout my life. I'd also like to thank the following family members for their love and support: Uncle Khamla and Aunt Pheth Khounlavong, Uncle Khone and Aunt Py Niravong, Uncle Jay and my late Aunt Nyla Anderson, and Uncle Doug and Aunt Maggie Salyers.

I'd also like to thank some friends who made living in Austin a memorable time, to say the least: Reken Patel, for being a great roommate and an excellent finder of restaurants serving delicious eats. Andy and Misty Heitsch, for opening up their home to me and their tasty weekend cookouts. Stephanie Freeman, for her numerous witty comments that always kept me laughing and her delicious banana bread, and for allowing me to occupy her living room when I had no place to stay during the last couple of months of finishing my thesis. Mehul Patel, for inspiring me to run the Austin Marathon and putting me in my place by consistently defeating me in every footrace. Carlos Alcala, for all the humorous stories you narrated. Bryan McCloskey, Brent Bregenzer, Tracy Hawkins, Dan Barad, Bob Tsai and Colin Hessel for providing way too much fun on the weekends. Many thanks to Amy Tam, Tammy Tam, Lily Wong and ZY Ho for helping make Austin home initially, and the friendship that followed. I also want to thank Jay Bacrania, Nancy Tran, Natalie Whit-

ney, Nisita Wanakule, Justin Smith, Coleman and Colette McCormick, and Tu-Hien Le for their sincere friendship since the good ol' days in Florida.

To The University of Texas at Austin Chemical Engineering Department, thank you for having me! It was a fantastic experience.

<div align="right">

YOUTHACHACK LANDRY KHOUNLAVONG

</div>

The University of Texas at Austin

December 2010

Coarse-Grained Simulations to Predict Structure and Properties of Polymer Nanocomposites

Publication No. _____

Youthachack Landry Khounlavong, Ph.D.
The University of Texas at Austin, 2010

Supervisor: Venkat Ganesan

Polymer Nanocomposites (PNC) are a new class of materials characterized by their large interfacial areas between the host polymer and nanofiller. This unique feature, due to the size of the nanofiller, is understood to be the cause of enhanced mechanical, electrical, optical, and barrier properties observed of PNCs, relative to the properties of the unfilled polymer. This interface can determine the miscibility of the nanofiller in the polymer, which, in turn, influences the PNC's properties. In addition, this interface alters the polymer's structure near the surface of the nanofiller resulting in heterogeneity of local properties that can be expressed at the macroscopic level.

Considering the polymer-nanoparticle interface significantly influences

PNC properties, it is apparent that some atomistic level of detail is required to accurately predict the behavior of PNCs. Though an all-atom simulation of a PNC would be able to accomplish the latter, it is an impractical approach to pursue even with the most advanced computational resources currently available. In this contribution, we develop (1) an equilibrium coarse-graining method to predict nanoparticle dispersion in a polymer melt, (2) a dynamic coarse-graining method to predict rheological properties of polymer-nanoparticle melt mixtures, and (3) a numerical approach that includes interfacial layer effects and polymer rigidity when predicting barrier properties of PNCs.

In addition to the above, we study how particle and polymer characteristics affect the interfacial layer thickness as well as how the polymer-nanoparticle interface may influence the entanglement network in a polymer melt. More specifically, we use a mean-field theory approach to discern how the concentration of a semiflexible polymer, its rigidity and the particle's size determine the interfacial layer thickness, and the scaling laws to describe this dependency. We also utilize molecular dynamics and simulation techniques on a model PNC to determine if the polymer-nanoparticle interaction can influence the entanglement network of a polymer melt.

Contents

List of Tables

List of Figures

Chapter 1

Introduction

Polymer nanocomposites (PNC) are a relatively new class of composite material synthetically made first in the late 1980s by Toyota, who ultimately created a timing belt case with superior mechanical properties and enhanced resistance to thermal expansion [1, 2]. Since this discovery, a general definition for PNCs has been adopted: a polymer, polymer blend, or copolymer embedded with *nanofillers* that have at least one dimension on the length scale of nanometers. These nanofillers can be spherical nanoparticles, carbon nanotubes, nanoplatelets, or nanofibers.

There is no shortage of scientific evidence claiming PNCs with outstanding mechanical [3, 4, 5, 6, 7], electrical [8, 9, 7], thermal [7, 10], barrier [11, 12, 13, 14, 7, 10], and optical [15] properties. Typically, such enhancements in properties manifest at low loadings of nanofiller. This is in contrast to traditional polymer composites (TC) where usually the filler (having dimensions on the order of microns) is required at much larger loadings to accomplish desired property augmentation. Needless to say, the use of PNCs would be advantageous in many applications. However, the synthesis and processing of PNCs are not trivial. In fact, the main culprit preventing the use of PNCs is

the agglomeration of the nanofillers, which generally leads to poor property enhancements, if any at all. Such affinity between nanofillers can even occur at low loadings [16]!

Experimentalists have fortunately developed methods to increase the miscibility of the nanofiller in the polymer. For instance, the surface of nanofillers have been altered by chemically attaching aliphatic chains to make it more hydrophobic and, thus, more likely to disperse [17, 18, 19, 20]. Another strategy is to apply an external field (stress, electrical, etc.) to promote the orientation of nanofillers in the host polymer [4, 21, 22]. There are even instances when the two constituents naturally interact favorably with one another to generate nanofiller dispersion [23]. These strategies have led to many advanced materials, though have not allowed for any general methods or rules for creating a PNC material with its maximized enhancements at an optimal, low-weight loading. Fortunately, this provides an opportunity for computational methods. Towards this, a method for predicting the nanofiller dispersion and, then, the PNC properties is a prerequisite.

One objective of this thesis is to develop a coarse-graining method to accurately predict nanoparticle dispersion in a polymer melt. The use of different length scales here is required due to the length scales spanned by the PNCs. Specifically, the atomistic interactions at the interface between nanoparticle and polymer govern the dispersion of the nanoparticle at an intermediate length scale (*mesoscale*) between atomistic and macroscopic. Moreover, the incorporation of such atomistic interactions in a full simulation of a PNC is not

pragmatic with the computational resources currently available *nor is* a theoretical framework able to accomplish such a feat for a realistic system. Thus, our idea is to extract the essential structural information of the polymer at the atomistic scale to use at the mesoscale so that a full PNC simulation is permissible and nanofiller dispersion is predictable. We accomplish this by developing a coarse-graining procedure for polymer-nanoparticle melt mixtures that accurately takes into account the polymer-nanoparticle interaction and accurately predicts nanoparticle dispersion while requiring less computational resources.

The *second objective of this thesis* is to predict, from a mesoscopic resolution, the rheological response of a PNC to oscillatory strain. This is a challenge considering that experiments effect such strains at a macroscopic scale. Fortunately, simulations of material under strain can be accomplished at the mesoscale due to previously developed simulation techniques [120, 121, 123]. However, the challenge here is what dynamic information needs to be translated from the atomistic scale to the mesoscale to account for dynamical effects at the mesoscale. This was achieved by utilizing coarse-grain interactions derived from our equilibrium coarse-graining procedure for predicting PNC structure alongside dissipative forces in dissipative particle dynamics (DPD) simulations. These dissipative forces were linked to characteristic relaxation times that can be derived from atomistic simulations.

The *third objective of this thesis* is to shed light on the impact the polymer-nanoparticle interface has on particular microscopic and macroscopic

3

quantities. This interface does not only affect dispersion of the nanoparticle, it also influences how the polymer packs near the surface of the nanoparticle. This leads to variations in local properties of the polymer relative to the bulk and is termed the *interfacial layer*. This is an important aspect of PNCs due to their large interfacial area (relative to TCs), which can result in large volume fractions of heterogeneity that, ultimately, can have a pronounced effect at the macroscopic scale. Furthermore, this heterogeneity in local properties can also be caused by confinement of the polymer if the nanofiller concentration becomes high enough, effectively "overlapping" the interfacial layers in the system. This latter point is a critical one, as we discovered that this interfacial layer overlap can also influence nanoparticle dispersion. It is clear the interfacial layer as well as the polymer-nanoparticle interface are key characteristics of PNCs, and are critical to understand their effects.

In the following sections, we go into more detail about our objectives that are achieved in the following chapters. Also, some experimental evidence is provided for the aspects we include in our overall multiscale approach for PNCs. Furthermore, we discuss some of the questions that will be addressed in the rest of the thesis.

1.1 Determining Nanofiller Dispersion and Rheological Properties in Polymer Melts

The surface chemistry between the two constituents of a PNC can promote or inhibit the nanofiller's miscibility at equilibrium. The phase behavior of the PNC can thus be altered by a chemical adjustment of this interface. For instance, Fornes et al. found that by attaching aliphatic chains to the surface of montmorillonite (MMT) and dispersing this altered MMT in Nylon, the dispersion of the MMT could be tuned [17]. More specifically, the altered MMT surface included site attachments of varying number of alkyl chains, effectively changing the grafting density. This detail is important because they discovered that the dispersion depended nonlinearly on the number of alkyl chains attached per site. Such a result indicates that nontrivial surface chemistry can play an important role in determining macroscopic properties. This finding as well as others [18, 19, 20, 23] verifies that accounting for the polymer-nanofiller interaction is required to accurately predict nanofiller dispersion at equilibrium.

There has been theoretical work on the phase behavior of PNCs, helping to elucidate what are the optimal conditions for exfoliation of nanofillers. To accomplish this, polymer reactive interaction site method (PRISM) theory [24, 25, 26], self-consistent field theory (SCFT) [27, 28, 29, 30], and field-theoretic [31] approaches have all been used. However, such studies have been restricted to generic systems that are useful for elucidating physics, but

of no direct help when predicting properties of realistic PNCs. In addition, simulations have also been reduced to such model systems when studying PNC dispersion due to computational constraints [32].

One of the goals of this thesis work is *to develop a coarse-graining method that includes the effects of the polymer-nanoparticle interaction on dispersion.* In this effort, atoms are grouped into coarse-grained units to be represented at a more efficient, but less detailed, *mesoscopic* resolution. More specifically, coarse-grain units composing the polymer chain will represent groups of monomers and the nanoparticles embedded within this coarse-grain polymer are represented as spherical units. Our coarse-grain method generates the effective polymer-polymer, polymer-nanoparticle, and nanoparticle-nanoparticle interactions for this new, coarse description of the PNC. The original polymer-nanoparticle interaction at the atomistic level will be captured in the method with which we coarse-grain these interactions. One challenge to overcome is the multicomponent nature of the PNC and the order in which to coarse-grain the above three interaction types. Also, it is not apparent what is the optimal choice for the number of atoms to be grouped as a coarse-grain unit. Moreover, it is not guaranteed that the resulting coarse-grained interactions be applicable for different nanoparticle volume fractions. Most importantly, the simulations, from which the atomistic information is gathered for input to our coarse-grain method, must be practical in size to execute in a reasonable amount of computational time. More obviously, the coarse-grained interaction must in the end save on required computational resources.

Another strategy for dispersing nanofillers includes how the mixture is processed. This can be accomplished by applying a stress [4] or magnetic [21, 22] field to the PNC. Such an approach is likely to work if the nanofillers remain kinetically trapped in a dispersed state. While this is an important challenge we do no directly address this issue in this work. However, we do augment our coarse-graining method by developing a way to incorporate dynamical effects occurring at the mesoscopic length scale. We aim to validate our method by ensuring that coarse-grained simulations can reproduce the rheological properties of a reference model PNC.

1.2 Interfacial Layer Effects in Polymer Nanocomposites

Not only does degree of nanofiller dispersion directly influence PNC properties, but the interfacial layers around the nanofillers can also become influential at the macroscopic scale. What is more, this layer most likely has a gradient in local properties. The range of this layer can be influenced by the particle and polymer size, polymer and particle concentration, polymer rigidity, and thermodynamic conditions.

Direct experimental measurement of interfacial layer properties is very difficult to obtain. There has been experimental proof of a different phase near nanoparticles by Berriot et al.[33], who revealed a third glassy phase encompassing nanoparticles. In the latter study, they also assumed a gradient

in glass transition temperature near the surface of the nanoparticles, which allowed them to accurately model the mechanical response displayed by rubber embedded with silica nanoparticles [33]. There have been more studies where an interfacial layer has been assumed to explain property trends [34, 35].

While it is difficult with experiments to understand what is exactly occurring at the molecular level near the polymer-nanofiller interface, computational and theoretical approaches do provide insight to this. One and two nanofillers have been simulated in a polymer to determine the structural aspects of the polymer near the surface and in confinement [36, 37, 38]. Similarly, theoretical work has taken a similar one or two nanofiller approach, but have been restricted to model systems of PNCs [39, 40, 41]. Such approaches provide insight not only on the polymer structure at the interface, but also the range of the perturbation away from the nanofiller's surface and a basis from which local properties can be derived from the local structure. In addition, the information obtained from the above approaches have also been fed into continuum models and theories to predict PNC properties [36, 42]. However, these approaches do not attempt to accurately account for nanofiller arrangement, as typically homogeneous dispersion is assumed and not determined from any input from the atomistic scale.

A goal of this thesis is *to provide insight into what influences interfacial layer characteristics as well as how this can affect certain microscopic and macroscopic quantities.* We utilize a mean-field theory approach to discern the dependence of how the interfacial layer's thickness depends upon particle

size, polymer rigidity, and polymer concentration. With this approach, we were able to obtain a scaling dependency of interfacial layer thickness on the latter list of parameters. This approach also provides the local density profile of this interfacial layer, which was used as input to a numerical approach we develop to predict barrier properties of PNCs. We investigate how interfacial layers and their overlap can influence the diffusion of a penetrant in model PNC membranes. Finally, we look at how the polymer-nanoparticle interface, and its resulting interfacial layer, may play a role in determining the entanglement length of a polymer melt.

1.3 Thesis Organization

Chapter 2: Many-body Interactions and Coarse-Grained Simulations of Structure of Nanoparticle-Polymer Melt Mixtures
This chapter present a computational approach for coarse-grained simulations of nanoparticle-polymer melt mixtures. We first examine the accuracy of an effective one-component approach based on a pair interaction approximation to polymer-mediated interactions, and demonstrate that even at low particle volume fractions, the polymer-mediated many-body interaction effects can prove significant in determining the structural characteristics of mixtures of nanoparticles and polymer melts. The origin of such effects are shown to arise from the extent of polymer perturbations resulting from the presence of the nanoparticles. To account for such effects, we propose a new simulation approach which employs a coarse-grained representation of the polymers to

capture the many-body corrections to the polymer-mediated pair interaction potentials. The results of the coarse-grained simulations are shown to be in good quantitative agreement with the reference simulations. The method developed in this article is proposed as a tractable approach to coarse-grain and effect computer simulations of atomistic descriptions of polymer-nanoparticle systems.

Chapter 3:Predicting Rheological Properties of Polymer-Nanoparticle Melt Mixtures

The cause of rheological property enhancements can be attributed to the large interfacial area of PNCs that can influence the dynamics of the polymer near the vicinity of the nanofiller. Taking this into account, we develop a method which augments our equilibrium coarse-graining scheme that predicts nanofiller dispersion by appropriately preserving the dynamical effects that occur at the mesoscale. The challenge here is what atomistic information needs to be translated to the mesoscale. We propose that the relaxation time of the coarse-grained segments comprising the coarse-grained polymer nanocomposite should match the relaxation of the center-of-mass of the group of monomers it is intended to represent. We account for two types of relaxation times in this method: (1) relaxation time in the bulk polymer and (2) relaxation time near the surface of the nanoparticle.

Chapter 4: Equilibrium Characteristics of Semiflexible Polymer Solutions Near Probe Particles

A numerical analysis of the mean-field theory for the structure of semiflexible polymer solutions near spherical surfaces is presented in this chapter. This framework is used to study the depletion characteristics of semiflexible polymers near colloids and nanoparticles. Our results suggest that the depletion characteristics depend sensitively on the polymer concentrations, the persistence lengths and the radius of the particles. Broadly, two categories of features are identified based on the relative ratios of the persistence lengths to the correlation length of the polymer solution. For the limit where the correlation length is larger than the persistence length, the correlation length proves to be the critical length scale governing both the depletion thickness and the curvature effects. In contrast, for the opposite limit, the depletion thickness and the curvature effects are dependent on a length scale determined by an interplay between the persistence length and the correlation length. This leads to nontrivial (numerical) scaling laws governing the concentration and radii dependence of the depletion thicknesses. Our study also highlights the manner by which the preceding features rationalize the parametric dependencies of insertion free energies of small probes in semiflexible polymer solutions.

Chapter 5: Influence of Interfacial Layers upon the Barrier Properties of Polymer Nanocomposites

In this chapter, we present a numerical approach which: (i) Uses a microscopically based polymer model to determine the characteristics of such interfacial layers; (ii) Embeds the so-determined interfacial characteristics into a numerical homogenization procedure which accounts for the overlap of interfacial

layers (approximately) and multibody interactions (exactly). The numerical approach is used to elucidate the influence of polymer matrix stiffness, particle sizes and particle volume fractions upon the penetrant diffusivity properties of PNCs.

Chapter 6 On Entanglements in Polymer Nanocomposites

In this chapter, an investigation is presented of the effects of polymer-nanoparticle interaction and confinement on the entanglement length of a polymer melt. Experimental studies have shown that nanoparticles can influence mechanical properties of which this alteration can be explained by a change in the number of entanglements [43, 44] though this explanation is not conclusive [45]. In an attempt to rationalize this behavior a computationally efficient model polymer nanocomposite is simulated with molecular dynamics to obtain equilibrium structures from which an entanglement length is calculated. The latter calculation is performed via primitive path analysis developed by Everaers and co-workers [46, 47]. The polymer-nanoparticle interaction is varied in an attempt to deduce its influence on the entanglement length of the polymer melt. Also, the nanoparticle volume fraction is changed to induce confinement effects in the system to help elucidate their role in the entanglement network.

Chapter 2

Many-body Interactions and Coarse-Grained Simulations of Structure of Nanoparticle-Polymer Melt Mixtures

2.1 Introduction

Development of nanoscale multicomponent materials such as PNCs involves an interplay of constituent selection, fabrication, processing and performance. A key question in this regard is the manner in which the polymer-polymer, polymer-filler, filler-filler interactions control the structure, dispersion features and the properties of the PNCs. Interest in this issue arises from the fact that experiments have unequivocally confirmed that the structural characteristics of the fillers dispersed in the polymer matrix proves critical in controlling property enhancements in PNCs. For instance, experimental studies have shown the mechanical properties of PNCs filled with clay particles are correlated to the degree of exfoliation or intercalation of fillers.[17, 48] Also, the barrier

properties of PNCs containing clay platelets have been shown to be very sensitive to the dispersion and orientation of the fillers. [20] Similarly, addition of carbon nanotubes have been shown to dramatically enhance polymer conductivities only upon the percolation of the filler in the polymer matrix.[8] It is evident that an outstanding issue for achieving the potential of PNCs for applications is to be able to *apriori* predict the structural characteristics of the fillers dispersed in the polymer.[49, 50]

Theoretical models and computer simulations provide an attractive means to address the interrelationship between the chemical details of the polymer and the filler on the one hand and the macroscopic structure of the filler and properties of the PNC on the other hand. Not surprisingly, a number of theoretical contributions have already addressed many elements of this issue. For instance, the polymer reference interaction site model (PRISM)[51, 52, 53, 54] has been used to study how polymers pack near a hard surface,[55] the effective interactions between nanoparticles,[56, 57, 39, 58] and the phase behavior exhibited of nanoparticle-polymer mixtures.[24, 25] Density functional theories (DFT) have also proved popular,[59, 55, 60] and have been used to study the packing of polymers near surfaces and the interactions between nanoparticles in polymer matrices.[61] On a more coarse-grained level, pioneering theoretical research of Giannelis and Balazs has shed light on the important thermodynamic features governing the structural state of nanofillers dispersed in polymer matrices. Vaia and Giannelis used lattice-based models to suggest that an interplay of polymer entropic and polymer-filler energetic factors determines

the equilibrium state of polymer-filler mixtures.[62, 63] Balazs and coworkers, and other have used a combination of self-consistent field calculations and/or density functional theories to investigate the interactions and phase behavior of plate and rod-like particles in polymer melts and solutions, and delineated optimal conditions for creating stable dispersed composites.[64, 65, 66, 29, 30]

Despite the insights derived from the above studies, successful use of such developments have been limited due to the emphasis of only modeling the physics on a *coarse-grained* scale.[67] Explicitly, in such models, the polymer is typically modeled as a connected sequence of segments, where each segment is understood to represent a collection of molecules or atoms.[68] Moreover, the polymer chain is typically assumed to be flexible and behave as an elastic spring or a Gaussian coil. The particle fillers in such models are represented as hard spherical or anisotropic objects. Thus, the specific chemical identities of the monomers and the fillers are ignored in these approximations. Instead, simpler model interaction potentials are used to characterize the interactions between segments of the polymer and the particle fillers. While insights derived from such models are valuable, there is still a lack of theoretical methods by which one can incorporate features relating to the detailed chemistry of the polymer and its interactions with the fillers (and functionalizers, if any) to predict their interplay in determining the state of dispersion of the nanofillers.

On the other hand, computer simulations coupled with accurate force-field parametrizations[68] may provide a means to quantify the connections between the chemical details of the different components and the filler dis-

persion and property characteristics. However, such a detailed approach is still not tractable due to the length and time scales which span many orders of magnitude in PNCs. Because of this issue, fully atomistic simulations of PNCs have been restricted to situations where there are only one[36] or two[37] fillers in the polymer matrix. While these one or two filler simulations do provide valuable insights into the local structure[36, 37] and dynamics[69, 70, 71, 72] of the polymer near the fillers, direct information on the filler dispersion characteristics is elusive in such approaches.

Many prior researchers have proposed and developed methods of coarse-graining (CG) as a way to enable computer simulations to predict structure and properties of materials while incorporating information at the atomistic level of detail.[73, 74, 75, 76, 77] The idea behind such coarse-graining techniques is to map atomistic (or finer resolution) systems onto a coarser resolution system (i.e. a *mesoscopic* length scale) so as to facilitate simulations and/or models of larger systems over possibly longer time scales and/or with less computational resources. The main task in such coarse-graining schemes is to determine the interactions between the mesoscale units such that they accurately capture the interaction features of the corresponding units at the atomistic scale. Commonly, the latter is ensured by positing that the interactions at the mesoscale level are chosen to either match the structural[74, 77, 78] or the thermodynamic properties[79, 80, 81] or the forces[82, 83] between the corresponding units at the atomistic scale. A variety of studies have detailed application of the above-mentioned CG methods to simple fluids,[84, 78, 85, 75] poly-

16

mer solutions,[86] polymer melts,[74, 87, 88, 89, 90, 91, 92, 93, 94, 95] and lipids.[76, 96, 97, 80, 79, 98]

Unfortunately for PNCs, the body of work on coarse-graining techniques is not as well-developed as it is for pure polymeric systems. Although some preliminary steps have been taken towards developing multiscale methods to link the filler-polymer interactions to the filler morphology in PNCs,[24, 99, 100] to our knowledge, no prior studies have examined the manner in which the above coarse-graining ideas can be adapted or modified to address issues specific to PNCs. Some issues specific to the PNCs are the following:

(i) PNCs are inherently multicomponent, and an outstanding question is the manner (and even the order) in which the different interactions need to be coarse-grained. Related to this feature is that the multicomponent nature brings to fore several length (and time) scales, which include the size of the fillers, the size of the polymers, the length scale over which the interfacial effects of the fillers extend etc. An outstanding question is: what is the appropriate length and time scale over which the physics can be coarse-grained without losing accuracy on the properties of interest?

(ii) Another challenge involved in CGing PNCs is in deciding the minimal amount of atomistic simulations required to obtain the interactions at the mesoscopic level. Current CG methods typically require structural information from atomistic simulations *at the same thermodynamic conditions* as a means for determining the coarse-grained interactions. For PNCs, this would suggest effecting atomistic simulations at the same temperature, density of

polymers and the *volume fraction of fillers*! Since such a task is intractable for PNCs, it is of interest to explore if a more minimal CGed representation derived by using atomistic simulations (containing at most one or two fillers) can still accurately predict the structure of the PNC.

In this work, our objective is to develop a CG method for PNCs that (1) can be parametrized using atomistic simulations; (2) accounts for the multi-component nature of PNCs in a systematic manner; (3) requires only a minimal amount of information as input from atomistic simulations; and (4) accurately predicts filler dispersion using the mesoscale simulations. A crucial ingredient in our work is the validation of the CG proposals by a direct comparison of exact "atomistic" simulation results with results from CG mesoscale simulations. However, since it is intractable to simulate a realistic atomistic description of a PNC to perform such validation tests, we use a simpler system as our "atomistic" model, chosen such that the PNC simulations can be effected at both the atomistic and the mesoscopic levels. Using such a model system, we address the issues detailed above. By validating our algorithm in this chapter, the application of this algorithm to a more realistic system (for which the atomistic predictions cannot be obtained) is straightforward, though we do not attempt this here. As a note, due to our choice of reference system, the algorithm may have to be refined for realistic systems that have intramolecular interactions, which may need to be rigorously accounted for.

Towards the above objective, we first examine the applicability of the simplest CG approach for PNCs, viz., the use of a pair interaction potential

based on an effective one-component approximation. In this methodology, the polymer degrees of freedom are formally integrated out, and consideration is restricted to the particle degrees of freedom which interact by polymer-mediated forces in addition to their bare interactions. While the preceding step can be effected in a formally exact manner[101] it is common to approximate the polymer-mediated forces as a sum of pair interaction forces corresponding to the polymer-mediated potential of mean forces (PMF) deduced at the dilute limit of particle concentrations.[102] While such an approximation renders computer simulations and modeling of PNCs tractable, our results demonstrate that as a consequence of the influence of many-body interactions this approximation fails for PNCs even at low volume fractions.

The above results are used to motivate the new CG approach proposed, which involves a mesoscale simulation involving the fillers along with a CG representation of the polymer molecules. After discussing the algorithmic details of the CG procedure, we present results exploring the robustness of the method in predicting NP dispersion. Specifically, we seek to address the following questions: To what extent does the mesoscopic resolution affect the accuracy of the NP dispersion prediction ? How sensitive are the coarse-grained interactions and the predictions to the particle volume fraction ? How do NP-polymer interactions influence the accuracy of particle dispersion predictions ? How much computational time is saved upon implementing our CG method ? We present results suggesting that the accuracy of our CG approach in predicting NP dispersion is robust to NP loading, NP-polymer interaction, and meso-

19

scopic resolution. In addition, our CG approach reduces computational time by an order of magnitude compared to simulations of our "atomistic" system.

The outline of the rest of the chapter is as follows: Section 2.2 details the model of our "atomistic" PNC. In Section 2.3 we present results regarding the applicability of the effective one-component approach. Section 2.4 details different algorithmic aspects of the CG procedure. Results from our coarse-grained simulations are compared to the exact predictions in Sec. 2.5. We conclude with a summary and outlook in Sec. 2.6.

2.2 Simulation details of the reference system

For reasons stated in the introduction, we use a simple model system for our "atomistic" representation and henceforth denote this as our "reference" system. This reference system is simple enough to allow for a measurement of the filler structure, which can be compared with the predictions of the coarse-grained scale to test for the accuracy of our proposed CG method. In this model, the "atomistic" polymer is chosen as a bead-spring polymer and the nanoparticle as a spherical Lennard-Jones (LJ) particle of different size than the beads in the polymer. In our simulations, we fixed the polymer chain length at $N = 100$, and for the pure polymer simulations the monomer number density was set to $\rho = 0.85$ and the simulation box length was 16.03. We used a finite extensible nonlinear elastic (FENE) bond potential to model

the intramolecular bonded interactions in the polymer,[103]

$$U_b(r) = -\frac{KR_o^2}{2} \ln \left[1 - \left(\frac{r}{R_o} \right)^2 \right], \qquad (2.1)$$

where we set $K = 30.$ and $R_0 = 1.5$. The monomer-monomer intramolecular and intermolecular pairwise potentials (U_{mm}) were chosen to be LJ interactions of the form:

$$U_{LJ}(r) = 4\epsilon \left[\left(\frac{\sigma}{r - \Delta} \right)^{12} - \left(\frac{\sigma}{r - \Delta} \right)^6 \right], \quad for \quad r \leq \Delta + R_c, \qquad (2.2)$$

where σ and ϵ were set to unity, Δ was set to zero, the cutoff R_c was fixed at 1.12, and $U_{LJ}(r)$ is zero for $r > \Delta + R_c$. The NP-monomer interaction (U_{nm}) was also of the form specified by eq. 2.2 with $\sigma_{nm} = 1$ and $\Delta_{nm} = 2$. However, ϵ_{nm} and $R_{c,nm}$ were varied as a means to test the accuracy of CG method to different polymer-nanofiller interactions. Specifically, we considered the following different cases: (1) *Weak attractive interactions*: $\epsilon_{nm} = 2$ and $R_{c,nm} = 2.5$; (2) *Strong attractive interactions*: $\epsilon_{nm} = 4$ and $R_{c,nm} = 2.5$; and (3) *Repulsive interactions*: $\epsilon_{nm} = 2$ and $R_{c,nm} = 1.12$. The NP-NP interaction (U_{nn}) was also chosen to be of the form of Eq. 2.2 with the parameters: $\Delta_{nn} = 4$, $\epsilon_{nn} = 2$, $\sigma_{nn} = 1$, and $R_{c,nn} = 1.12$; this parameter choice results in the NP radius ($R_p = \Delta_{nm} + \sigma/2$) to be 2.5. The thermal energy k_BT and the monomer mass (m) were both set to unity, while the NP mass was set to 125. The NP volume fractions ($\phi = 4\pi N_p R_p^3/3L^3$, where L is the length of the simulation box and was set to 23.17, and N_p is the number of nanoparticles in

21

the simulation) for these simulations were varied such that $\phi = 0.05, 0.10, 0.15,$ or 0.20. The number of NPs in the simulation box for $\phi = 0.05$ was 10, with the number of chains being 100. From the latter PNC simulation specifications, polymer chains were removed as NPs were added for higher volume fraction simulations; this was done to keep the pressure near 5, which is what the pressure was for the pure polymer simulation.

All MD simulations were performed in an NVT ensemble, and accomplished with LAMMPS (Large-scale Atomic/Molecular Massively Parallel Simulator).[104, 105] All runs were long enough that the center of mass of the polymer moved a few R_g, for both equilibration and production periods. For the mesoscopic simulations, we also chose to utilize MD simulations to obtain a measure of the equilibrium NP dispersion. This is an appropriate choice since in this study no dynamic properties are being studied, and hence the actual dynamics and the time scales are irrelevant.

2.3 Many Body Interactions and Accuracy of Effective One Component Approach

In this section, we present results examining the validity of a common approach for coarse-graining PNCs, termed the "effective one-component approach." This approach is based on integrating out the polymer degrees of freedom to map the two component polymer-nanoparticle system to a one component system of just the particles interacting with *polymer-mediated in-*

teractions in addition to their original or bare interactions.[65, 66, 29, 30, 101] At a formal level, such polymer-mediated interactions embody all levels of interparticle interactions including pairwise interactions, three-body interactions and higher order multibody interactions. However, it is common to simplify such a framework further by an approximation which hypothesizes that the structural characteristics of the particles in the PNC dispersion, even at *finite loadings*, is determined by just the pairwise component of polymer-mediated potentials of mean forces (PMF) deduced at the *dilute* limit of particle concentrations (i.e. between two particles immersed in the polymer matrix, denoted henceforth as U_2^{PM}).[100, 29] Such an assumption can be expected to be reasonable when either (i) the influence of the third (or more) particles on U_2^{PM} is negligible; or (ii) configurations where three or more particles interact simultaneously within the range of U_2^{PM} occur only rarely. Since the range of U_2^{PM} is expected to be of the order of correlation length of the polymer melt matrix, the range of $U_2^{PM}(r)$ is of the order of polymer monomer sizes in polymer melts. Since in typical situations, the polymer monomers are smaller than the particle sizes, one may speculate that the above assumption would be applicable (due to condition (ii) above) except for very high loadings of the particles.

The simplifications arising from the preceding assumption, if applicable, are considerable. Computer simulations of PNCs where the polymers and fillers are treated on an equal footing require the equilibration of both components, making this approach almost intractable. In contrast, the preceding

approximation allows the use of an effective "one-component" representation in which the polymer-nanoparticle mixtures are reduced to one involving just the particles interacting by an additional pairwise interaction arising from polymer-mediated PMFs deduced at the limit of dilute filler concentrations. Explicitly, by eliminating the polymer degrees of freedom (except for determining the PMFs for the dilute particle limit), such an approach renders simulations of the filler structural features feasible. Moreover, reduction to a one-component particulate system also facilitates the use of liquid state and colloid physics theories and approximations to shed light on the thermodynamics and structure of the filler suspension.[29, 66, 65, 30, 61, 106, 86, 61, 100]

Since the above framework constitutes the "simplest" approach for coarse-graining PNCs, in this work, we first examine the applicability of the above assumption for the model system detailed in Section 2.2. To quantify the accuracy of the one-component approach and the importance of many-body interactions we compare two quantities:

(i) $U_2^{PM}(r)$: The polymer-mediated PMF obtained at dilute particle concentrations. These were determined by using configurations from a MD simulation where the two NPs were fixed a distance r apart in an equilibrated polymer melt. The (time) averaged polymer-NP force projected along the interparticle axis was determined and was used to obtain the effective polymer-mediated interparticle potential $U_2^{PM}(r)$;

(ii) $U_2^{MB}(r; \phi)$: Defined as the "effective" interparticle pair potential, which in a one-component approximation is capable of reproducing the struc-

24
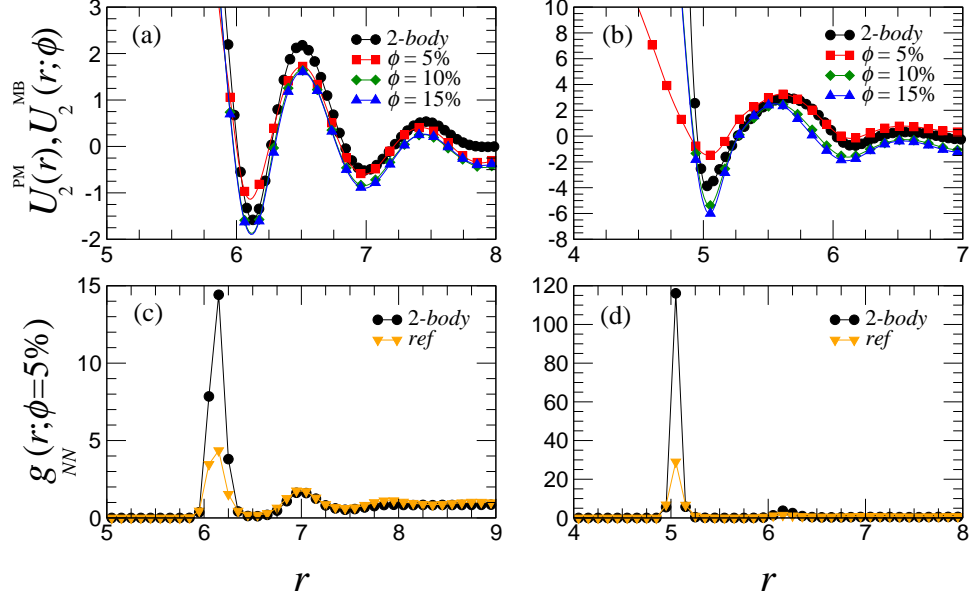
Figure 2.1: (a) and (c) pertain to the strongly attractive system and (b) and (d) are for the repulsive system. (a) and (b) A comparison of $U_2^{PM}(r)$ and the volume fraction ϕ dependent $U_2^{MB}(r;\phi)$; (c) and (d) A comparison of $g_{NN}(r)$ at $\phi = 0.05$ between the reference PNC system and that in the one-component approach (indicated by the legend 2-body).

ture of the NPs dispersed in the polymer melt. The latter was determined by simulations involving just the particles, where the interparticle interaction potentials were iteratively refined (details of such iterative refinement procedures are elaborated in the following section) such that the interparticle radial distribution functions $g_{NN}(r)$ in such simulations match with that in the reference polymer-particle mixture.[74] Since $g_{NN}(r)$ depends on ϕ, $U_2^{MB}(r;\phi)$ was determined by implementing the iterative procedure for different ϕ's.

Shown in Figs. 2.1a-b (for the sake of brevity, we display results only for the cases of strong attraction ($\epsilon_{nm} = 4$ and $R_{c,nm} = 2.5$) and repulsion ($\epsilon_{nm} = 2$ and $R_{c,nm} = 1.12$)) is a comparison of $U_2^{PM}(r)$ with $U_2^{MB}(r;\phi)$.

As expected, both cases (strong attraction and repulsion) show $U_2^{MB}(r; \phi)$ not varying much at high volume fractions ($\phi = 0.10$ and 0.15) — a fact consistent with the increased importance of excluded volume interparticle interactions at higher loadings. More interestingly, both PMFs in Figs. 2.1a-b differ considerably from their $U_2^{MB}(r; \phi)$ counterparts. Surprisingly, this disparity is even seen at particle volume fractions as low as $\phi = 0.05$, for which it is expected that $U_2^{MB}(r; \phi = 0.05) \approx U_2^{PM}(r)$; the latter results suggest that multibody effects manifest in our reference system at extremely low volume fractions. For repulsive interactions (Fig. 2.1b) the deviations between $U_2^{PM}(r)$ and $U_2^{MB}(r; \phi)$ become more pronounced at higher volume fractions, and the resulting increase in the first well-depth is suggestive of aggregated particle structures not captured in $U_2^{PM}(r)$. These discrepancies in the interparticle potentials are also reflected in a comparison of the actual $g_{NN}(r)$ and the values predicted by using a one-component approach with the interparticle potential $U_2^{PM}(r)$ (Figs. 2.1c and d).

The origins of the above discrepancies and the implied importance of many-body interactions may be understood by examining the range of particle-induced perturbations of the polymer's structure, and whether indeed the length scales are much smaller than the size of the particles. Shown in Figs. 2.2a-b are results for the polymer densities around the particles, from which it can be seen that the polymer densities deviate from their bulk values up to distances of the order of the particle sizes themselves. This feature is expected to be generically true for the nanoparticle regimes where the particle

26
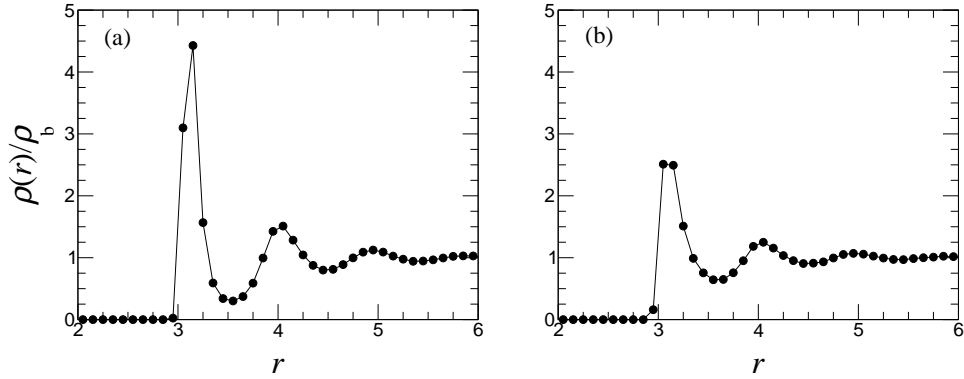
Figure 2.2: Local polymer density profiles around a nanoparticle for (a) strongly attractive and (b) repulsive cases.

sizes are typically only a few times the size of the polymer monomers.[39, 69] It is evident that due to the size scale of such polymer-particle interfacial zones, many-body overlap of such polymer perturbations can occur at extremely low particle volume fractions — thereby explaining the results presented in Figs. 2.1a - d.

2.4 Coarse-Graining Method

2.4.1 Rationale

As an outcome of the results of the preceding section, it is evident that simulations and/or models based on polymer mediated interparticle potentials of mean forces cannot prove adequate for accurate prediction of the particle structure characteristics. While simulations involving polymers and particles on an equal footing does incorporate the influence of many-body interactions, it is at the expense of being almost intractable for equilibration due to the wide

spectrum of length and time scales. An outstanding issue is whether one can devise a tractable methodology by which one can incorporate the influence of many-body interactions in predictions of the particle structure characteristics in PNCs.

To address the above issue, we propose a new methodology based on the hypothesis that the polymer-mediated forces responsible for the particle structure has two parts: (i) The polymer-mediated PMF, $U_2^{PM}(r)$, which exhibits features on the length scale of the polymer monomers (i.e. the correlation length of the polymer melt); and (ii) The many-body corrections to $U_2^{PM}(r)$, which arises from the interfacial overlap of multiple particles. *We hypothesize that the latter exhibits variations only on length scales larger than the polymer monomer sizes, and therefore to capture such effects, it would suffice to use a CG representation of the polymer molecules.*

Based on the above reasoning, our proposal for PNC simulations is to directly incorporate $U_2^{PM}(r)$ within the interparticle forces and use a coarse-grained (CG) representation of the polymer molecules to correct for the many-body interactions absent in $U_2^{PM}(r)$. Incorporating $U_2^{PM}(r)$ in such simulations is a critical feature, since the polymer-mediated interaction effects manifest on the length scale of polymer monomers and are not expected to be captured accurately by the CG polymer representation. Since the range of many-body interactions and particle sizes are usually at least a few monomer diameters, a relatively coarse polymer representation is expected to suffice for capturing the many-body interaction effects. This feature is expected to lead
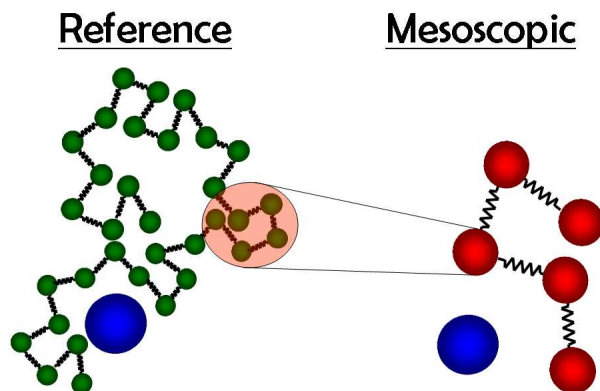
Figure 2.3: Schematic illustration of a blob and its representation in terms of the monomers at the atomistic scale.

to sufficient acceleration of PNC computer simulations compared to that of the atomistically realistic polymer representation.

Below we describe the details of implementation and validation of this idea. The objective of this CG procedure is to map the reference system of polymer and filler to a system of fillers along with coarse-grained polymers. To effect this mapping, the interactions between CG polymer segments and the polymer segment-filler interactions need to be deduced based on information from the reference (atomistic) system. As a model for CG polymers, we use a simple representation where a collection of monomers at the reference scale (referred to henceforth as "blob") is replaced by a single unit (referred to henceforth as "segment") at the mesoscale (see Fig. 2.3). We also use the terminology "nanoparticles" (NPs) and "particles" respectively to identify the fillers at the reference and the mesoscopic scales.

2.4.2 Polymer-Polymer Interactions

The first step of our CG procedure quantifies the bonded and the nonbonded segment-segment interactions. The interactions and the accuracy of the CG representation is expected to depend on the resolution of the blob (see Fig. 2.3 for a depiction), defined in this study as the number of monomers per blob (N_b). To explore the manner in which the resolution affects the predictions of NP structure, in this work we explored four different choices for N_b: 2, 5, 10, and 50. We note that $N_b = 50$ corresponds to coarse-graining the polymer as a "dumbbell." The latter is included as a probe on the limits of accuracy and resolution dependence of the coarse-graining procedure. After adopting a specific choice for N_b, we used a "structure-matching" approach to coarse-grain the polymer such that it is represented by two new CG interactions: bonded and nonbonded segment-segment interactions. Specifically, we determine the CG segment-segment bond interaction (U_{bond}) by constraining the segment-segment bond probability distribution P_{ss} to match the blob-blob bond probability distribution P_{bb}. In a similar manner, the CG segment-segment nonbonded interactions (U_{ss}) are determined by constraining the nonbonded segment-segment RDF (g_{ss}) to match the blob-blob RDF (g_{bb}).

To effect the above matching, MD simulations of a reference, bead-spring polymer melt (having parameters stated in Sec. 2.2) is performed to obtain P_{bb} and g_{bb}. In characterizing the RDFs (and probability distributions) involving the blobs, we defined the blob's position at the center of mass of

the monomers composing the blob. Following the analysis of this polymer reference system, a CG simulation of a system of just polymers composed of segments is performed. The initial "guesses" for the CG interactions for this mesoscopic system are calculated from P_{bb} and g_{bb} by a simple Boltzmann probability ansatz.[84, 89, 74] Specifically, the segment-segment bond interaction was chosen as:

$$U_{bond}(r) = -k_B T \ln [P_{bb}(r)], \qquad (2.3)$$

the segment-segment nonbonded interaction as,

$$U_{ss} = -k_B T \ln [g_{bb}(r)]. \qquad (2.4)$$

U_{bnond} was fit to a harmonic potential,

$$U_{bond}(r) = K_H (r - R_H)^2, \qquad (2.5)$$

and is used alongside U_{ss} (which was instead represented in tabular form) to define the CG simulation. Once the CG simulation is complete, results for P_{ss} and g_{ss} were obtained and compared to their reference counterparts to determine the error in the predictions of the polymer structure. For quantifying the error in U_{bond}, we used the measure

$$f_{err} = \int [P_{ss,i}(r) - P_{bb}(r)]^2 dr, \qquad (2.6)$$

where i indicates the current iteration of a sequential set of CG simulations.
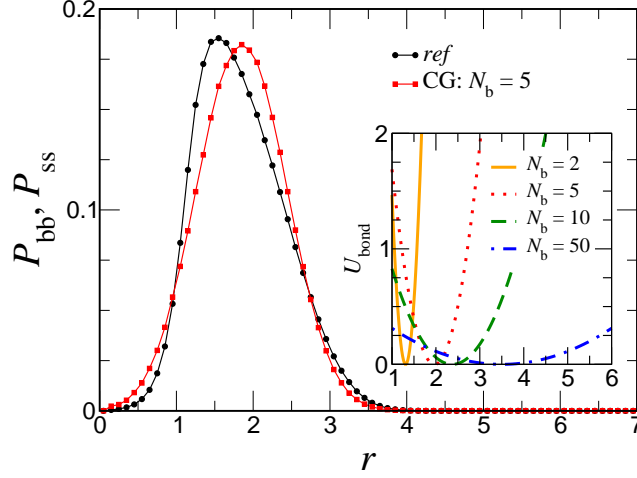
Figure 2.4: A comparison of the atomistic blob-blob bond probability distributions with the segment-segment bond probability distributions resulting from the initial guess for U_{bond}. The inset displays the harmonic bond potentials U_{bond} for various resolutions ($N_b = 2$, 5, 10 and 50).

In all the cases and resolutions examined in our simulations, the initial "guess" for U_{bond} produced a f_{err} of $O(10^{-2})$ or less, and hence was not updated further. A comparison between P_{ss} and P_{bb} is shown for $N_b = 5$ in Fig. 2.4. As can be seen from the inset of Fig. 2.4, the CG bonded potentials become softer with increase in N_b. The latter can be rationalized by noting that since the blob represents the averaged positions of a few monomers, the blob-blob probability distributions are expected to be softer relative to the corresponding monomer distributions.

The error for U_{ss} was determined using a definition similar to Eq. (2.6), with however the bond probability distributions P_{ss} and $P_{bb}(r)$ replaced respectively by the corresponding intermolecular segment-segment and blob-blob RDFs g_{ss} and g_{bb}. The error for the initial guess U_{ss} was however much more

32

significant than the error for the initial U_{bond}. To obtain a U_{ss} that produces the correct RDF, U_{ss} was refined using a procedure commonly termed the iterative Boltzmann inversion method,[74]

$$U_{ss,i+1}(r) = U_{ss,i}(r) + \alpha k_B T \ln[g_{ss,i}(r)/g_{bb}(r)], \qquad (2.7)$$

where i indicates the current iteration and α is a "pseudo time-step" that was set to unity. In the above, $U_{ss,i}(r)$ and $U_{ss,i+1}(r)$ represent the intersegment interactions at the end of steps i and $i+1$ respectively, and $g_{ss,i}$ denotes the intermolecular segment-segment RDF at the end of step i. $g_{bb}(r)$ denotes the "target" RDF corresponding to the intermolecular blob-blob distributions at the reference scale. The above iterative procedure was effected until a convergence $f_{err} \sim O(10^{-2})$ was achieved. Figure 2.5(a) illustrates the results of this iterative process by displaying g_{ss} and U_{ss} for the first and fourth iterations for $N_b = 5$. Figure 2.5(b) depicts a comparison between the converged U_{ss} with the original monomer potentials for different N_b. Yet again, U_{ss} is seen to become softer with increasing N_b, a result which can be understood to be a consequence of the possibility for the segments to interpenetrate.

2.4.3   Segment-Particle Interactions

As mentioned in the introduction of this paper, filler dispersion in PNCs has been shown to be heavily influenced by the polymer-filler interactions. Thus, an accurate representation of this interaction at the mesoscopic length scale is
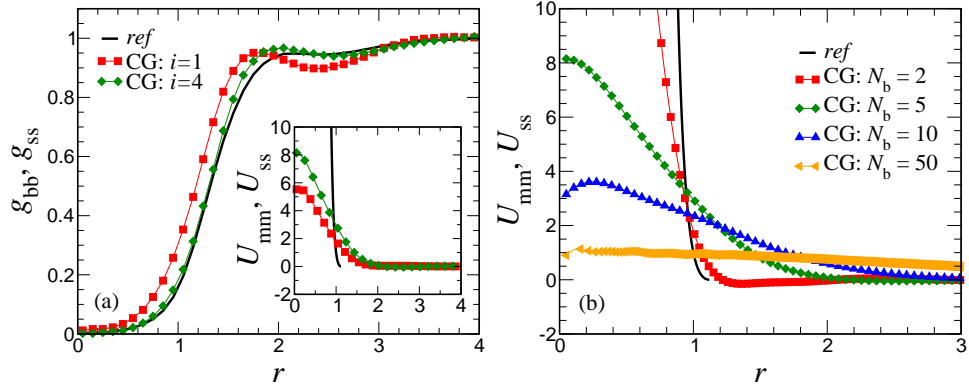
Figure 2.5: (a) Convergence of *segment-segment* RDF (g_{ss}) and (inset) interaction (U_{ss}) for a resolution of five monomers per blob. The blob-blob RDF (g_{bb}), which is shown in black, was calculated from a MD simulation of bead-spring polymers interacting with a pairwise potential U_{mm} between monomers shown in the inset with a black line. The other colored lines (red and green) correspond to different iterations, and the plots are color coordinated to match RDFs with the segment-segment potential that generated it. (b) Comparison of mesoscopic *segment-segment* potentials derived via the iterative Boltzmann procedure. Mesoscopic potentials are shown for different CG resolutions, i.e. number of monomers per blob (N_b). Each mesoscopic potential was deemed converged after $f_{err} \sim O(10^{-2})$. The black line is the *monomer-monomer* potential and is provided for comparison.

expected to be essential for capturing the filler structure in CG simulations. In order to parametrize the interactions between the CG polymer segments and the particle, again structure matching ideas were used.[107] Explicitly, the CG segment-particle interactions were chosen by constraining the RDF of segment-particle to match that of the blob-NP. This entailed simulating the reference system with one NP in the polymer matrix, with the interactions between the polymer monomer and NP chosen in the form specified in Sec. 2.2. This simulation was used to obtain the RDF between the NP and the *blobs* (g_{nb}). The coarse-grained particle-segment interaction (U_{ps}) was determined by requiring g_{ps} arising from a mesoscopic simulation of one particle in a CG polymer melt to reproduce this target g_{nb}. The intra and intersegment interactions for the CG polymer were parametrized as detailed in Sec. 2.4.2. The initial guess for U_{ps} was chosen as the potential of mean force (i.e., $U_{ps} = -k_B T \ln [g_{nb}(r)]$), and was then iterated upon with Eq. 2.7 with the appropriate subscripts substituted.

In Fig. 2.6, the results of the above iterative procedure are displayed for two *NP-monomer* interactions: (a) Repulsion ($\epsilon_{nm} = 2$ and $R_{c,nm} = 1.12$) and (b) Strong Attraction ($\epsilon_{nm} = 4$ and $R_{c,nm} = 2.5$). (Recall that we also studied a Weak Attraction case, where $\epsilon_{nm} = 2$ and $R_{c,nm} = 2.5$, which will be referenced later but is not shown in Fig. 2.6.) The reference potentials for these two cases are shown for comparison with their mesoscopic counterparts for varying resolutions ($N_b = 2, 5, 10$, and 50). Similar to the *segment-segment* interactions, the coarse-grained *particle-segment* interactions are seen to be
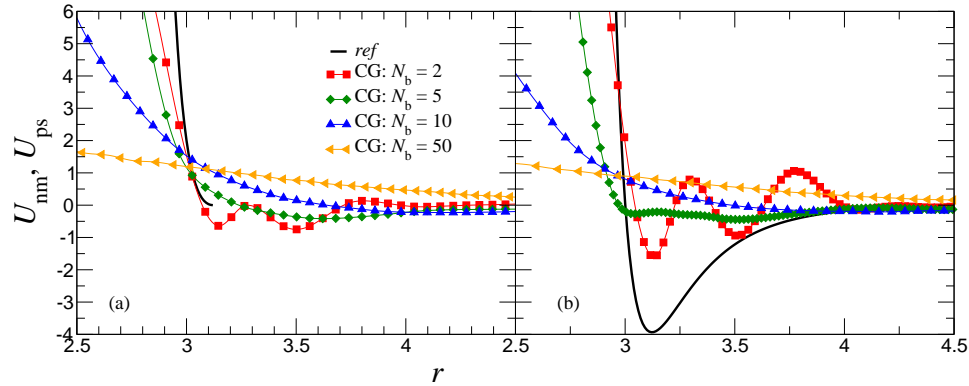
Figure 2.6: Dependence of *particle-segment* potential on CG resolution and its comparison to the corresponding *NP-monomer* potential. The black lines correspond to *NP-monomer* interactions while the other colored lines represent the *particle-segment* interactions at different resolutions for the case where the *nanoparticle-monomer* interaction is (a) repulsive and (b) strongly attractive.

softer than the original *NP-monomer* interaction. The fact that the coarse-grained potential also maintains somewhat of a hard repulsion is expected since the identity of the particles remains unchanged and hence there is expected to be a hard repulsion between the center of mass of the blob and the particles.

2.4.4 Particle-Particle Interaction

The third interaction to be included in the mesoscopic simulations is the particle-particle interaction. Since the goal of our CG methodology is to be able to "predict" the particle structure using CG simulations for situations where such information cannot be obtained from atomistic simulations, a "structure-matching" approach to deduce the CG interparticle interactions would not in general be feasible. On the other hand, since the NPs are themselves not being CGed, one may speculate that the particle-particle interac-

tions in the mesoscale simulation should just match the corresponding reference interactions. However, such a hypothesis ignores the fact that due to the coarse-graining of the polymer molecules, the polymer-mediated potential of mean-force between the particles will differ between the reference and mesoscopic scales. To illustrate this, in Fig. 2.7 we compare the polymer-mediated potential of mean forces for the reference and CG polymer representations. To determine the latter, we utilize configurations from a MD simulation where the two particles are fixed in a CGed polymer melt a distance r apart. The bonded and nonbonded segment-segment interactions U_{ss}, U_{bond}, and the particle-segment interaction U_{ps} were chosen based on the parametrizations detailed in the preceding sections. Subsequently, the averaged force projected along the interparticle axis experienced by the particles due to the surrounding polymer segments was obtained and used to determine the potential of mean-force. From the results displayed in Figs. 2.7(a)-(b) it is seen that in the (a) weakly attractive and (b) repulsive cases, the polymer-mediated interparticle forces at the mesoscale level are substantially different from the reference level. Although we do not display the same results for the strongly attractive case, they display similar trends as the weakly attractive case.

The origins of the above differences can be understood by noting that the magnitude and range of the polymer-mediated forces depend on the magnitudes and ranges of both the polymer-polymer and the polymer-particle interactions. As demonstrated in earlier sections, features of the CG interactions arise on the scale of segment sizes, whereas in the atomistic simulations
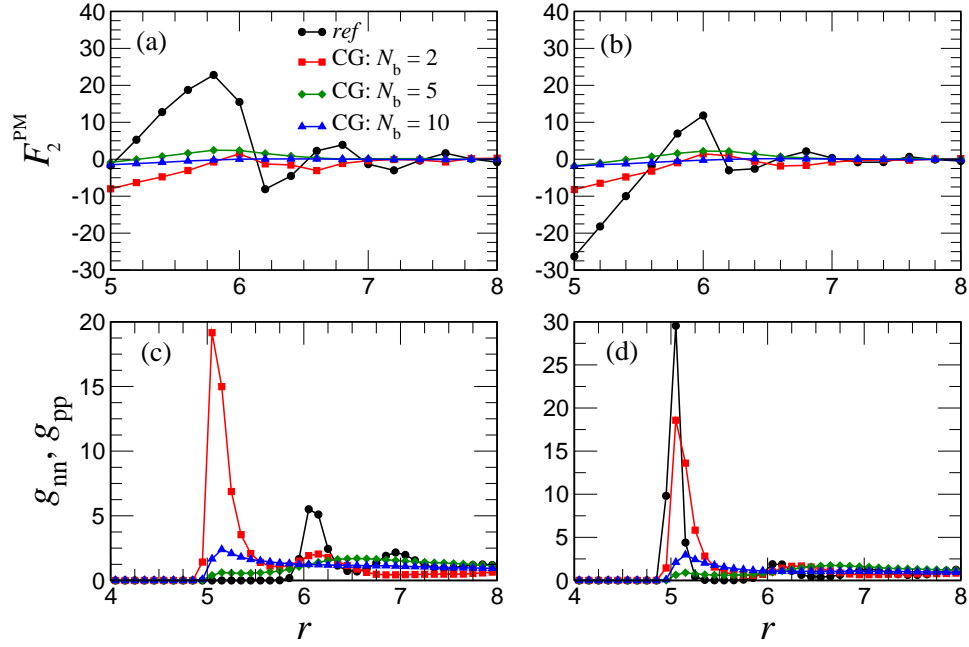
Figure 2.7: (a),(b) Polymer-mediated forces for different *NP-monomer* inter-
actions, length scale, and CG resolution. Plot (a) is for the weakly attractive
case and plot (b) is for the repulsive case. Each plot displays polymer-mediated
force from both reference and mesoscopic simulations. (c),(d) *Particle-particle*
RDFs from reference and mesoscopic simulations. Plot (c) is for the weakly
attractive case and plot (d) is for the repulsive case. Both plots are for a
NP volume fraction of 0.20. The CG resolutions shown are for $N_b = 2$ (red),
$N_b = 5$ (green), and $N_b = 10$ (blue) monomers per blob.

the corresponding features arise on the scale of monomer sizes. Moreover, the magnitudes of both the segment-segment and segment-particle interactions are considerably weaker relative to the atomistic monomer-monomer and the monomer-NP interactions. Not surprisingly, the polymer-mediated potential of mean forces also become considerably mitigated with a CG polymer representation.

Since such polymer-mediated forces (at the appropriate length scales) play a crucial role in determining the overall structure of the nanoparticle dispersion, it is evident that using a CG polymer representation in conjunction with *just* the original NP-NP interactions, would lead to inaccurate predictions for the particle structure characteristics. To demonstrate this, in Fig. 2.7(c)-(d), we present results from a CG simulation where the correctly parametrized polymer-polymer and polymer-particle interactions were used, but the particle-particle interactions at the mesoscale were kept identical to the original LJ interaction between NPs (Eq. 2.2). In Fig. 2.7, the reference *NP-NP* RDF is plotted alongside the CG *particle-particle* RDF for two different U_{nm} interactions: (c) weakly attractive and (d) repulsive. It is clearly evident that inclusion of the CG polymer with the original NP-NP interactions do not yield the correct RDFs at the mesoscale.

The above results highlight the physics underlying the CG approach proposed in this work. Recall, that a key aspect of our approach is to use the CG polymer only as a means to account for the many-body *corrections* to polymer mediated forces. Explicitly, our idea was to incorporate the "exact"

$U_2^{PM}(r)$ in the coarse-grained simulation, and proposed that the CG polymer would suffice to capture the influence of many-body effects absent in $U_2^{PM}(r)$. In this framework, the particle-particle interactions $U_{pp}(r)$ at a coarse-grained level are to be adopted as:

$$U_{pp}(r) = U_{nn}(r) + U_2^{PM}(r) - U_{2,CG}^{PM}(r), \qquad (2.8)$$

where U_{pp} is the total interaction between particles a distance r apart. $U_{nn}(r)$ denotes the NP-NP interactions in the reference system (Eq. (2.2)). $U_2^{PM}(r)$ denotes the polymer mediated potential of mean force obtained for the reference ("atomistic") system. Finally, $U_{2,CG}^{PM}(r)$ denotes the polymer mediated potential of mean force obtained for the CG system. The latter is included to avoid double counting the CG particle-segment interaction forces which are directly incorporated by using the CG polymer representation. In the following section, we present results examining the accuracy of our above CG proposal (eq. 2.8) in predicting the particle structure characteristics of different particle-polymer interactions and concentrations of the particles.

2.5 Results and Discussion

In order to validate the different aspects of the CG method proposed, we compare the *particle-particle* RDFs provided from mesoscopic simulations to *NP-NP* RDFs calculated from simulations of our reference system. To recall, U_{ss} and U_{ps} were both determined by requiring the segment-segment and segment-

particle structure to match the corresponding blob-blob and blob-NP structure of our reference system containing either no or just one particle. Moreover, U_{pp} was also obtained as the PMF at the infinite dilution limit of the particle concentrations. Therefore, using g_{nn} at finite volume fractions to quantify the accuracy of our CG method is an appropriate procedure for validation of the algorithmic details. We discuss our results for three types of NP-polymer interactions: weak attraction (Fig. 2.8), strong attraction (Fig. 2.9), and repulsion (Fig. 2.10). For each of these interaction types, we studied the following cases for the particle volume fraction: (a) 0.05, (b) 0.10, (c) 0.15, and (d) 0.20.

2.5.1   Effect of nanoparticle loading

We first consider the results for the effects of particle loading and showcase the results by considering the situation where there is a weak attraction between NP and polymer (Fig. 2.8). It is seen that the predictions from the CGed simulations quantitatively capture the oscillatory nature of the RDF as well as improve upon the prediction of the first peak seen in the reference simulations. There are minor discrepancies in the prediction of the first peak of the RDF, but such errors become diminished as the volume fraction of the particles is increased. We recall that either ignoring the polymer-mediated forces (see Fig. 2.7(c)-(d)) or not incorporating the CG polymer representation (see 2.1(c)-(d)) led to considerable error in predicting both the oscillatory nature and the height of the peaks. Thus, the predictions of the CG approach can be seen to be a significant improvement over the other predictions.
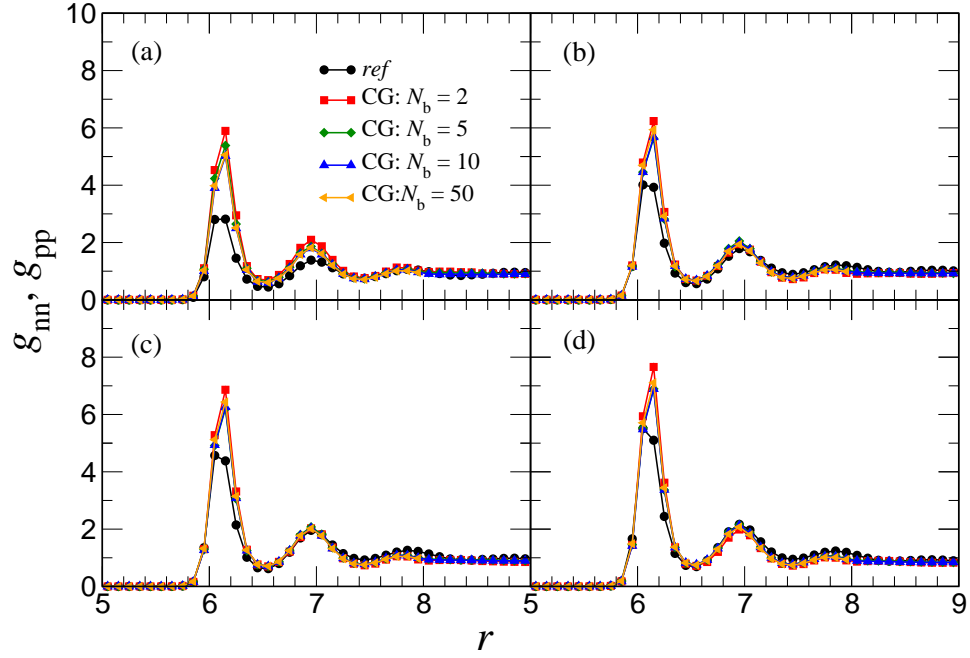
Figure 2.8: Comparison of *particle-particle* and *NP-NP* RDFs for a weakly attractive NP-polymer interaction for various volume fractions: (a) 0.05, (b) 0.10, (c) 0.15, and (d) 0.20. The black points are the *NP-NP* RDFs generated by our reference simulations, while the red, green, blue, and orange points are *particle-particle* RDFs from mesoscopic simulations at different CG resolutions indicated in the legend.
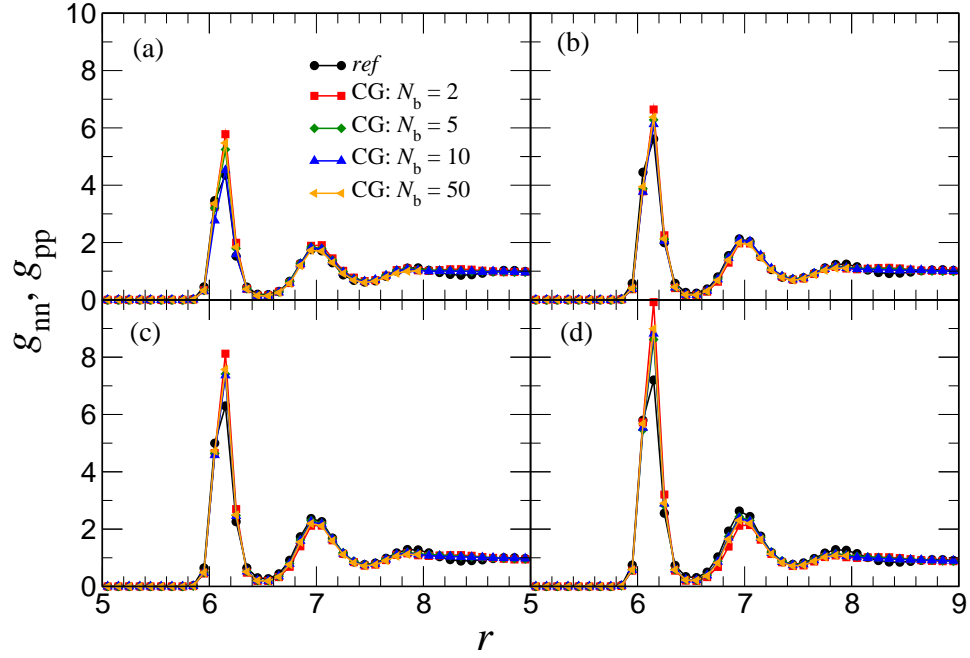
Figure 2.9: Comparison of *particle-particle* and *NP-NP* RDFs for a strongly attractive NP-polymer interaction for various volume fractions: (a) 0.05, (b) 0.10, (c) 0.15, and (d) 0.20. The black points are the *NP-NP* RDFs generated by our reference simulations, while the red, green, blue, and orange points are *particle-particle* RDFs from mesoscopic simulations at different CG resolutions indicated in the legend.
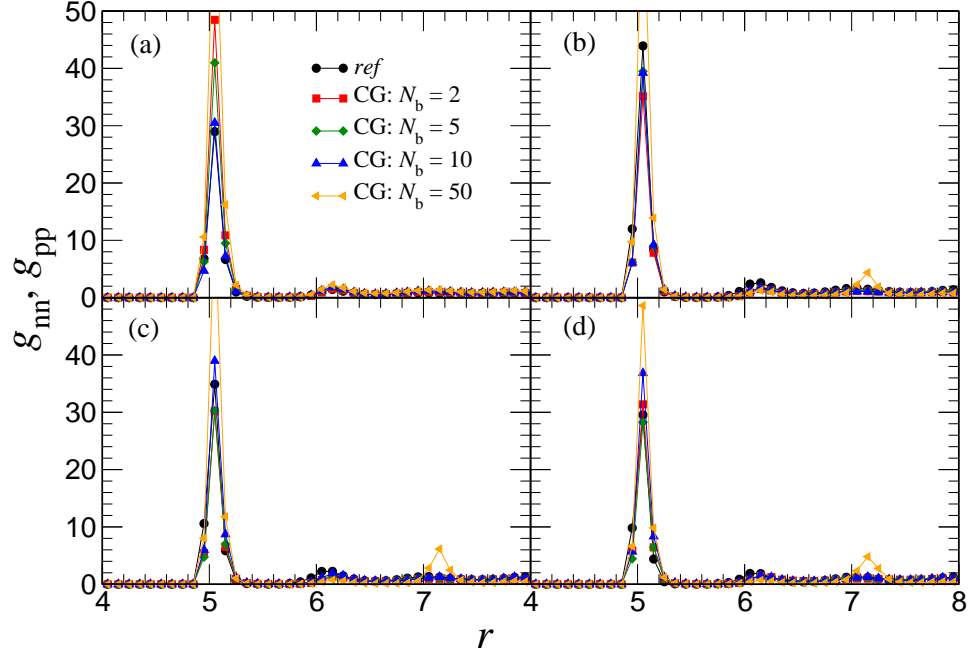
Figure 2.10: Comparison of *particle-particle* and *NP-NP* RDFs for a repulsive NP-polymer interaction for various volume fractions: (a) 0.05, (b) 0.10, (c) 0.15, and (d) 0.20. The black points are the *NP-NP* RDFs generated by our reference simulations, while the red, green, blue, and orange points are *particle-particle* RDFs from mesoscopic simulations at different CG resolutions indicated in the legend. The insets show a zoomed in version of the RDF comparison plot to display the prediction accuracy at longer distances.

In comparing the volume fraction dependent RDFs for other particle-polymer interactions (Figs. 2.9 and 2.10), it is evident that the trends seen in Fig. 2.8 apply equally well for such situations. Moreover, the discrepancies noted in the first peak in Fig. 2.8 become less significant for the other NP-polymer interactions, suggesting that the CG simulations prove accurate in capturing the interparticle structural effects for different polymer-nanoparticle interactions even up to reasonably high volume fractions.

2.5.2 Dependence on nanoparticle-polymer interaction

Considering that the NP-polymer interfacial effects can dramatically influence the manner in which the NPs are dispersed in a PNC (as can be seen by comparing Fig. 2.8(a) and Fig. 2.10(a)), it is important that our CG method be robust to such variations. Comparing the RDFs displayed in Figs. 2.8-2.10, it is evident that the quantitative accuracy of our CG simulations is insensitive to the different polymer-particle interaction types studied. Indeed, our CG method captures the structural characteristics for the situation where the particles are well-dispersed (Fig. 2.8 and Fig. 2.9) as well as for the case where the NPs exhibit an agglomerated structure (Fig. 2.10). The fact that these disparate features can be accommodated within the CG approach is a consequence of the incorporation of the polymer-mediated forces at the mesoscale.

2.5.3 Influence of blob resolution on the mesoscopic length scale

The CG blob units in this study varied from $N_b = 2$ to $N_b = 50$. Despite the fact that the different interactions were sensitive to the blob resolution, it is evident from the results displayed in Fig. 2.8, Fig. 2.9 and Fig. 2.10 that for resolutions $N_b = 2 - 10$, there are no noticeable differences in accuracies of the predicted NP structure. We believe that this feature is again a result of the direct inclusion of the polymer-mediated forces U_2^{PM} at the mesoscale. Interestingly, in Figs. 2.8 and 2.9, we observe that even an extremely coarse resolution $N_b = 50$ is seen to enable quantitatively accurate predictions for the attractive case. The latter corroborates our hypothesis that multibody corrections are expected to vary on much larger length scales, especially for *well-dispersed systems* such as for attractive polymer-particle interactions.

2.5.4 Transferability of Interactions

As mentioned in the introduction, CG schemes suffer from the drawback that the CG interactions are typically only applicable to the thermodynamic conditions at which they were derived. It is of interest to probe the impact of such transferability issues upon our coarse-graining scheme, and specifically, whether such issues are particle loading, polymer-particle interactions and/or polymer resolution dependent.

To probe the transferability of the interactions, we applied our CG interactions to different thermodynamic state points to test their sensitivity to

temperature and density. This was completed by running the reference and mesoscopic simulations at various temperatures while keeping all the interactions the same as outlined above. More specifically, the reference system was defined by the interactions detailed in Sec. 2.2 and the mesoscale simulations were defined by the interactions deduced in Secs. 2.4.2- 2.4.4. (It should be noted that the CG interactions were unaltered when utilized for these different thermodynamic state points.) The accuracy of our NP structure predictions was again determined by comparing the RDFs between particles at the mesoscale and NPs at the reference scale. We explored the temperature and density dependence by (1) fixing the density at 0.85 and setting $T = 0.8$ and $T = 2.0$ (Figs. 2.11- 2.13) and (2) fixing the temperature at $T = 1.0$ and setting $\rho = 0.60$ and $\rho = 1.00$ (Figs. 2.14- 2.16); for each set, two volume fractions were investigated: $\phi = 0.05$ and $\phi = 0.20$.

To explore the temperature sensitivity of the CG interactions we set $T = 0.8$ and $T = 2.0$, separately, and varied the interaction potential between the polymer and particle. The results for the weakly attractive case is presented in Fig. 2.11, the strongly attractive case in 2.12, and the repulsive case in 2.13; each figure displays the temperature and volume fraction associated with the simulations and all coarse-grained simulations were held at resolution of $N_b = 5$. Fig. 2.11 and Fig. 2.12 show that the CG interactions accurately predict the NP structure for $T = 2.0$, but not as well for $T = 0.8$. In contrast, for the repulsive case (Fig. 2.13) this trend is opposite; the lower temperature shows better results. Whereas the former result can be explained as a consequence
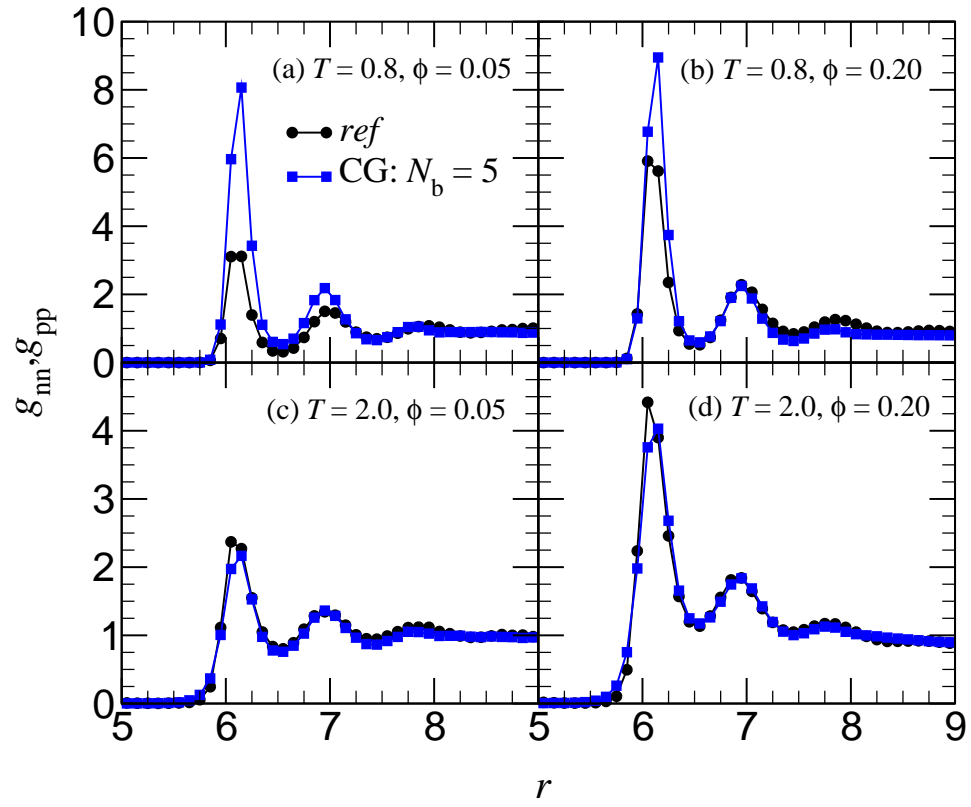
Figure 2.11: Temperature comparison of *particle-particle* and *NP-NP* RDFs for weak attraction between NP and polymer.
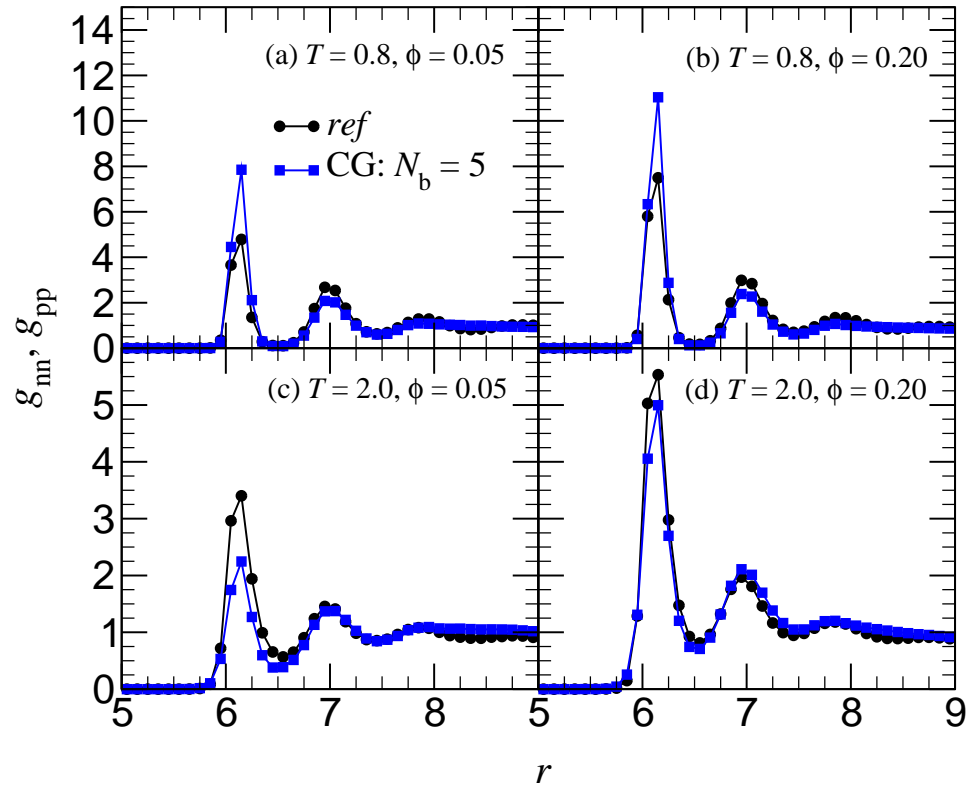
Figure 2.12: Temperature comparison of *particle-particle* and *NP-NP* RDFs for strong attraction between NP and polymer.
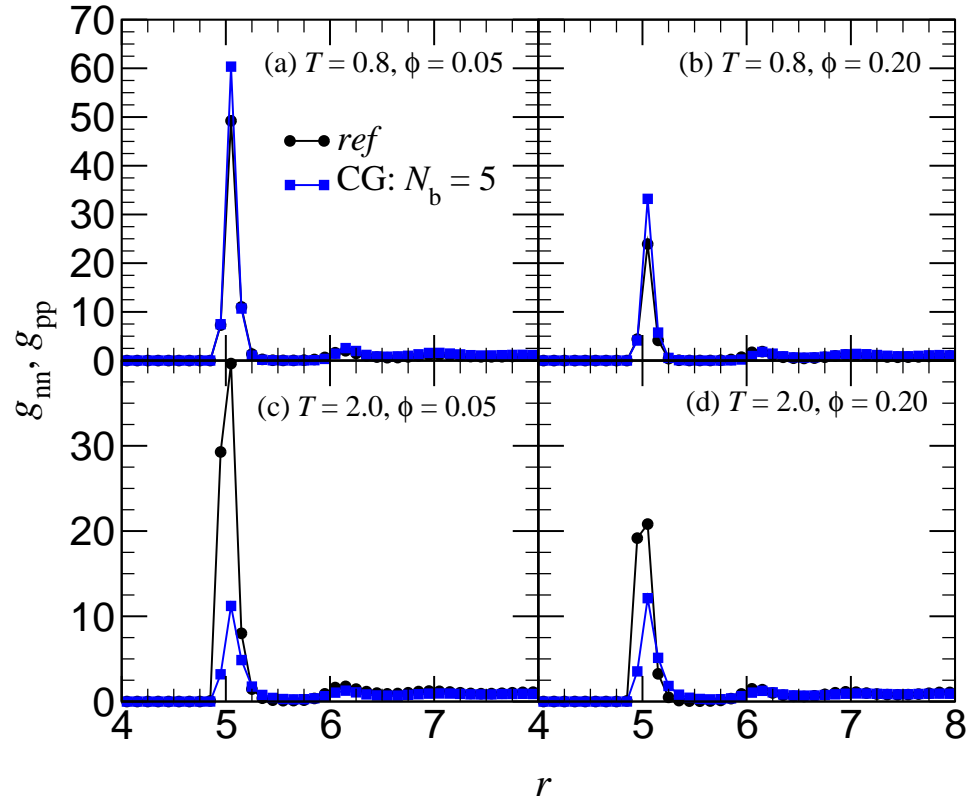
Figure 2.13: Temperature comparison of *particle-particle* and *NP-NP* RDFs for repulsion between NP and polymer.
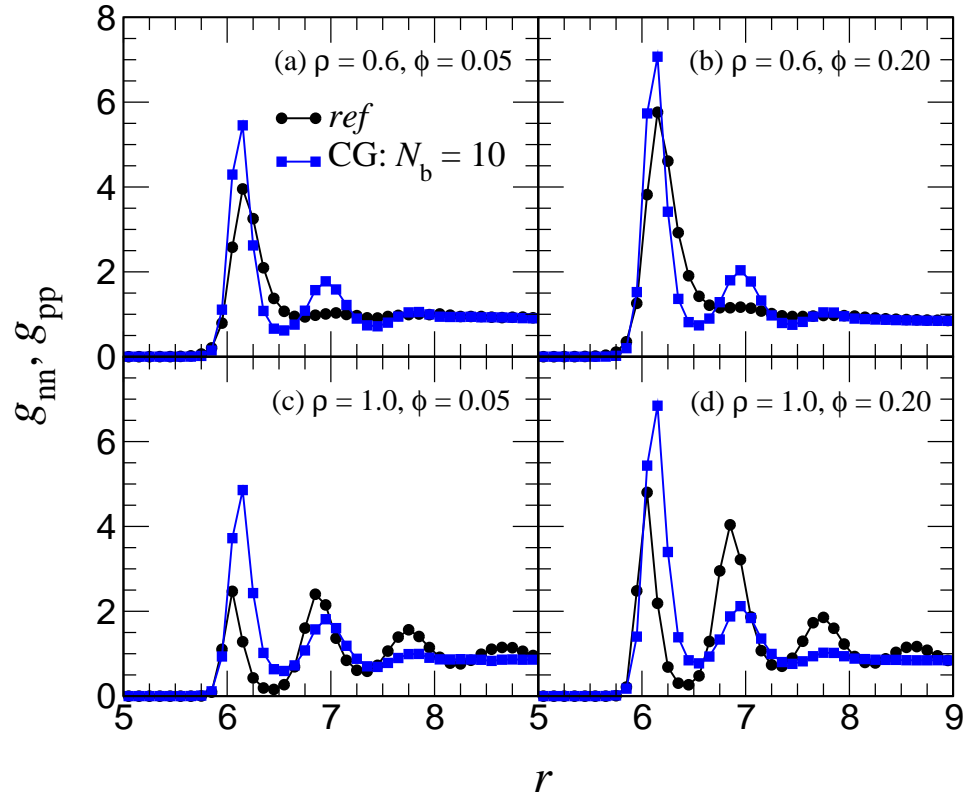
Figure 2.14: Density comparison of *particle-particle* and *NP-NP* RDFs for weak attraction between NP and polymer.
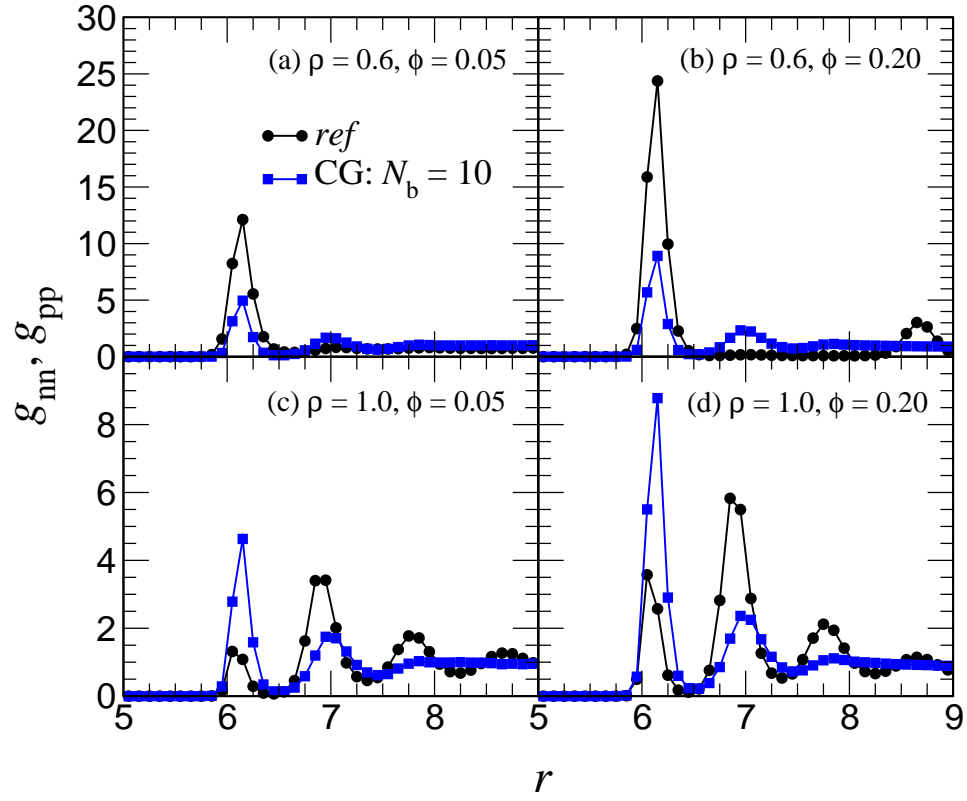
Figure 2.15: Density comparison of *particle-particle* and *NP-NP* RDFs for strong attraction between NP and polymer.
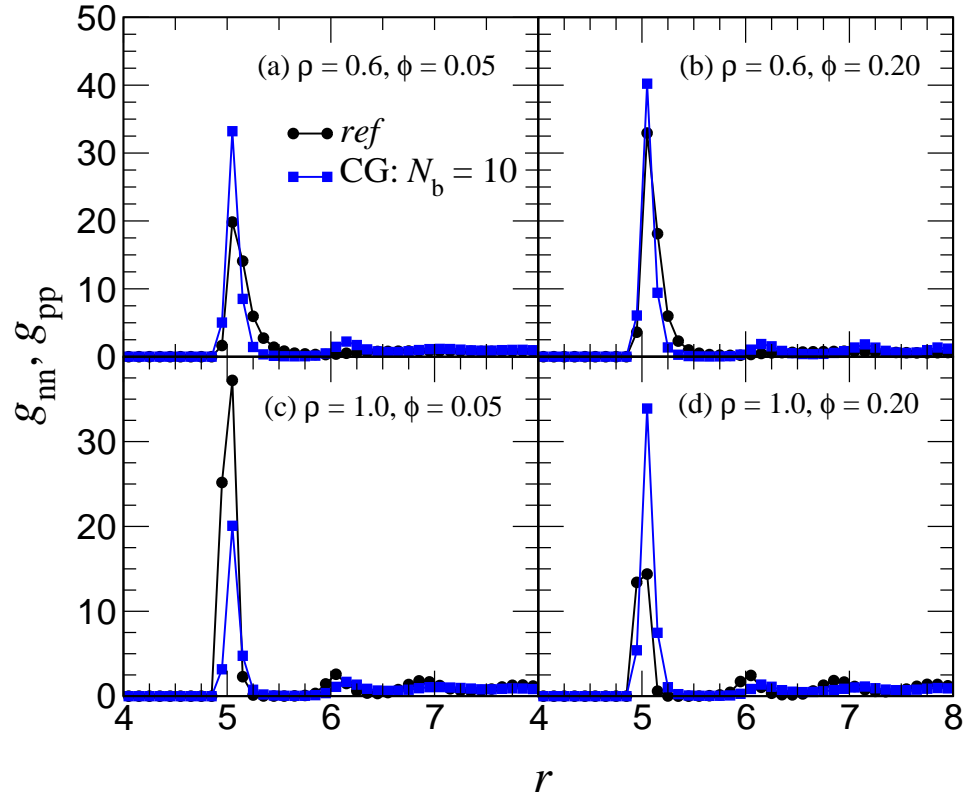
Figure 2.16: Density comparison of *particle-particle* and *NP-NP* RDFs for repulsion between NP and polymer.

of the fact that at higher temperatures the polymer-mediated interactions are less important since thermal energy and repulsive interactions tend to be the predominant structural determinent, we do not have an explanation for the latter results and believe it to be fortuitous.

The influence of density on our NP structure predictions was investigated by simulations at $\rho = 0.60$ and $\rho = 1.00$. These results are given at a resolution of $N_b = 10$ for different polymer-particle interactions: weak attraction (Fig. 2.14), strong attraction (Fig. 2.15), and repulsion (Fig. 2.16). From the displayed results, it is evident that the NP structure predictions are very sensitive to density changes in the PNC system, and that our CG scheme is not able to capture such changes. Indeed, for the low density case, a long range structure is predicted in reference RDFs which contrasts with the results for the reference simulations. In contrast, the higher density reference system exhibits longer range structure than predicted from our coarse-grained simulations. In hindsight, such results are not wholly surprising considering the sensitive dependence of the polymer-mediated interparticle forces upon the overall polymer density.

We summarize that the intention of this portion of our study was not to develop a rigorous scheme for ensuring the transferability of the potentials. Rather, our motivation to explore the sensitivity of the CG interactions to temperature and polymer density changes. In this regard, our results do point to the CG interactions being more sensitive when applied at different densities than different temperatures. Also, though all CG resolutions are not

explored, it is expected that different resolutions will show similar trends as the resolutions investigated here.

2.5.5 Reduction of Computational Resource Requirements

The main goal of CG is to reduce (relative to a full atomistic simulation of the system at a finite concentration of particles) the amount of computational resources required to simulate a system while still keeping intact certain properties of the system. In the previous sections, we have already discussed the manner in which the latter was accomplished. In this section, we briefly comment on the computational advantages derived in using the coarse-grained approach. Explicitly, to simulate our reference simulation in parallel on 16 processors took approximately 48 hours. In contrast, the mesoscopic simulations needed only 5 hours on a single processor. A second implicit advantage to our CG scheme was that it requires at most a reference simulation involving two NPs fixed in a polymer matrix — which is considerably more feasible than simulating a fully atomistic PNC. In fact, such two-particle simulations for much more realistic atomistic potentials have already been achieved, suggesting that our methodology can be translated directly to such systems.[37]

2.6 Discussion and Outlook

In this chapter, a coarse-graining method was developed with an aim to accurately predict NP dispersion in PNCs. The CGing procedure involved mesoscale simulations of NPs dispersed in a CG representation of the polymer matrix. The mapping of the reference ("atomistic") scale to the mesoscale was accomplished by (1) requiring that mesoscale polymer-polymer and polymer-particle interactions reproduce (at a predetermined resolution) the polymer structure in the bulk and near the NP surfaces; and (2) including the exact polymer-mediated interparticle interactions from the reference level. The CG method introduced and tested on PNCs in this study is shown to accurately predict NP structure while being robust to the changes in NP loading and NP-polymer interactions. We were able to (1) reduce the computational time required to predict the NP structure by an order of magnitude and (2) reduce the most computationally expensive input of our CG method to an atomistic simulation containing only a polymer melt and two nanoparticles.

The approach proposed in this chapter was motivated by demonstrating the influence of polymer-mediated many-body interactions upon the particle structure characteristics in PNCs. We note that the influence of many-body interactions has been demonstrated earlier in the context of dilute polymer solutions.[86, 108] In such studies the variation of both $U_2^{PM}(r)$ and its many-body corrections occur on the length scale of the correlation length of the solution which corresponds to the size of the polymer coils in the dilute concentration limit. The melt situation considered in our study contrasts with the

above in that the correlation length is expected to be of the same scale as the monomer size. In such situations, one would typically expect the many-body effects to not be relevant until dense volume fractions of particles. However, we provided evidence for the non intuitive result that even in the melt situation, many body effects can indeed be significant in influencing the overall structure of the nanoparticles. More surprisingly, such effects were shown to be relevant at extremely low volume fractions of particles!

Along similar lines, we note that earlier work by Bolhuis *et al.* for mixtures of colloid-(dilute) polymer solution mixtures uses a methodology superficially similar to the approach proposed in this work.[109, 108, 110, 111, 112, 107, 41, 86] Explicitly, they use a "soft-colloid" CG representation of the polymer for addressing the thermodynamics of the mixture. In our notation, this is equivalent to a case where each polymer molecule is coarse-grained to a single degree of freedom. However, an important difference in this earlier work is the absence of $U_2^{PM}(r)$ in the mesoscale simulations. This relates to the fact that in a (dilute) solution the correlation length of the polymer solution is of the order of the radius of gyration of the polymer (R_g). Hence, all polymer scale effects, including the polymer-mediated interparticle potentials of mean forces, arise on the scale of R_g. Whence, coarse-graining the polymer on the scale of R_g and using a soft-sphere representation suffices to capture, even with the uncorrected particle-particle interactions, the influence of the polymers upon the particle structural characteristics. In contrast, in our system of polymer melt, the correlation length of the polymer matrix and the

features of $U_2^{PM}(r)$ occur on the scale of the monomer sizes. So, any coarse-graining of the polymer which does not correct the interparticle interactions would necessarily miss effects arising from the polymer-mediated interactions (as was demonstrated in Figs. 2.7(c)-(d)).

The main focus of this work was to develop a minimal CG scheme by which the nanoparticle structural characteristics at finite loadings could be deduced by using atomistic information involving at most one or two particles in the polymer melt. While we demonstrated the robustness of our procedure for different polymer-particle interactions and particle loadings, a related question was the transferability of such interactions to other thermodynamic conditions. Strictly speaking, the CG interactions derived are expected to be only applicable at the thermodynamic conditions for which it was derived.[113, 114, 115, 116, 117, 118] Indeed, our investigation of the CG interactions over a range of densities and temperatures follows this rule. The instances where we did see the CG interactions be applicable to other thermodynamic conditions can be merely explained as fortuitous.

Although this study was restricted to a simplistic model of bead-spring polymer embedded with LJ NPs, the methods that comprise our CG approach have been previously shown to work well for fully atomistic polymers. Thus, we are hopeful that our CG method would be applicable to an atomistically detailed representation of the PNCs with the same level of accuracy shown here. We point out that in a more realistic representation of a PNC, additional detailed intramolecular interactions may be required; for instance, alongside

bond interaction, angle and torsional interactions may be necessary to produce the same accuracy we see in this study. We note that the approach proposed here can also be wrapped into property prediction approaches which require particle structure as an input (see Chapter 5). Moreover, with appropriate matching of time scales, our method can potentially be extended to investigate the dynamical properties of PNCs. More generally, the ideas demonstrated in this chapter may provide a means to incorporate many-body interactions in the simulation of other particle containing complex fluids where a coarse-grained representation of the permeating fluid may be used as a means to correct the potential of mean-forces deduced in the dilute limit.

Chapter 3

Predicting Rheological Properties of Polymer-Nanoparticle Melt Mixtures

3.1 Introduction

The addition of nanofillers into polymers can create an enhancement in the rheological response of the nanocomposite [45, 43, 44]. Moreover, this complicated response has the ability to influence the way the nanofillers are arranged. In this chapter, we explain a method that augments the equilibrium coarse-graining method explained in Chapter 2 to include the dynamical effects at the mesoscopic resolution. To determine the validity of our method, we compare a reference system (the same used in Chapter 2) simulated with molecular dynamics with a CGed system simulated with dissipative particle dynamics. This comparison is realized by comparing each length scale's stress response. Specifically, an oscillatory shear is applied to both the reference and CG systems and the storage (G') and loss (G'') modulus are compared. We find upon using the method explained in this chapter that these moduli are predicted semiquantitatively with CG DPD simulations

3.2 Simulation Details of Reference System

For reasons stated in the introduction of Chapter 2, we use a simple model system for our "atomistic" representation and refer to it as our "reference" system. This reference system is simple enough to allow for a measurement of the storage and loss moduli, which can be compared with the predictions for the same quantities from our mesoscopic simulations of the CGed PNC. Such a comparison will elucidate the accuracy of the extension proposed here (denoted as dynamic CG method) to the previously elaborated equilibrium CG method. We use the same reference system in Chapter 2, namely, a bead-spring polymer interacting with Lennard-Jones particles of different size. We do highlight here the details of the polymer-nanoparticle interactions since they are of importance in this study. However, polymer-polymer and particle-particle interactions are the same as described in Chapter 2. The nanoparticle-monomer intramolecular and intermolecular pairwise potentials (U_{nm}) were chosen to be LJ interactions of the form:

$$U_{LJ}(r) = 4\epsilon \left[\left(\frac{\sigma}{r - \Delta} \right)^{12} - \left(\frac{\sigma}{r - \Delta} \right)^{6} \right], \quad for \quad r \leq \Delta + R_c, \qquad (3.1)$$

where $\sigma = 1$, $\Delta = 2$, and $U_{LJ}(r)$ is shifted so that it is zero at R_c and for $r > \Delta + R_c$. To vary the monomer-nanoparticle interaction we study three cases: (1) weak attraction, $R_c = 2.5$ and $\epsilon = 2$; (2) strong attraction, $R_c = 2.5$ and $\epsilon = 4$; (3) repulsion, $R_c = 1.12$ and $\epsilon = 2$. The NP volume fraction was determined in the same manner as Chapter 2 and was varied such that

$\phi = 0.05$ and $\phi = 0.15$.

To apply an oscillatory shear to our reference system, we begin with an equilibrated configuration of our reference PNC and perform non-equilibrium MD (NEMD) simulations in LAMMPS [105, 104]. Specifically, a Nose/Hoover thermostat is coupled with the SLLOD equations of motion [119], and the simulation box is tilted with a specified frequency (ω) having a max deformation of 10% of the simulation box length. The frequency is defined by $\omega = 2\pi/T_p$, where T_p is the period of strain oscillation and was set to $100, 500, 1000$, and 5000. The rest of the simulation parameters (temperature, simulation box length, etc.) remain unchanged from our reference system in Chapter 2. From these simulations, we measured the stress as a function of time ($\sigma(t)$) of the system and calculated the storage (G') and loss (G'') moduli:

$$G' = \frac{\int_0^{n_p T_p} sin(\omega t)\sigma(t)dt}{\lambda_0 \int_0^{n T_p} sin^2(\omega t)dt} \tag{3.2}$$

and

$$G'' = \frac{\int_0^{n_p T_p} cost(\omega t)\sigma(t)dt}{\lambda_0 \int_0^{n T_p} cos^2(\omega t)dt}, \tag{3.3}$$

where λ_0 is the max strain (10%), t is time, and n_p is the number of oscillations periods. The results for G' and G'' obtained from this method were used to validate the predictions of these moduli from our DPD simulations of CG PNCs.

3.3 Simulation Details of Coarse-Grained Simulations

We utilized Dissipative Particle Dynamics (DPD) [120] to simulate our CG PNC system to properly conserve momentum when CG segment units of the chain collide with other CG segments or particles. Such collisions are inelastic and DPD is built to take into account this transfer of internal energy upon collision. Moreover, DPD has already been successfully applied to model PNC systems [121, 122].

In general, all DPD particles experience a total force ($\mathbf{F}$) that includes contributions from three distinct forces,

$$\mathbf{F} = \sum_i \left(\mathbf{F}_i^c + \mathbf{F}_i^R + \mathbf{F}_i^D \right), \tag{3.4}$$

where $\mathbf{F}_i^c$ is the conservative force, $\mathbf{F}_i^R$ is random force, and $\mathbf{F}_i^D$ is a dissipative force. The conservative forces can be obtained from the CG interactions we derived in Chapter 2 and here we stick to a resolution of on CG segment on a CGed polymer chain representing 10 monomers. The random force is a stochastic force with a functional form determined by the fluctuation-dissipation theorem (see Ref [121] for the functional form used in this study). The dissipative force is to account for the inelastic collisions occurring at this CGed length scale. Specifically, the CG segments comprising the CGed polymer chain experiences a velocity dependent dissipative force acting along the vector defined by its center-of-mass and the other object's (segment's or parti-

cle's) center-of-mass. The particle, however, experiences the latter plus a rotational dissipative force (this concept is borrowed from Ref [122]). Both velocity dependent and rotational dissipative forces are characterized by a single friction factor (γ). In particular, we are interested in linking the segment-segment (γ_{ss}) and particle-segment (γ_{ps}) friction factors to a dynamic quantity, which can be derived from atomistic (or in our case reference) simulations. How this is accomplished is detailed below.

After ensuring the CGed PNC was equilibrated and gave the same temperature and pressure as our CG simulations in Chapter 2 [1], an oscillatory strain was applied to the system. To accomplish this, a nonequilibrium method is used which adds a force to the equations of motion in the x-direction and utilizes Lees-Edwards Boundary condition [123]. The frequency (ω) applied to our simulations are the same as our reference simulations. Though the dynamics of such CGed systems will inherently be faster than our reference system, such a choice for ω is acceptable since by utilizing our dynamic CG method (detailed below) time is rescaled appropriately.

3.4   Dynamic Coarse-Graining Method

As mentioned in the previous section the PNC is described by three forces. The conservative force is derived by a coarse-graining method that has been proven to accurately predict the equilibrium dispersion of spherical particles

---

[1]The simulation box was varied so that the pressure of the CG simulations in Chapter 2 could be reproduced. This resulted in simulation box lengths of our CG simulations to be slightly different (± 1) than our reference system.

in a polymer melt where the particle-polymer interaction can be varied from repulsive to attractive (see Chapter 2). While the details are not repeated in this chapter, we do mention that the aforementioned method ensures that the polymer's atomistic structure in the bulk and near the particle inclusions are reproduced at the mesoscale as well as includes the potential of mean force that incorporates particle structural fluctuations occurring at a monomeric resolution.

Here, we explain the dynamic coarse-graining method that augments our previously developed equilibrium coarse-graining method. We link the dissipative (an in turn the conservative) forces to atomistic quantities. (Such an approach is akin to the approach we used for the conservative forces in the fact that the mesoscopic description is derived from the atomistic resolution.) Specifically, the frictional parameters of the dissipative forces are related to the relaxation time of the blobs at an atomistic resolution. Two relaxation times are calculated from reference simulations here: (1) τ_{bb}, the relaxation time of blobs in a purely polymer melt simulation and (2) τ_{nb}, the relaxation time of blobs near the surface of a nanoparticle. Both relaxation times are obtained from the self-intermediate scattering function ($I_s(\mathbf{q}, t)$),

$$I_s(\mathbf{q}, t) = \frac{1}{N} \left\langle \sum_j e^{i\mathbf{q}\cdot\mathbf{r}_j(t)} \right\rangle, \tag{3.5}$$

where $\mathbf{q}$ is the wave vector, $\mathbf{r}_j(t)$ is the blob's center-of-mass displacement as a function of time (t), and $\langle .. \rangle$ indicates an ensemble average. The relaxation times were extracted at a given $\mathbf{q}$ when $I_s(\mathbf{q}, t)$ is equal to 0.1. We use the
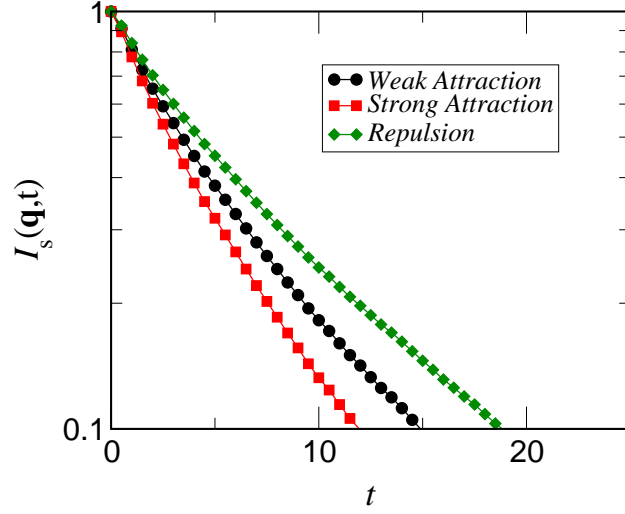
Figure 3.1: Self-scattering function for blobs in a polymer melt obtained from reference simulation. $I_s(\mathbf{q}, t)$ is given for each polymer-nanoparticle interaction type.

"interfacial layer" thickness (L_i), determined from the valley of the first peak of the particle-blob radial distribution function, to obtain the wave vector (or length scale) $q = 2\pi/L_i$ at which this relaxation time is extracted. A plot of $I_s(\mathbf{q}, t)$ for blobs in a polymer melt reference simulation is given in Fig. 3.1 with the various curves indicating different length scales determined by the interfacial layer thickness for each polymer-particle interaction.

To determine the relaxation time of the blob near the nanoparticle surface, we used Eq. 3.5 but tracked the blob's center-of-mass displacement $(\mathbf{r}_j(t))$ in a different manner. Specifically, we only track the blobs that are within the interfacial layer thickness and their motion in the plane that is normal to the initial position vector of the blob. The plot of this scattering function is given in Fig. 3.2, and we can see that $I_s(\mathbf{q}, t)$ is of exponential form like the bulk
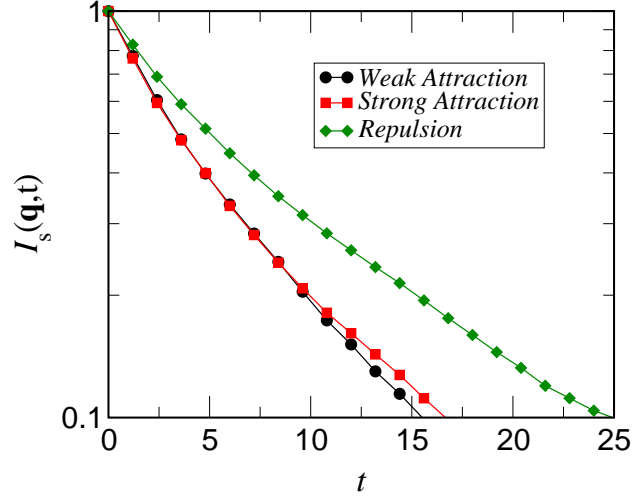
Figure 3.2: Self-scattering function for blobs near a nanoparticle obtained from a reference simulation. $I_s(\mathbf{q}, t)$ is given for each polymer-nanoparticle interaction type.

Interaction Type	L_i	τ_{bb}	τ_{nb}
Weak Attraction	1.65	14.9	15.5
Strong Attraction	1.50	11.9	16.7
Repulsion	1.75	18.8	24.9

Table 3.1: Blob relaxation times in bulk and near a nanoparticle for various polymer-nanoparticle interactions.

measurements. The interfacial layer thicknesses for each interaction type as well as the associated blob relaxation times in the bulk and near a nanoparticle extracted from Fig. 3.1 and Fig. 3.2, respectively, are given in Table 3.1.

We utilize the knowledge of the above blob relaxation times from reference simulations to determine the corresponding friction factors for our DPD simulations of the CGed PNC. Namely, we determine the segment-segment (γ_{ss}) and particle-segment friction factors (γ_{ps}). To determine γ_{ss}, we run DPD simulations of the pure CGed polymer for arbitrarily chosen segment-
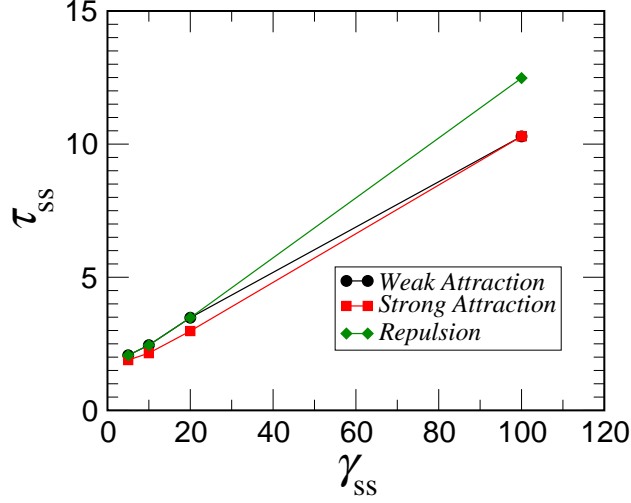
Figure 3.3: Segment relaxation time in bulk CGed polymer as a function of segment-segment friction factor.

segment friction factors, and subsequently determine $I_s(\mathbf{q}, t)$ for the segments with the same method used for the blobs in the reference simulations. A plot of τ_{ss} as a function of γ_{ss} is shown in Fig. 3.3, which clearly shows that these two quantities are linearly related and this relationship is provided in the plot. We use this linear relationship as well as τ_{bb} provided in Table 3.1 to calculate the values for γ_{ss} for each polymer-nanoparticle interaction type. Subsequently, we proposed a simple relationship between the ratio of blob relaxation times near the nanoparticle and in bulk to the ratio of the friction factors of the segment near the particle and in the bulk,

$$\frac{\tau_{ps}}{\tau_{ss}} = \frac{\gamma_{ps}}{\gamma_{ss}}. \tag{3.6}$$

The values for γ_{ss} and γ_{ps} are provided in Table 3.2 for the different polymer-

Interaction Type	γ_{ss}	γ_{ps}
Weak Attraction	153.2	159.6
Strong Attraction	118.7	165.6
Repulsion	157.5	208.6

Table 3.2: Blob friction factors for different polymer-nanoparticle interaction types.

nanoparticle interaction types studied.

3.5   Results and Discussion

Now that the connection between the DPD friction factors for the segment and the relaxation times of blobs from reference simulations has been clarified, we now show results of the storage modulus (G') and loss modulus (G'') resulting from using these friction factors. Specifically, we compare the G' and G'' results from reference simulations to those predicted from DPD simulations.

The G' results for a strong attraction between monomer and particle are shown in Figs. 3.4-3.5 while the data for a repulsive monomer-particle interaction are shown in Figs. 3.6-3.7. Fig. 3.4 shows a quantitative match between ref and CG systems for a particle volume fraction of 5%, however, for $\phi = 0.15$ in Fig. 3.5 the match is much less quantitative. This trend is opposite for the repulsive case; G' results for $\phi = 0.05$ (Fig. 3.6) are less accurate than $\phi = 0.15$ (Fig. 3.5). The inconsistent matching mentioned here can be attributed to a lack of averaging G' calculations over different initial equilibrated trajectories as well as number of periods. Specifically, only one initial equilibrium configuration was simulated for each CG data point, and the
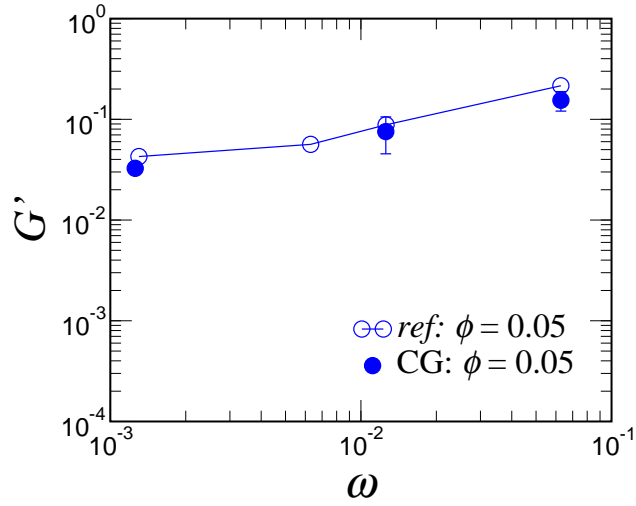
Figure 3.4: A comparison of storage modulus (G') predictions for reference and CGed PNC simulations ($\phi = 0.05$) with a strong attraction between monomer and particle.

lower frequencies were only averaged over approximately $10T_p$ after a week of simulation time. Thus, we suggest that averaging over many initial different configurations to calculate G' may improve the matching between reference and CGed systems.

The G'' results given in Figs. 3.8-3.10 are more quantitative in matching the CG simulations to the reference simulations. G'' results for attractive monomer-particle interaction are given in Fig. 3.8 and Fig. 3.9 for $\phi = 0.05$ and $\phi = 0.15$, respectively. For a monomer-particle repulsion, the G'' comparison is shown in Fig. 3.10 ($\phi = 0.05$) and Fig. 3.11 ($\phi = 0.15$). As expected, the G'' results show the worst match across length scales at lower ω, which is a result of lower number of periods to average over when calculating G'' from Eq. 3.3.
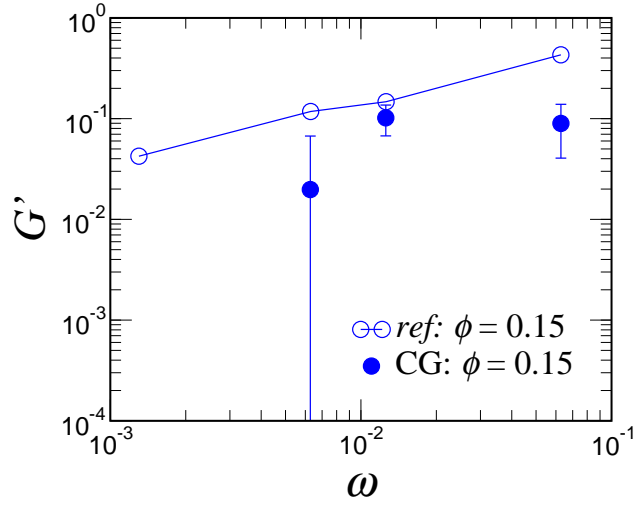
Figure 3.5: A comparison of storage modulus (G') predictions for reference and CGed PNC simulations ($\phi = 0.15$) with a strong attraction between monomer and particle.
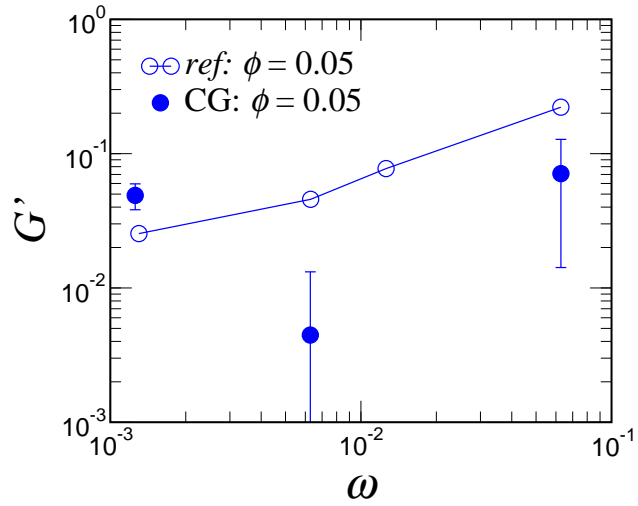
Figure 3.6: A comparison of storage modulus (G') predictions for reference and CGed PNC simulations ($\phi = 0.05$) with a repulsive interaction between monomer and particle.
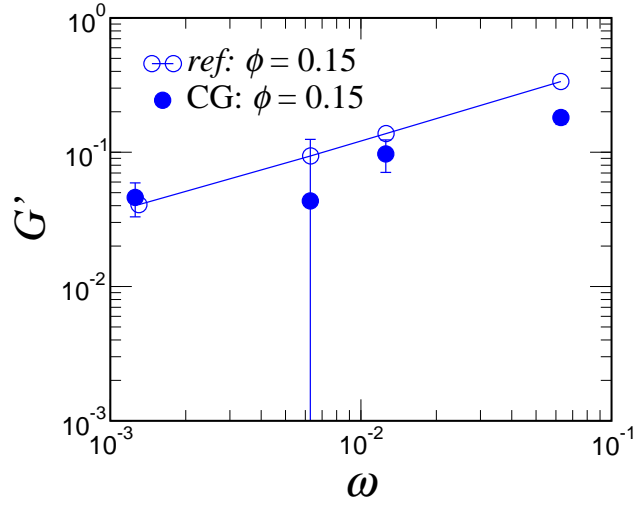
Figure 3.7: A comparison of storage modulus (G') predictions for reference and CGed PNC simulations ($\phi = 0.15$) with a repulsive interaction between monomer and particle.
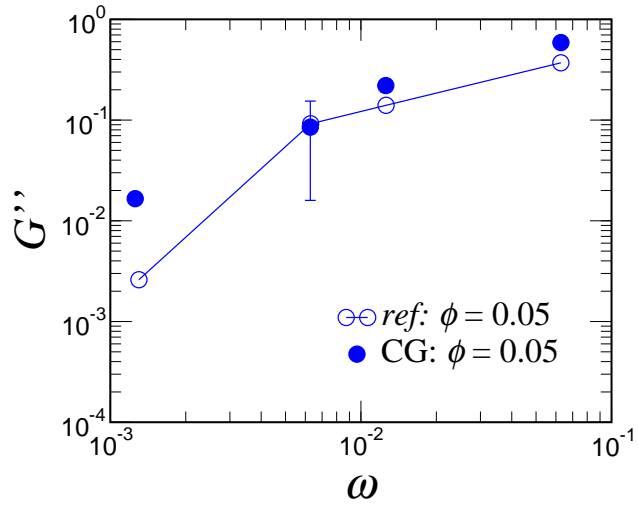
Figure 3.8: A comparison of loss modulus (G'') predictions for reference and CGed PNC simulations ($\phi = 0.05$) with a strong attraction between monomer and particle.

72
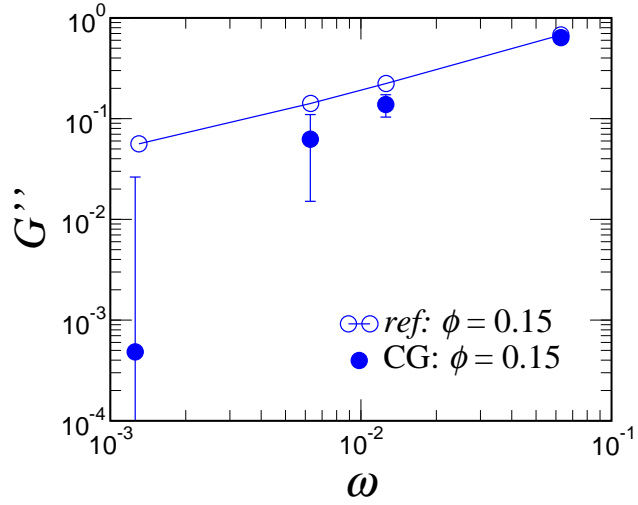
Figure 3.9: A comparison of loss modulus (G'') predictions for reference and CGed PNC simulations ($\phi = 0.15$) with a strong attraction between monomer and particle.
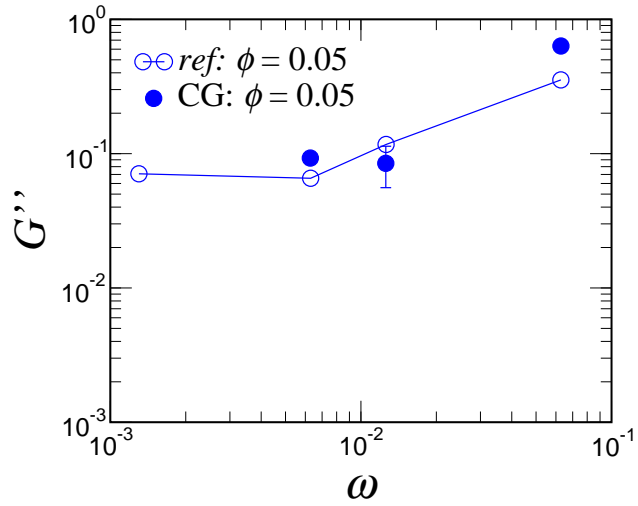
Figure 3.10: A comparison of loss modulus (G'') predictions for reference and CGed PNC simulations ($\phi = 0.05$) with a repulsive interaction between monomer and particle.
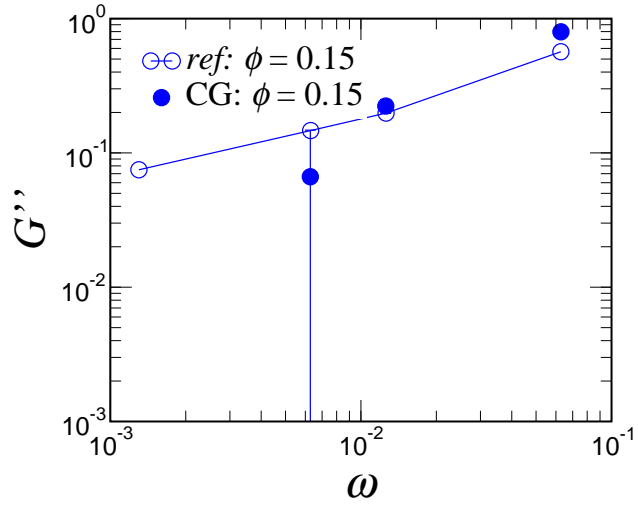
Figure 3.11: A comparison of loss modulus (G'') predictions for reference and CGed PNC simulations ($\phi = 0.15$) with a repulsive interaction between monomer and particle.

3.6   Conclusion

In this chapter, we present a method to augment our CG method that was shown to quantitatively predict particle structure via CG simulations. To accomplish this, we linked a mesoscopic quantity (the friction factor that characterizes the dissipative forces in DPD simulations) to the relaxation time of blobs (or groups of monomers) in our reference simulation. It turned out that the relationship between blob relaxation time and DPD friction factor was linear. Technically, these blob relaxation time (in the bulk and near a particle surface) could be extracted from atomistic simulations. Thus, our method could straightforwardly be applicable to more realistic all-atom PNCs. Moreover, we were able to see a semiquantitative match between reference and CG simulations for G' and G''. We suggest that our semiquantitative accuracy

may be improved upon averaging these moduli predictions over a larger number of strain oscillation periods as well as initial equilibrated configurations of the CGed PNC.

Chapter 4

Interfacial Layer Characteristics of Semiflexible Polymer Solutions Near Spherical Particles

4.1 Introduction

Pertinent to predicting the behavior of polymer nanocomposites (PNCs) is an understanding of the interfacial layer characteristics around its inclusions. The overlap of these layers can be influential in determining the nanofiller dispersion in a PNC, as seen in the previous chapter. In addition, the properties in these layers can manifest at the macroscale as has been suggested by experiments, and elucidated further for PNC barrier properties in the chapter proceeding this one. This chapter focuses on understanding what polymer and particle characteristics can influence the structure of the interfacial layer and how these characteristics can determine its length. Also, in the process, we learn how the interfacial layer thickness affects the insertion free energy of the particle in the semiflexible polymeric solution.

Many researches have examined the structure of *flexible* polymer so-

lutions around spherical particles, and pertinent results have been obtained using a variety of analytical, numerical and simulation methods.[124, 125, 126, 127, 128, 129, 130, 41] In contrast to the situation for flexible polymers, much less theoretical advances have occurred in the more biologically and experimentally relevant context of mixtures of semiflexible/rodlike polymer solutions and spherical particles. Studies so far have only considered the behaviors of an isolated semiflexible polymer chain[131] and dilute solutions of rodlike polymers near spherical particles.[132, 133, 134, 135] Scaling analysis and mean field theories have been presented for the structure of semiflexible polymer solutions and melts near flat surfaces.[136, 137, 40] To the best of our knowledge, there are no prior theoretical/numerical results which quantify the structure of semiflexible polymer solutions (at finite concentrations) near spherical particles.

This chapter presents a polymer self-consistent field theory based numerical analysis of the structure of semiflexible polymer solutions around spherical particles. We focus on the case where the polymers do not have any energetic interactions with the particle, and hence the model we consider is the case of a hard sphere inserted into a solution of semiflexible polymers. The polymers are expected to be depleted around the particle leading to an energetic cost of insertion of the particle. The present study is motivated by two issues:

(i) We desire to develop a fundamental understanding of the polymer concentration, polymer flexibility and particle size dependencies of the inser-

tion free energies of spherical probes in semiflexible polymer solutions. Indeed, many models for protein stability, partitioning and diffusion coefficients require knowledge of the insertion free energy and its scaling with sizes and concentrations.[138, 139, 140] We note in this regard that experiments which have examined properties such as the solubility of small particles in semiflexible polymer solutions have come to varied conclusions on their parametric dependcy upon the particle size R and polymer segment concentration ψ. Explicitly, quantities (P) such as solubility, insertion probability and particle mobility (related to the exponential of the insertion free energy) have been described by functional forms:[140, 141, 142]

$$P = \exp(-\alpha R^{\beta} \psi^{\gamma}) \tag{4.1}$$

with the exponents $\beta \simeq 1 - 2$ and $\gamma \simeq 0.5 - 1$, and α a numerical constant. A clear explanation for the range of experimental results noted, and theoretical predictions for P does not exist. In this work we address this question explicitly and present numerically determined scaling laws which sheds light (at a mean-field level) on the range of exponents reported in experiments.

(ii) A second motivation for this chapter is to present a numerical apporach for the solution of the self-consistent field theory equations for semiflexible polymer solutions around spherical particles. SCFT equations for semiflexible polymers have been presented and numerically solved in earlier contexts relating to block copolymers,[143] polymer solutions[144] and polymer melts near flat surfaces.[40] However, to our knowledge there has been no earlier work

which has presented the numerical solution of the equations for situations embodying spherical symmetry. As we demonstrate later, spherical symmetry brings in some new features to the formulation and the resulting equations to be solved. We present the theoretical details and the numerical solution procedure for the resulting model.

The rest of this chapter is organized as follows: In section 4.2 we present our model for semiflexible polymers, the formulation accounting for the spherical symmetry and the numerical solution procedure. The next two sections focus on the density profiles and the depletion thicknesses around a flat plate and a spherical particle. The results in the context of flat plates provide important insights on the different length scales and their interplay in determining the overall depletion thickness. We invoke physical arguments based on random phase approximation to extract numerical scaling laws describing the dependencies of the depletion thicknesses as a function of the different parameters. In the section 4.5 we present our results for insertion free energies of spherical particles and conclude with a few comments on the implications of our results for the context of above-mentioned experiments.

4.2 Model and Numerical Details

4.2.1 Model and Mean Field Limit

We consider a model for a solution of semiflexible polymers in the presence of a single spherical particle. We adopt a grand canonical formalism for the

polymer solution and use the Kratky-Porod model (KP) to describe the confor-
mations of the semiflexible polymers.[145, 146] In the KP model, the polymer
chains are represented by continuous space curves $R_i(s)$, where, i indexes the
different polymer chains, and s denotes the arc length variable running from
0 to the contour length L. The bonded interactions in the KP model are
quantified by an elastic bending energy of the form:

$$\beta U_0 = \frac{\lambda}{2} \sum_{i=0}^{\infty} \int_0^L ds \left| \frac{d\mathbf{u}_i(s)}{ds} \right|^2, \tag{4.2}$$

where $\mathbf{u}(s) \equiv d\mathbf{R}/ds$ represents the tangent vector to the chain at the contour
location s and is constrained to be a unit vector. λ represents the bending
elasticity of the polymer, and is in turn directly proportional to its persis-
tence length. To describe the excluded volume interactions between the dif-
ferent segments of the chain, we adopt the commonly used binary interaction
model:[147]

$$\beta U_1 = \frac{v}{2} \sum_{i=0}^{\infty} \sum_{j=0}^{\infty} \int_0^L ds \int_0^L ds' \delta[\mathbf{R}_i(s) - \mathbf{R}_j(s')], \tag{4.3}$$

where $\delta(\cdots)$ represents the delta function enforcing locally the exclusion of
overlaps of monomers, and v represents the strength of the excluded volume
interactions.

In the grand canonical framework, the partition function of the polymer

solution at a activity coefficient z_p can be expressed as:[146, 148]

$$\Xi(z_p, V, T) = \sum_{n=0}^{\infty} \frac{z_p^n}{n!} \int \prod_{i=1}^{n} d\mathbf{R}_i(s) \exp[-U_0 - U_1] \prod_s \delta\left(\mathbf{u}_i(s) - \frac{d\mathbf{R}}{ds}\right) \delta(|\mathbf{u}_i(s)| - 1).$$
(4.4)

The above represents a functional integral over the different space curves $\mathbf{R}_i(s)$ statistically weighted by the Boltzmann factor corresponding to the energetic interactions U_0 and U_1. The first δ function above is used to enforce the constraint that $\mathbf{u}(s)$ represents the tangent vector at the chain at the location s, whereas the second delta function enforces the fact that $\mathbf{u}(s)$ is of magnitude unity. The above partition function can be transformed by using standard functional integral methods into a field theory where the fundamental degrees of freedom is a fluctuating potential field $w(\mathbf{r})$:[148]

$$\Xi = \int_{-i\infty}^{i\infty} Dw \exp(-\beta H[w(\mathbf{r})]),$$
(4.5)

where

$$-\beta H[w(\mathbf{r})] = \frac{1}{2B} \int dr\, w^2 + \frac{\alpha}{B} \int dr\, w + Ze^{-\alpha} Q(w).$$
(4.6)

In the above, all length scales have been nondimensionalized by L. The constants $B \equiv vN^2/L^d$ and $Z \equiv z_p L^d$ represents the nondimensional excluded volume parameter and the activity coefficient of the polymer solution. The constant α satisfies $\alpha = BZ\exp(-\alpha)$, and is chosen so as to subtract out the free energy corresponding to a homogeneous polymer solution. Q represents the partition function of a single chain in the external potential field $w(\mathbf{r})$, and

is given as:

$$Q = \int q(\mathbf{r}, \mathbf{u}, 1) \, d\mathbf{r} d\mathbf{u}, \tag{4.7}$$

where the field $q(\mathbf{r}, \mathbf{u}, s)$ satisfies the equation:[145, 146]

$$\frac{\partial q(\mathbf{r}, s)}{\partial s} = -\mathbf{u} \cdot \nabla_{\mathbf{r}} q + \frac{1}{2\mu} \nabla_{\mathbf{u}}^2 q(\mathbf{r}, s) - w(r) q; \qquad q(\mathbf{r}, \mathbf{u}, s = 0) = 1. \tag{4.8}$$

Physically, $q(\mathbf{r}, \mathbf{u}, s)$ quantifies the statistical weight that a wormlike chain experiencing a potential $w(\mathbf{r})$ has its segment s at position $\mathbf{r}$ and with orientation $\mathbf{u}$. In the above equation, $\mu \equiv \lambda/N$ and represents the persistence length of the polymer expressed in units of the total contour length L. Using standard thermodynamic identities, the average homogeneous polymer solution density (nondimensionalized as $C \equiv \psi L^d / N$) can be expressed in terms of the chemical potential Z as: $C = Z \exp(-\alpha)$.

Polymer self-consistent field theory (SCFT) corresponds to a saddle point approximation of the above field theory.[148] In this framework, the integral over the potential field $w(\mathbf{r})$ in eq. (4.5) is replaced by the value of the exponent evaluated at its saddle point. Explicitly, the saddle point field $w^*(\mathbf{r})$ is given as:

$$w^*(\mathbf{r}) = BC[\phi(\mathbf{r}) - 1], \tag{4.9}$$

where the volume fraction field $\phi(\mathbf{r})$ is obtained from $q(\mathbf{r}, \mathbf{u}, s)$ as[146]

$$\phi(\mathbf{r}) = \frac{1}{4\pi} \int d\mathbf{u} \int_0^1 ds \, q(\mathbf{r}, \mathbf{u}, s; [w^*]) q(\mathbf{r}, -\mathbf{u}, 1 - s; [w^*]). \tag{4.10}$$

82

Implementation of SCFT for different situations require the iterative solution of $w^*(\mathbf{r})$ which simultaneously satisties eqs. (4.9) and (4.10) [recall that $q(r, \mathbf{u}, s)$ depends on $w(\mathbf{r})$ through eq. (4.8)] subject to appropriate externally imposed constraints. In the specific case of polymer solutions near spherical particles, the influence of the particle is transformed as a boundary condition,

$$q(r = R, \mathbf{u}, s) = 0 \qquad (4.11)$$

imposed on the surface of the sphere.[149] The self-consistent solution of eqs. (4.8) - (4.11) then provides a mean-field approach to compute the grand canonical partition function $H[w^*(\mathbf{r})]$ and the polymer volume fraction profiles $\phi(\mathbf{r})$ as a function of the polymer chemical potential Z and the excluded volume parameter B. Knowledge of $\phi(\mathbf{r})$ allows us to determine an overall depletion thickness Δ defined as the equivalent radius of a shell over which a step function profile for the polymer density would be depleted.[150] In other words Δ is defined through:

$$\frac{4\pi}{3}[(R + \Delta)^3 - R^3] = 4\pi \int_R^\infty dr \, r^2 [\phi(r) - 1]. \qquad (4.12)$$

4.2.2 Numerical Solution Procedure

In general, the diffusion equation (4.8) does not admit an analytical solution. For the limit $N \to \infty$, an approach termed as ground-state dominance allows one to simplify the equations and obtain analytical solutions for a few special

cases.[124, 137] Since our objective in this chapter is to examine the depletion characteristics for a range of particle sizes and concentration conditions, we resort to a numerical solution of eq. (4.8). In solving eq. (4.8) for polymer solution near a spherical particle, we exploit the fact that $q(\mathbf{r}, \mathbf{u}, s)$ possesses the symmetry

$$q(\mathbf{r}, \mathbf{u}, s) \equiv q(r, \mathbf{u} \cdot \mathbf{e}_r, s), \tag{4.13}$$

where r denotes the radial distance from the center of the sphere and $\mathbf{e}_r$ represents the unit radial vector (relative to an origin placed at the center of the sphere) at the location $\mathbf{r}$. By adopting a local coordinate system centered on $\mathbf{r}$ with $\mathbf{e}_r$ representing the Z axis and $\mathbf{u} \cdot \mathbf{e}_r = \cos\theta$, we can transform equation (4.8) as:

$$\frac{\partial q(r, \theta, s)}{\partial s} = -\cos\theta\frac{\partial q}{\partial r} + \frac{\sin\theta}{r}\frac{\partial q}{\partial \theta} + \frac{1}{2\mu}\frac{1}{\sin\theta}\frac{\partial}{\partial \theta}\left(\sin\theta\frac{\partial q}{\partial \theta}\right) - w(r)q; \qquad q(r, \theta, s = 0) = 1. \tag{4.14}$$

Equation (4.14) forms the starting point for analyzing the configurations of semiflexible polymers in situations embodying spherical symmetry. We note that a convenient way to solve eq. (4.14) is by expanding $q(\mathbf{r}, \theta, s)$ in Legendre polynomials as:[151]

$$q(\mathbf{r}, \theta, s) = \sum_l q_l(r, s) P_l(\cos\theta), \tag{4.15}$$

where P_l represents the lth order Legendre polynomial. By using the properties

84

of P_l, equation (4.14) can be transformed as:[151]

$$\frac{\partial q_l}{\partial s} = -\frac{l+1}{2l+3}\frac{\partial q_{l+1}}{\partial r} - \frac{l}{2l-1}\frac{\partial q_{l-1}}{\partial r} - \frac{(l+1)(l+2)}{2l+3}\frac{q_{l+1}}{r} + \frac{l(l-1)}{2l-1}\frac{q_{l-1}}{r} - \frac{l(l+1)}{2\mu}q_l - w(r)q_l,$$

(4.16)

subject to

$$q_l(r = R, s) = 0$$

$$q_l(r, s = 0) = \delta_{l,0}.$$

(4.17)

Moreover, eq. (4.10) can be recast in terms of $q_l(r, s)$ as:

$$\phi = \int_0^1 ds \sum_l \left[\frac{q_l(r,s)q_l^\dagger(r,1-s)}{2l+1} \right],$$

(4.18)

where $q_l^\dagger(r, s)$ satisfies

$$\frac{\partial q_l^\dagger}{\partial s} = \frac{l+1}{2l+3}\frac{\partial q_{l+1}^\dagger}{\partial r} + \frac{l}{2l-1}\frac{\partial q_{l-1}^\dagger}{\partial r} + \frac{(l+1)(l+2)}{2l+3}\frac{q_{l+1}^\dagger}{r} - \frac{l(l-1)}{2l-1}\frac{q_{l-1}^\dagger}{r} - \frac{l(l+1)}{2\mu}q_l^\dagger - w(r)q_l^\dagger,$$

(4.19)

subject to

$$q_l^\dagger(r = R, s) = 0$$

$$q_l^\dagger(r, s = 0) = \delta_{l,0}.$$

(4.20)

Our model is governed by three parameters: the nondimensionalized radius of the particle R, persistence length μ, the excluded volume parameter B and the bulk concentration of the polymer C. As seen from the above

equations, in the mean-field limit, the parameters B and C appear only as the combination BC in determining the density profiles $\phi(r)$. For the numerical results presented in the subsequent sections, we varied R (nondimensionalized by L) in the range $0.01 - 5$, μ in the range $0.001 - 1$ and BC in the range $0.01 - 100$. This range of parameters allowed us to cover the regimes of particle sizes where R was the smallest length scale to the regime where the curvature of the particle was inconsequential. Moreover, the range of μ chosen allowed us to span the regimes of flexible to rodlike polymers. The values of B and C covered the regimes ranging from dilute to concentrated polymer solutions.

The numerical results for $\phi(r)$ (methodology discussed below) are embedded within an iterative loop for determining the mean-field potential $w^*(\mathbf{r})$. The latter is accomplished by a real-space procedure identical to the one proposed by Fredrickson and Drolet,[152] where $w_i^*(r)$, the guess for $w^*(\mathbf{r})$ at the ith step is evolved as:

$$w_{i+1}^*(r) = w_i^*(r) + \epsilon\big(BC[\phi(\mathbf{r}; w_i^*(r)) - 1] - w_i^*(r)\big). \qquad (4.21)$$

An $\epsilon = 0.005$ allowed us to attain convergence within few thousand iterations when starting from random initial conditions.

To obtain $\phi(r)$ for a given potential field $w_i^*(\mathbf{r})$, we solved equations (4.16) and (4.19) numerically by using a two-step Lax-Wenderoff (LW) method similar to the one suggested in Daoulas and coworkers.[40, 153] Truncation of the Legendre polynomial expansion eq. (4.15) at $l = 12$ was found to ensure sufficient convergence of the density profiles. The presence of the discontin-
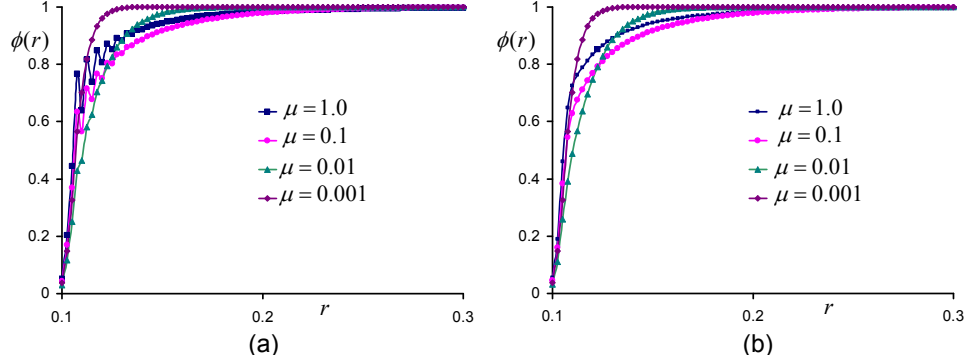
Figure 4.1: An illustration of the numerical issues and our procedure to resolve it. (a) Representative volume fraction profiles $\phi(r)$ for $R = 0.1$ and μ values indicated in the figure; (b) Smoothed density profiles corresponding to the numerical results of (a).

uous boundary condition at $r = R$ leads to numerical oscillations near the surface, which is a well-known artifact in the solution of hyperbolic partial differential equations.[154] To lucidate this, we display in Fig. 4.1a representative volume fraction profiles determined for radius $R = 0.1$ and persistence lengths $\mu = 0.001, 0.01, 0.1$ and 1.0. While the physical differences between the behaviors for these parameters constitute the focus of subsequent sections, the above discussed oscillations are certainly visible in the numerical results. We note that such artifacts become less pronounced for situations involving larger radii and/or smaller rigidity. Within the numerical schemes explored for this work, we were never able to completely eliminate such numerical oscillations. Instead, we adopted a two pronged strategy to account for such oscillations: (i) We used a one step Lax method close to the surface which is transitioned to the two step LW method [153]; (ii) We used a numerical smoothing procedure which averages out the oscillations to deduce a smooth variation in the

density profile. We repeated the preceding steps with different discretizations to ensure numerical accuracy. The equations were typically solved by using a r discretization in the range $1 - 2.5 \times 10^{-3}$ and a $\delta s = 1/2000$. The resulting density profiles were used to determine the depletion thicknesses which are discussed in the subsequent sections. In Fig. 4.1b we display the "smoothed" density plots corresponding to the original figures displayed in Figs. 4.1a.

4.3 Depletion Near Flat Surfaces

In this section, we present the numerical results for depletion thicknesses around large spherical objects and flat plates. In such a case, the polymer solution density profiles are independent of R and hence,

$$\Delta_f = f(BC, \mu). \tag{4.22}$$

Shown in Fig. 4.2 are our numerical results for Δ_f displayed as a function of BC for different values of persistence lengths μ. We observe that at very low concentrations, the depletion thicknesses plateaus to a concentration independent value. Upon increasing the polymer concentrations, Δ_f is seen to decrease monotonically with concentration. Qualitatively, $\Delta_f(C \to 0)$ is expected to be representative of the size of an isolated semiflexible polymer chain, and hence, it is easy to understand that an increase in the rigidity of the polymer segments (the parameter μ) leads to a corresponding increase in the depletion thickness Δ_f. The influence of polymer concentrations can also
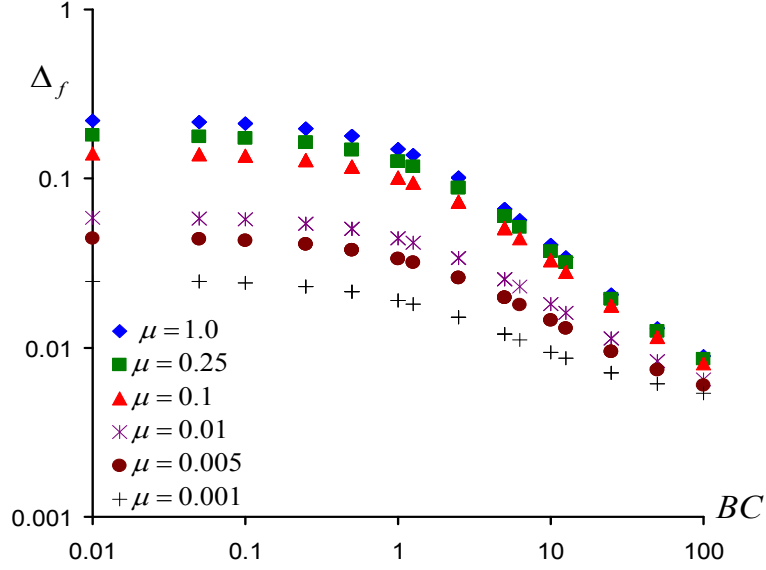
Figure 4.2: Depletion thicknesses Δ_f near flat plates as a function of the parameter BC for different persistence lengths μ.

be rationalized by noting that at higher concentrations the depletion thickness is expected to become related to the correlation length of density fluctuations in the polymer solution. The latter monotonically decreases with increasing polymer concentrations thereby explaining the behavior of the depletion thickness.

How do the quantitative details of the behavior observed in Fig. 4.2 compare with corresponding theoretical predictions ? We first compare our numerical results $\Delta(C \to 0)$ with the theoretical prediction for the nondimensional size of a semiflexible polymer chain:[155]

$$R_g(\mu) = \mu^{1/2} \left[\frac{1}{9} - \frac{\mu}{3} + \frac{2}{3}\mu^2 + \frac{2}{3}\big(-1 + \exp(-1/\mu) \big)\mu^3 \right]^{1/2}. \qquad (4.23)$$

89

In Fig. 4.3a, we compare $\Delta(C \to 0)$ alongside the above result, and observe that eq. (4.23) provides an excellent fit to our results. This confirms our hypothesis that for dilute solutions, the depletion thickness is proportional to the size of the polymer chain and is given (the prefactor determined based on the fit to numerical data) as:

$$\Delta_f(C \to 0) = 1.7\mu^{1/2}\left[\frac{1}{9} - \frac{\mu}{3} + \frac{2}{3}\mu^2 + \frac{2}{3}\big(-1 + \exp(-1/\mu)\big)\mu^3\right]^{1/2}. \quad (4.24)$$

To understand quantitatively the origins of the concentration dependence of Δ_f, we note that for flexible polymer solutions, previous theoretical researches have confirmed that a correlation length derived based on random phase approximation (RPA) accurately models the *mean-field* concentration dependence of the depletion thickness near flat plates. Whence, it is of interest to compare our above results to the corresponding RPA predictions of correlation lengths for semiflexible polymer solutions, ξ_{RPA}. Doi and coworkers considered the KP model for semiflexible polymers and derived a prediction for ξ_{RPA} as (in our notation and nondimensional variables):[155]

$$\xi_{\mathrm{RPA}} \propto R_g(\mu)(BC + 1)^{-1/2}, \quad (4.25)$$

where $R_g(\mu)$ is given by eq. (4.23). In Fig. 4.3b, we compare the above with our numerical results by considering the ratio $\Delta_f/\Delta_f(C \to 0)$ (thereby normalizing the factor $R_g(\mu)$) as a function of BC. It is seen that that our numerical results

90
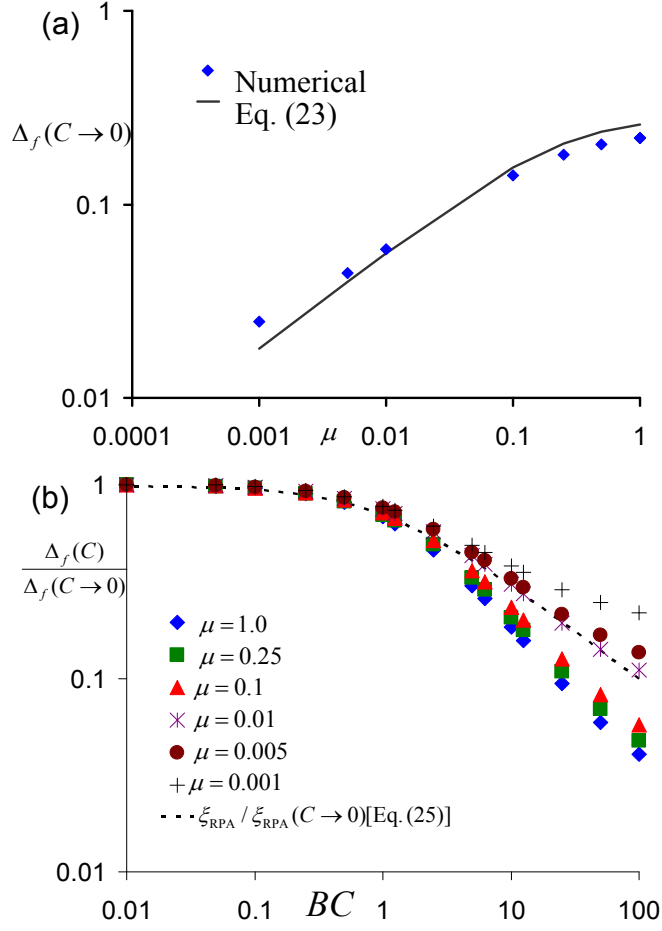
Figure 4.3: (a) A comparison of $\Delta_f(C \to 0)$ (displayed as points) with the theoretical predictions for the size of a semiflexible polymer chain (solid line); (b) $\Delta_f/\Delta_f(C \to 0)$ for polymer solutions of different persistence lengths. Dotted line represents the theoretical prediction for $\xi_{\mathrm{RPA}}/\xi_{\mathrm{RPA}}(C \to 0)$.

are not consistent with the behavior expected for ξ_{RPA}. Explicitly, we observe for large μ the concentration decay is stronger than predicted, while for smaller persistence length μ the concentration decay is weaker than that expected for ξ_{RPA}. These results suggest that the depletion thicknesses exhibits a much more complex dependence on μ and BC than that embodied in the RPA prediction for the correlation length ξ_{RPA}.

To gain more insight into the above discrepancies, we consider the RPA approximation for the density correlation function $g_{\mathrm{RPA}}(\mathbf{q})$ for semiflexible polymer solutions. While an exact expression for $g_{\mathrm{RPA}}(\mathbf{q})$ does not exist, approximate functional forms have been proposed in Marques and Fredrickson[156] and Netz *et al.*[157] We adopt the results of Netz *et al.* which yields (in units of $\mathbf{q}$ normalized as $\mathbf{q}L$)

$$g_{\mathrm{RPA}}^{-1}(\mathbf{q}) = \frac{\alpha(\mu)q^2}{1 + \alpha(\mu)q/\sqrt{6\pi}} + BC + 1, \qquad (4.26)$$

where the function $\alpha(\mu)$ is given as:

$$\alpha(\mu) = \mu\left[\frac{1}{9} - \frac{\mu}{3} + \frac{2}{3}\mu^2 + \frac{2}{3}\left(-1 + \exp(-1/\mu)\right)\mu^3\right], \qquad (4.27)$$

and is identical to the functional form for nondimensional $R_g^2(\mu)$ (eq. (4.23)). From eq. (4.26) we deduce that

$$g_{\mathrm{RPA}}(\mathbf{q}) \sim \begin{cases} (q\sqrt{6\pi} + BC + 1)^{-1} & q\alpha \gg 1 \\ (q^2\alpha + BC + 1)^{-1} & q\alpha \ll 1. \end{cases} \qquad (4.28)$$
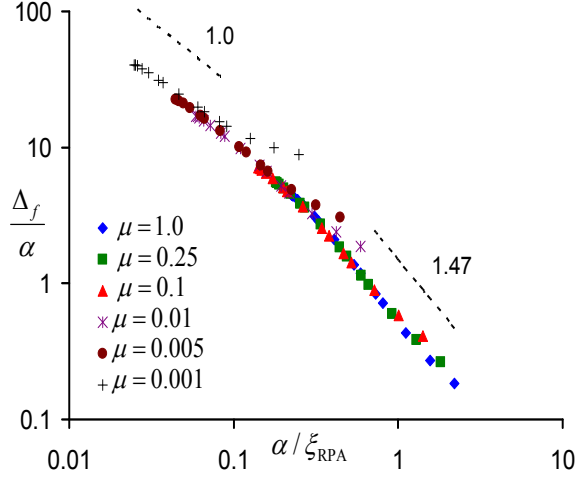
Figure 4.4: A test of the scaling proposal of eqs. (4.29) and (4.30).

From eq. (4.28) it is evident that g_{RPA} is a function of three nondimensional length scales: $\xi_{\mathrm{RPA}} \equiv \alpha(\mu)^{1/2}(BC+1)^{-1/2}, \alpha(\mu)$ and $(BC+1)^{-1}$. For $\alpha/\xi_{\mathrm{RPA}} < 1$, the decay behavior of g_{RPA} is dominated by $\xi_{\mathrm{RPA}} \equiv \alpha^{1/2}(\mu)(BC+1)^{-1/2}$. Using eqs. (4.25) and (4.27) we observe that this regime occurs when the correlation length ξ_{RPA} is larger than the persistence length of polymer, which corresponds to the "flexible" limit of the semiflexible polymer solution. In such a case, we expect the depletion thickness to be closely related to ξ_{RPA}. In contrast, for $\alpha/\xi_{\mathrm{RPA}} > 1$ the decay behavior of g_{RPA} is determined by an interplay of the length scales, ξ_{RPA} and $(BC+1)^{-1} \equiv \xi_{\mathrm{RPA}}^2/\alpha$. This regime ccurs for $\xi_{\mathrm{RPA}} \lesssim \mu$ or the "rigid" limit of the semiflexible polymer solution. In such a case, we might expect the depletion thickness also to reflect an interplay between the preceding two length scales.

The above reasoning can be encapsulated in a scaling proposal for the

depletion thickness Δ_f as:

$$\frac{\Delta_f}{\alpha} = f(\frac{\alpha}{\xi_{\text{RPA}}}), \tag{4.29}$$

with $f(x)$ expected to behave as:

$$f(x) \sim \begin{cases} x^{-1}, & x \ll 1, \\ \\ x^{-2} & x \gg 1. \end{cases} \tag{4.30}$$

This hypothesis is tested in Fig. 4.4 by considering the ratio Δ_f/α as a function of α/ξ_{RPA} (to ensure consistency, we used the numerical values for $\Delta_f(C \to 0)$ in place of $\alpha^{1/2}$). It is observed that in the above representation, $f(x)$ exhibits a behavior of $x^{-0.97}$ for $x < 1$ which crosses over to $x^{-1.47}$ for $x > 1$. While we do not observe the crossover to the exponent -2 predicted for $x \gg 1$, we speculate that the transition from the exponent -1 to -1.47 is strongly suggestive of the crossover to the asymptotic scaling behavior and hence consider the numerical results in Fig. 4.4 to be in good agreement with the hypothesis and scaling predictions underlying eq. (4.30).

In summary, our numerical results for the depletion of semiflexible polymers near flat objects suggests a complex interplay between the persistence length μ and the correlation length of the semiflexible polymer ξ_{RPA}. Explicitly, for the flexible limit of semiflexible polymers, we predict that the depletion thickness scales as the correlation length of the polymer solution. In contrast, for the limit of rigid polymers and rod solutions, our numerical results suggests that the density profiles exhibits an interplay between two length scales. Over-

all, this results in a scaling collapse of the depletion thickness as a function of the ratio $\alpha/\xi_{\mathrm{RPA}}$, and provides a quantitative prediction for use in experiments measuring the depletion thicknesses of semiflexible polymers near flat plates.

4.4 Depletion near Spherical Objects

Next, we consider the depletion characteristics of semiflexible polymers around spherical objects which brings to fore an additional length scale, viz., the radius of the particle R. It is commonly supposed that for particle sizes R much larger than the flat plate depletion thickness Δ_f, curvature effects are negligible and that the depletion thickness around the spherical particles $\Delta_R \simeq \Delta_f$.[126] The issue we address in this section is whether this consideration is indeed true for solutions of semiflexible polymers, and the implications of the persistence length-correlation length interplay noted in the preceding section. Due to numerical limitations however, we could only probe regimes such that $R/\Delta_f \geq 0.3$. Consequently, while we were able to address the relevance of curvature effects, our results do not allow us to draw concrete scaling conclusions regarding the behavior of depletion thicknesses for very small radii.

To render the parameter space tractable, we work in nondimensional variables. Explicitly, based on the parametric considerations discussed in the preceding section, we expect that

$$\Delta_R = f(BC, \mu, R). \tag{4.31}$$

Using the fact that Δ_f is a function of the parameters BC and μ, the above can be rewritten as:

$$\Delta_R = f(\Delta_f, \mu, R). \tag{4.32}$$

Since we expect that the different quantities become independent of the contour length for large contour lenghts, the above representation can be expressed in terms of three nondimensional combinations, $\Delta_R/R, R/\Delta_f$ and R/μ as:

$$\frac{\Delta_R}{R} = f(\frac{R}{\Delta_f}, \frac{R}{\mu}). \tag{4.33}$$

(we adopt this representation since it provides a better physical representation of some of the scaling collapses discussed below).

In Fig. 4.5 we display our numerical results for depletion thicknesses Δ_R/R as a function of R/Δ_f for different values of R/μ. To aid in the discussion, we have separated these results into three regimes:

(a) Figure 4.5a pertains to the results for $R/\Delta_f > 10$ and for the entire range of R/μ examined. It is seen that all the data for $R/\Delta_f > 10$ collapse onto a single curve which is independent of the value of R/μ and has a power-law slope of $\simeq -1$. This suggests that for this regime

$$\frac{\Delta_R}{R} \simeq \frac{\Delta_f}{R}, \tag{4.34}$$

or $\Delta_f \simeq \Delta_R$. This result reinforces the intuitive expectation that for very large particles (relative to the depletion thickness in the flat plate regime) the depletion thickness is independent of the curvature of the particles.
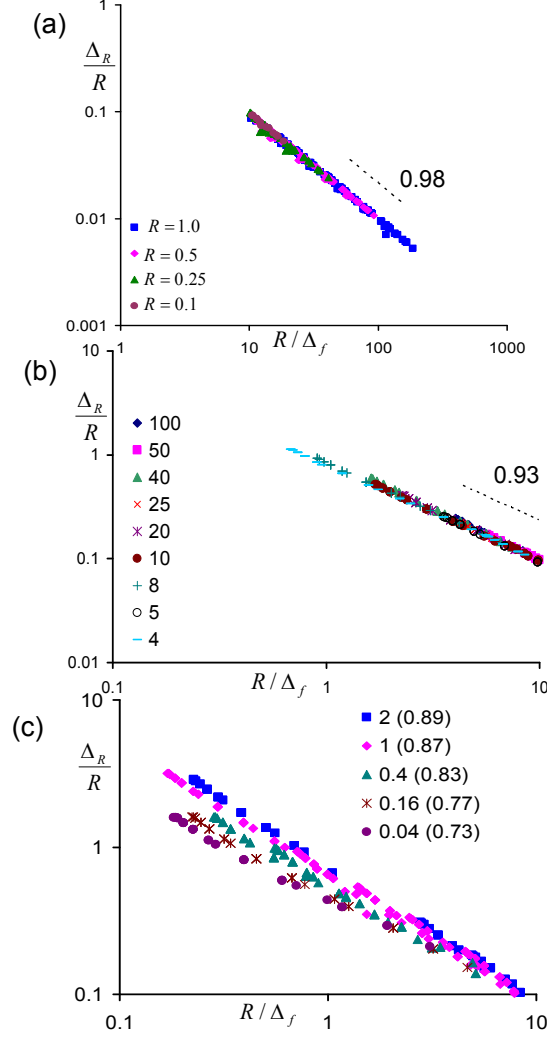
Figure 4.5: Depletion thicknesses Δ_R normalized by the radius R represented as a function of the depletion thicknesses near a flat plate (inversely normalized by R): (a) Numerical results for $R/\Delta_f > 10$ for different radii R and persistence lengths μ (to maintain clarity, we do not distinguish the different μ values by specific symbols); (b) Numerical results for $R/\Delta_f < 10$ for different R/μ indicated; (c) Numerical results for $R/\Delta_f < 10$ for different R/μ indicated. Numbers in the parenthesis correspond to the exponents of a power law fit of the data.

(b) Figure 4.5b displays the results of Δ_R/R for $0.3 < R/\Delta_f < 10$ for the regime $R/\mu \gtrsim 4$. We observe that our numerical results exhibit a scaling collapse of the form:

$$\frac{\Delta_R}{R} \simeq \left(\frac{\Delta_f}{R}\right)^{-0.93}, \tag{4.35}$$

which is independent of the R/μ considered. Whence we conclude that for large values of R/μ, the curvature of the particles has only a small influence on the depletion thickness even upto the regime $R \simeq \Delta_f$, and

$$\Delta_R \simeq \Delta_f. \tag{4.36}$$

(c) Figure 4.5c displays the results of Δ_R/R for the regime $0.3 < R/\Delta_f < 10$ for the regime $R/\mu \lesssim 4$. In contrast to the behavior noted for larger values of R/μ, we observe that Δ_R/R now displays a strong dependence on the radius relative to the persistence length of the polymer. Explicitly, we observe that the Δ_R/R exhibits a scaling of the form:

$$\frac{\Delta_R}{R} \simeq \left(\frac{R}{\Delta_f}\right)^{-\nu}, \tag{4.37}$$

with an exponent $\nu < 1$ (quantifying the deviation from the flat plate behavior), decreasing monotonically with lowering of R/μ. Moreover, it is seen that the radius at which the depletion thicknesses start to deviate from the flat plate regime also explicitly depends upon the ratio R/μ, with deviations observed at larger radii for smaller R/μ values.

A physical basis for the above trends can be obtained by combining the

insights gleaned in the preceding section with the hypothesis that curvature effects manifest when the radius of the particles becomes comparable to length scales at which density variations occur near a flat plate. For the case where μ is small (the "flexible" limit of the semiflexible polymer), we suggested that the density profiles near a flat plate exhibit variations on a single length scale ξ_{RPA} and hence $\Delta_f \simeq \xi_{RPA}$. In such regimes, curvature effects are also expected to occur only when $R \simeq \xi_{RPA} \equiv \Delta_f$. Moreover, curvature effects are expected to be only a function of R/Δ_f and hence independent of the ratio R/μ (except insofar as the μ dependence embodied in Δ_f). This reasoning rationalizes the behavior noted in Fig. 4.5b where for large values of R/μ the curvature effects did not impact the depletion thickness up until the regime $R \simeq \Delta_f$, and the deviation from the flat plate scaling (an exponent of 0.93 vs an exponent of 1.0) was independent of R/μ.

In contrast, for larger μ (the rigid polymer limit), we suggested that the density profiles near a flat plate might exhibit a two length scale behavior which depends on ξ_{RPA} and $\xi_{RPA}^2/\alpha(\mu)$ with Δ_f determined by their interplay (cf. eq.(4.30)). Since the density profiles exhibit variations on the length scale ξ_{RPA}, in this regime also we may expect curvature-induced deviations to begin when $R \simeq \xi_{RPA}$. Since the length scales follow the hierarchy $\xi_{RPA} > \Delta_f > \xi_{RPA}^2/\alpha$, the curvature induced deviations occur for $R > \Delta_f$. Moreover, using eq. (4.30) we have

$$\frac{R}{\Delta_f} = \frac{R}{\xi}\left(\frac{\xi}{\alpha(\mu)}\right)^{\beta},$$

with $\beta < 0$ ($\beta = -0.47$ in our numerical results, and expected to be -1 in the

asymptotic scaling regime). When $R \simeq \xi$, we have

$$\frac{R}{\Delta_f} \simeq \left(\frac{R}{\alpha(\mu)}\right)^{\beta}. \qquad (4.38)$$

Since $\alpha(\mu)$ is a monotonically increasing function of μ (see eq. (4.27)), the above suggests that the curvature-induced deviations in this regime occur at larger values of R/Δ_f for systems with smaller values of R/μ. This reasoning rationalizes the behavior observed in Fig. 4.5c, where indeed stronger deviations beginning at larger values of R/Δ_f where noted for systems with smaller R/μ values.

Due to the complex two parameter scaling expected for the regime depicted in Fig. 4.5c, we are unable to propose a simple scaling collapse of the data. However, for the purposes of quantitative comparisons, we empirically fitted the data for $R/\mu \lesssim 2$ and extracted a power law profile of the form (fit displayed in Fig. 4.6):

$$\frac{\Delta_R}{R} \simeq \left(\frac{R}{\Delta_f}\right)^{-0.86} \left(\frac{R}{\mu}\right)^{0.17}, \quad 0.1 < R/\Delta_f < 10. \qquad (4.39)$$

Considering the nonanalytic nature of the different exponents above, we speculate that the above scaling is not a manifestation of a distinct physical phenomena but rather a reflection of the crossover to the situation of very small particles. Unfortunately, due to numerical limitations we are unable to probe the latter regime to determine the precise asymptotic scaling laws.

In sum, our numerical results for the curvature dependence of the de-
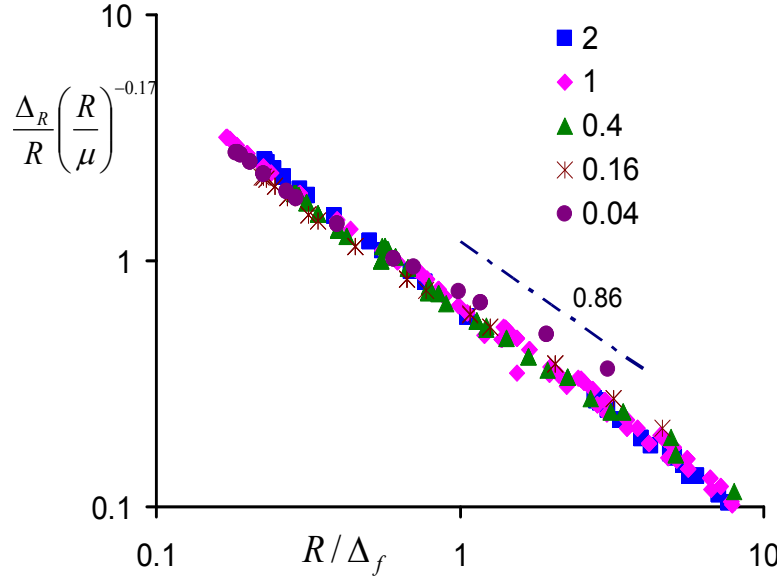
Figure 4.6: Empirical fit of Δ_R/R to the parameter $R/|Delta_f$.

pletion thickness indicates novel behavior which sensitively depends on the persistence length of the polymer relative to the radius of the particle. For the case when the persistence length of the polymer is smaller than the radii, the depletion thickness was shown to exhibit very little curvature dependence, even for radii as small as R/Δ_f and $R/\xi_{\text{RPA}} \simeq 0.5$. In contrast, for $R/\mu \lesssim 1$ and $R/\Delta_f \leq 10$, the depletion thickness starts to exhibit a curvature dependence for radii $R \simeq O(\mu)$, with the intensity of the curvature dependence monotonically increasing with an increase in the ratio μ/R.

The above results serve to higlight the subtleties in the depletion characteristics involving semiflexible polymers and small probes. Explicitly, the flexible limit is shown to behave quite differently from the rigid limit of the semiflexible polymers in their respective curvature dependencies of the deple-

101

tion thickness (and correspondingly the free energies of insertion, as demonstrated in the next section). This revises the accepted wisdom that the curvature dependence of depletion thicknesses for polymer solutions occurs for particle sizes comparable to or smaller than the the depletion thicknesses for flat plates. Instead, we suggest that the such a notion is true only for solutions of *flexible* semiflexible polymers. In contrast, for *rigid* semiflexible polymer solutions, due to the disparity between the correlation length and the depletion thickness of the polymer solution, curvature effects manifest at a length scale much larger than the depletion thickness for flat plates.

4.5   Insertion Free Energy

In this final section, we consider the dependence of the insertion free energy of the particles as a function of the different parameters in the system. As we will demonstrate, the insertion free energy of small particles is intimately tied to the depletion thickness Δ_R. Whence, the understanding developed in the preceding sections proves crucial in explaining the characteristics of the insertion free energies.

To deduce the insertion free energies, the free energy expression eq. (4.6) is computed relative to the homogeneous solution for different parameters. The insertion free energy F_1 of a particle of size R can be expected to be expressed as:[114]

$$F_1 = \Pi \frac{4}{3}\pi R^3 + 4\pi R^2 \gamma. \tag{4.40}$$

In the above, the first term represents the volumetric energy contribution arising from the work needed to create a cavity of size R, and is expressed as the osmotic pressure of the solution Π multiplying the volume of the particle. For the mean-field situation considered in this chapter, we have for the nondimensionalized osmotic pressure

$$\frac{\Pi R_g^d}{k_B T} = C + \frac{BC^2}{2},\tag{4.41}$$

and hence the parametric dependence of the first term in eq. (4.40) can be considered as understood. The second term in eq. (4.40) represents the energy penalty arising from the interfacial tension γ. The latter arises explicitly due to inhomogeneous density variations induced by the introduction of the particle, and is expected to dominate the insertion free energy for small particles.

In this section, we consider the numerical results for the interfacial tension term γ and rationalize our results by considering the explicit dependence of γ on the other parameters. Explicitly, we expect that for regimes where curvature effects do not play a significant role (see previous section), γ itself will be independent of R and only dependent on B, C and μ. In contrast, we expect that in regimes where curvature effects manifest γ would also become dependent on the curvature in a manner similar to the Tolman corrections noted for the curvature dependence of surface tension for gas-liquid interfaces.[114, 158] To render the analysis tractable, we again resort to a nondimensional framework, and nondimensionalize γ with the variable ΠR.
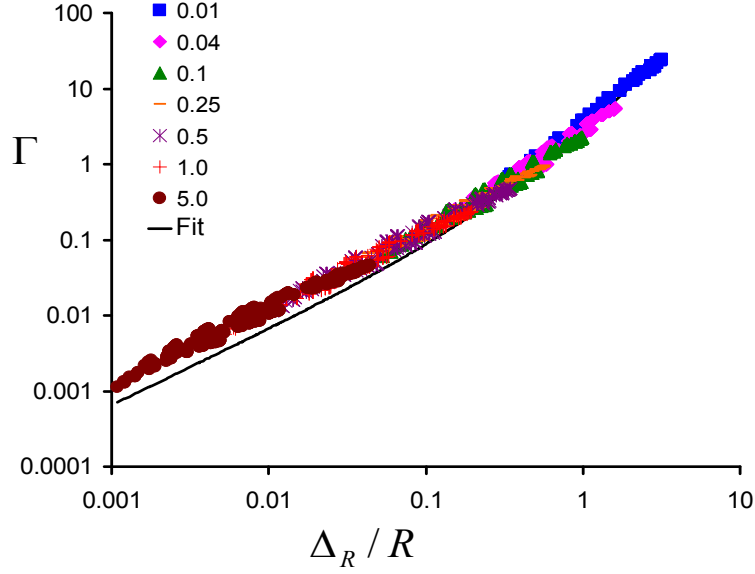
Figure 4.7: Numerical results for the normalized interfacial tension Γ as function of Δ_R/R for different radii. The results exihibit only little dependence on the specific μ values (chosen in the range $0.001 - 1$). Hence, to maintain clarity we do not distinguish the different μ values in the plot. The above results are well-fit by an indicated quadratic function of the form: $f(x) = 0.65x + 2.28x^2$.

Using $\Delta_R = f(BC, \mu, R)$, we expect:

$$\Gamma \equiv \frac{\gamma}{\Pi R} = f(\frac{\Delta_R}{R}, \frac{\mu}{R}). \tag{4.42}$$

In Fig. 4.7 we display our results for Γ as a function of Δ_R/R for different radii. We observe that in this representation, the γ values collapse onto a single universal curve which is (practically) independent of the specific μ/R values. Moreover, we observe that the functional form of the curve can be well fit to

a quadratic of the form:

$$\Gamma = a\left(\frac{\Delta_R}{R}\right) + b\left(\frac{\Delta_R}{R}\right)^2, \qquad (4.43)$$

where a and b are $O(1)$ constants determined by fitting our data. On physical terms, the above results can be understood based on the arguments used to motivate the nondimensionalization of γ. One way to think about the interfacial tension term is to think of it physically as the osmotic pressure contribution arising from the evacuation of polymers from a layer of thickness Δ_R surrounding the particle. For $\Delta_R < R$, we expect this energetic term to be of the form $4\pi R^2 \Delta_R \Pi$, i.e. $\gamma \simeq \Delta_R \Pi$. These considerations lead to

$$\Gamma \simeq \frac{\Delta_R}{R}, \qquad (4.44)$$

a functional form which is close to the result obtained by fitting our data. The second term in the fit of our numerical results can be understood as a manifestation of the curvature effects on γ which arises for the case when the depletion thicknesses become comparable to or larger than the radius of the particle.

We now discuss the implications of our results in the context of the experimental observations mentioned in the introduction. Explicitly, our numerical results indicate that the insertion free energy for a spherical particle

in a semiflexible polymer solution follows a functional relationship of the form:

$$F_1 = \Pi \frac{4}{3}\pi R^3 \left[1 + 1.95\frac{\Delta_R}{R} + 6.8\left(\frac{\Delta_R}{R}\right)^2 \right] \text{ for } \frac{\Delta_R}{R} \leq 3.0. \qquad (4.45)$$

It can be see that the size dependence of the insertion free energy exhibits a complex functional form which depends on R through through both the osmotic pressure and interfacial tension term. For large particles, the first term above is expected to dominate and the insertion free energy scales as R^3 and will exhibit a concentration dependence identical to that of the osmotic pressure. For smaller particles, the interfacial tension terms are expected to dominate and the insertion free energy is expected to be a function of Δ_R/R. In such a case, using the results discerned in eqs. (4.29), (4.30) and (4.39) we can deduce that depending on the regime of values for Δ_R/R, F_1 can exhibit a particle size scaling dependence of the form R^β with β in the range $1-2$. In a similar manner, the concentration dependence of the insertion free energy is also expected to exhibit a complex dependency on the parameters BC and μ whose functional form (not expressible as a simple power law) depends on the value of radius of the particle relative to the depletion thickness. These insights may serve to explain the different functional forms and exponents noted in the experimental literature regarding the solubility and mobility of small particles and proteins in semiflexible polymer solutions.[140]

4.6 Conclusions and Outlook

In this chapter, we presented a numerical approach to the solution of the self-consistent field theory for the structure of semiflexible polymer solutions near spherical surfaces. We used the framework to study the depletion characteristics of semiflexible polymers near colloids and nanoparticles. Our results suggest that the depletion characteristics of semiflexible polymers exhibit more complex parametric dependencies than their flexible counterparts. Explicitly, the polymer density profiles (and the depletion thicknesses) were shown to be depend sensitively on the polymer concentrations, the persistence lengths and the radius of the particles. Broadly, two categories of features were identified based on the relative ratios of the persistence lengths to the correlation length of the polymer solution. For the flexible limit of semiflexible polymers, the correlation length proves to be the critical length scale governing both the depletion thickness and the curvature effects. In contrast, for the rigid limit of the semiflexible polymer solutions the depletion thickness and the curvature effects were shown to be dependent on a length scale which was determined by an interplay between the persistence lengths and the correlation length. This led to nontrivial scaling laws governing the concentration and radii dependence of the depletion thicknesses. Our study also highlighted the manner in which the above features impact upon the insertion free energies of small probes in semiflexible polymer solutions.

Several directions present itself for future study. The framework presented in this chapter can be straightforwardly used to address the properties

of confined semiflexible polymers and their solutions. Another extension of the present study would be to address the effect of attractive interactions between the polymer and probes. Such effects are bound to be of importance in biological contexts, and compared to the case of flexible polymers, the results for semiflexible polymers are still lacking. As an immediate extension to this study, in the following chapter, the density profiles near the particles (provided by this numerical approach) are utilized as input to a predictive method for barrier properties of polymer composites.

Chapter 5

Influence of Interfacial Layers upon the Barrier Properties of Polymer Nanocomposites

5.1   Introduction

There has been a long history of development of theoretical models for predicting the effective properties of "composites" comprising of one or more dispersed phases in a homogeneous matrix.[159, 160] At the simplest level, such models concern with the question "what are the effective properties of the medium for specified properties of the matrix and the dispersed phases ?" A variety of theoretical techniques ranging from volume averaging methods, cluster expansions and renormalization group theories have been used to predict the mechanical, electrical, rheological and barrier properties of media made up of statistically homogeneous and ordered dispersions.[160, 161, 162]

The present work was motivated by a desire to explore a "numerical homogenization" framework which which allows the prediction of macroscopic effective properties of composite media for a specified (in principle, arbitrary)

distribution of local properties. Motivation for such a framework arose from the many recent observations of polymer nanocomposites (PNCs) where classical models of effective properties of composite media have been shown to fail in predicting their macroscopic property charcteristics.[163, 49, 164] While the reasons for such failure has not been conclusively established, it has been speculated that such discrepancies arise primarily due to two features missing in the classical composite theories:

(i) The complex structural characteristics of the PNCs: Many of the common nanofillers used in PNCs are characterized by strong van der waals interparticle attractions which promote their aggregation [165]. Moreover, the effective interactions between nanofillers are also influenced by the polymer-filler interactions, and if the latter are unfavorable it leads to conditions favoring the agglomeration of the fillers. Many of the classical composite theories assume either statistically homogeneous or ordered dispersions, and do not account for the complex structural characteristics arising due to the aggregation of the fillers.

(ii) Interfacial property characteristics: A significant feature which distinguishes PNCs from traditional composites are the presence of significant amounts of polymer-filler interfaces and their influence upon the macroscopic properties. Indeed, many experiments have clearly demonstrated that polymer-surface interactions can lead to properties for polymer layers which are significantly different from that of the bulk polymeric material [166]. Most classical models for dispersed media and composites treat the interface between dis-

persed media either as a boundary condition for the field equations or by incorporating a fictitious "interfacial phase" characterized by properties different from that of the bulk polymer. Such approaches are expected to be reasonable only for situations where the length scale of variation of the interfacial properties is much smaller than both the radii of the fillers and the variations in the macroscopic fields (stress, electrical fields etc.) set up due to the introduction of the filler. Whereas, in reality, the interfacial layer may exhibit a continuous gradation in its properties extending to significant distances relative to the size of the fillers.[167, 168, 169, 170] It has been suggested that the lack of such effects in the classical composite models is a possible reason for their shortcoming in modeling the properties of PNCs.

In this work, we wish to go beyond approximate analytical approaches and instead seek to develop a direct numerical approach which can potentially incorporate both arbitrary structural information of the fillers and specified interfacial characteristics to predict the macroscopic properties of PNCs. Specifically, our objective is to develop a methodology which can take in as input the structural characteristics of the particles (determined either experimentally or from theoretical models and/or simulations) and information for the local, interfacial properties and ultimately be able to predict the effective macroscopic properties of the dispersion. In this chapter, we demonstrate such a methodology by its application to the context of barrier properties of polymer nanocomposite membranes, an issue which has attracted significant attention in the recent literature due to reports of observations counterintutive

to composite theories (reviewed in the next section). However, our framework can also be readily extended to predict the role of interfaces upon macroscopic properties such as the mechanical moduli, conductivity etc. of polymer nanocomposites.

5.2 Barrier Properties of PNC membranes

Polymer membranes have long been used as barrier materials to inhibit the transport of gas and/or vapors. This property has greatly been exploited in the food packaging industry, where typically it is critical to limit the exposure of water vapor and oxygen from different foods.[171] Polymer membranes have also been used in the gas separation industry, where the preferential transport of gases in a mixture through polymer membranes provides an avenue for their separation.[172, 173, 174, 175] In such applications, the barrier properties of polymers are quantified by a quantity termed the permeability (P) of the polymer to a penetrant. Explicitly, the solution-diffusion model breaks these contributions to permeability down as: $P = DS$, with D being the diffusivity of the gas (measuring the mobility of the gas in the polymer) and S defined as the solubility of the gas in the polymer (quantifying the amount of gas dissolved in the polymer). Methods to tune the barrier properties and selectivity of polymer membranes usually focus on means to tune either the solubility of the penetrant in the membrane, or alternatively, hinder the diffusional transport of the penetrant.[176, 177, 178, 179]

A common approach to tune the diffusional transport of penetrants in

polymer membranes involves incorporating fillers with sizes on the order of microns.[176] It is believed that such fillers block the diffusion paths available for the penetrants and thereby enhance the barrier properties of membranes. Based on this physical picture many theoretical models have also been proposed which incorporate particle and polymer properties, and predictively quantify the diffusivity of penetrants in polymer-particle composites.[159, 180, 181, 182] Counterintuitive to such expectations, recent experiments have discovered that in certain scenarios, using spherical fillers of sizes of the order of a few nanometers in a polymer membrane may enhance the membrane's permeability and selectivity to large molecule penetrants.[183, 184, 185] Specifically, experiments by Merkel *et al.*[11] revealed that upon embedding glassy poly(4-methyl-2-pentyne) (PMP) with fumed silica nanoparticles (NP), the permeability of the membrane to methane was enhanced. Moreover, the addition of such NPs was also shown to increase the selectivity of the membrane to n-butane (larger molecule) over methane (smaller molecule). (Such non-intuitive penetrant size favorability in the selectivity of a membrane is characteristic of what are termed *reverse-selective membranes*.) The original observations were rationalized on physical grounds by suggesting that the NPs disrupt the packing of the polymers in the polymer-particle interfacial region, which in turn causes the layers of polymer around the NP to have higher free volume than the bulk regions of unperturbed polymer. It was speculated that the latter was responsible for the enhanced diffusion transport of penetrants relative to the bulk polymer membrane. Evidence supporting such claims were provided

113

by measurements demonstrating a reduction in density upon the addition of NPs (where the density reduction was measured relative to an additive density calculated by considering volume contributions of the polymer and particle densities).[186] Also, positron annihilation lifetime spectroscopy measurements have shown a shift towards larger values of void sizes as the NP loading was increased.[11]

Subsequent to the above experiments, there have been some theoretical investigations into the origins of the non-intuitive behavior of composite membranes made of mixtures of polymers and nanofillers (PNCs). Continuum mechanical composite theories such as the Maxwell's effective medium model (MM) for the effective diffusivity of a 2-phase dispersed system,[159, 180, 187, 188] considers only the presence of two phases, viz., the particle and the medium (polymer phase) with their specific properties. Since the particles in the membranes are usually nonporous, the fillers only function as an obstacle to the penetrant. Thus, trends from such 2-phase models can only predict a *decrease* in membrane permeability upon addition of fillers. To overcome this limitation, research efforts have probed the role of modified polymer interfacial properties by the use of 3-phase models which posit the presence of three well-defined phases, the particle, polymer medium and an "interfacial region" which is assumed to have its own physical properties.[189, 190, 36] One such model was used by Xue et al.[191] who modeled the PNC membrane as a two dimensional (2D) system having a certain configuration of particles (modeled as disks) possessing interfacial layers with designated interfacial

thickness and penetrant diffusivity. Using this approach they demonstrated that the penetrant diffusivity grew exponentially with particle area fraction and increased with increasing interfacial layer thickness. Moreover, their study revealed anisotropic networks of particles (i.e. irregular connections of particles linked by overlapping interfacial regions) and percolation of interfacial layers enhanced diffusivity more substantially than dispersed non-overlapping interfacial layers. While such a model was able to study the effects of the interfacial layer thickness and the impact of percolation of such layers upon the macroscopic diffusivity, details regarding the origin of the interfacial layers, its properties and the consequences of potential overlap of interfacial layers were ignored. Moreover, the methodology was implemented in a 2D framework, and hence quantitative applicability of the results to three dimensional (3D) systems is not known.

A more detailed undertaking for the above experimental results was the model proposed by Hill.[35, 192] In this model, a relation between local free volume and local density was used to argue that the reduction in polymer density near surfaces was responsible for the enhanced diffusivity of penetrants in the interfacial layer. The depletion density profiles for polymer solutions was embedded (albeit, with a depletion thickness which was considered as a fitting parameter) within a hydrodynamic theory which accounted up to the influence of two-body interactions. Within this model, the effects of particle and penetrant size were incorporated, and trends representative of experimental results (including the reverse-selectivity effect) were reported in qualitative

agreement with the experiments. Despite capturing most of the qualitative physics accurately, Hill's model[35, 192] utilizes density profiles based on theories for polymer solutions near flat surfaces whose applicability for polymer melts near highly curved surfaces (such as NPs) is suspect. Moreover, considering the perturbative manner by which the interparticle interactions are treated and the neglect of effects arising from the overlap of interfacial layers, the model is expected to be applicable only for low to moderate concentrations of fillers.

As elaborated in the preceding section, the present work is motivated by the desire to develop a framework which goes beyond the approximate analytical approaches and instead seek a more direct numerical approach to quantify the impact of both structural complexities of the dispersion and the interfacial characteristics upon the macroscopic properties of PNCs.[193, 9, 194] Specifically, in the context of the above experiments, our goal is to develop a "homogenization" procedure which allows us to predict the macroscopic effective diffusivity for a specified (in principle, arbitrary) distribution of local penetrant diffusivities. We demonstrate that this methodology can be used fruitfully to (numerically) characterize the effects of multibody interactions, role of continuously varying interfacial layers and the impact of overlap of interfacial layers.

A second, related objective of this work is to use the above approach to improve some of the deficiencies elaborated in the context of the earlier research efforts on barrier properties of PNCs. Specifically, we wish to address:

(i) The role of *polymer matrix rigidities*: Most highly permeable membranes tend to be composed of rigid amorphous polymers with high free volumes.[195, 196, 197] Nanofillers have been speculated to disrupt the packing of rigid polymers more significantly compared to their flexible analogs. In fact, Merkel et al.[198] explicitly invoke polymer rigidity as an important factor in rationalizing and contrasting their observations with earlier results. We wish to address whether indeed the rigidity of the polymer plays an important role in modulating the barrier property behaviors observed in PNCs.

(ii) The role of *particle curvatures*: Our interest in this issue arises from the contrasting behaviors exhibited by PNCs and traditional composites (referring to composites having fillers with dimensions much larger than nanometers).[11] While these differences have typically been rationalized by invoking the sizes of the interfacial layers relative to the particle size, such explanations ignore the possible curvature dependence of the interfacial layers themselves. We propose to account for such effects to discern quantitatively the interplay of curvature and interfacial characteristics upon the macroscopic barrier.

In this work, we propose to broadly retain the physical picture proposed in the work of Hill[35, 192] which ascribes the interfacial properties to free volume effects resulting from the reduced polymer densities near particle surfaces. However, we use the results of a more realistic model of a compressible, semi-flexible polymer melt near a spherical particle to deduce the polymer density profiles near particle surfaces.[40] This model allows us to account for the polymer rigidity in a systematic manner and, thereby, probe the interplay between

117

polymer packing and the curvature of the particle in determining the density profiles of the polymer. The results of this approach is fed into a multibody simulation methodology which accounts approximately for the overlap of the polymer density profiles (and hence the local penetrant diffusivities via a free volume model identical to that employed in Hill[35]). However, the simulation approach rigorously accommodates the multibody particle interaction effects which influence the effective macroscopic diffusivities. Using such a framework we calculate the effect of various parameters upon the penetrant diffusivities in PNC membranes. Our results indicate that an increase in polymer rigidity and/or a decrease in particle size greatly contribute to the depletion of polymer near the surface of a NP, as well as significantly enhance the diffusion of a penetrant in a PNC. In addition, we find that at moderate particle concentrations, multibody effects become appreciable for the rigid polymer and/or small particle regimes.

The rest of this chapter is split into three main sections. Following this introductory section we define our model and outline the manner by which the local interfacial properties are obtained (section 5.3.1) and utilized in a 3D framework to capture the multibody effects of PNCs (sections 5.3.2 - 5.3.4). In section 5.4, the results of our study are presented where the effects of particle size (section 5.4.1), polymer rigidity (section 5.4.2), and penetrant size (section 5.4.3) on the macroscopic penetrant diffusivities in PNCs are discussed. Our results are also compared to existing experimental data in section 5.4.4, while our multiscale method is discussed with regards to earlier

developed theoretical efforts in section 5.4.5. The final section (5.5) provides a summary of our findings and highlights some potential future directions.

5.3   Description of Modeling and Simulation Framework

The overall modeling/simulation framework we use involves three components: (i) Obtaining the interfacial layer characteristics using a microscopic polymer model; (ii) Creating a polymer density/diffusivity landscape for a configuration of particles; (iii) Obtaining the macroscopic penetrant diffusivity for a specified local diffusivity landscape. Each of these steps are elaborated in the sections below.

5.3.1   Obtaining Interfacial Layer Characteristics

Inherent to our framework is the idea that polymer densities are modified (relative to the bulk density) near the particles, and such changes lead to the modified penetrant diffusivities near the particles. We note that most membranes are used in their glassy, nonequilibrium state,[197] for which predictive models characterizing polymer packing are not established. As an approximate means to characterize the polymer packing (and density profiles) near the surfaces, we propose to use the model of compressible, semiflexible polymer melts. Such a model utilizes a coarse-grained framework, where details on the scale of monomers are eschewed and instead the the polymer chains are

represented on the scale of the Kuhn segment lengths.[146] In such models, the density profiles near surfaces exhibits smooth, nonoscillatory variations from the bulk values to a surface value determined by the interaction of the polymers with the particle. The local density of the polymer can in turn be related to the local free volumes and hence the local penetrant diffusivities.

Recently, we have developed a self-consistent field theory (SCFT) based approach for a single spherical particle in semiflexible polymer *solutions*.[199] In this SCFT based model, there was assumed to be no energetic interactions between the particles and the polymers, and thus the particle was modeled as a hard sphere which excludes polymer conformations penetrating its surface. The polymer was modeled as a worm-like chain[200, 146] and the entire system was modeled within a grand canonical framework which allowed us to maintain a prescribed solution concentration. Using such a model, the local polymer segment density profiles near the particle predicted by our theory revealed an interfacial layer surrounding the particle that was depleted of polymer segments (relative to the bulk density). These density profiles, characterized by an interfacial thickness (Δ), were shown to vary in a complex manner upon changing the polymer rigidities and particle sizes. Since the numerical and formulation of this model was presented in detail in Chapter 4, below we mainly highlight the modifications used for this work and the parameters explored for the present study.

The above model is pertinent to the present study in view of our objective to study the impact of conformational rigidity upon the overall barrier

properties of PNCs. Towards this goal, we extended our earlier model which was restricted to polymer solutions to treat the case of compressible polymer melts with density fluctuations characterized by a simple free energy functional of the form:[201, 201, 202]

$$F = \int d\mathbf{r} \kappa^{-1} \left(\frac{\rho(\mathbf{r})}{\rho_b} - 1 \right)^2, \qquad (5.1)$$

where ρ_b stands for the bulk density of the polymer and κ represents a measure of the compressibility of the polymer melt. With the above modification, our model is characterized by three parameters: κ, the radius of the particles (R), and the persistence length (μ) of the polymer. In the present work, we fix the κ parameter at a nondimensional value of $\kappa R_g^d / N^2 = 0.1$ where R_g denotes the radius of gyration of the polymer and N the number of polymer segments in the polymer. Alternative choices for κ parameter led to a modification of the results only at a quantitative level. To discern the effects of particle curvature, R (nondimensionalized by polymer contour length) was varied from 0.1 to 5 while μ (nondimensionalized by polymer contour length) was chosen to be between 0.001 and 1.0. We note that μ quantifies the rigidity of the polymer, and a value of 0.001 represents a situation more akin to flexible polymers, whereas a value of 1.0 represents a situation corresponding to rigid polymers.

A selection of local density profiles for the semiflexible polymer melt near a particle are shown in Fig. 5.1 for the $\mu = 0.1$ as a function of R (Fig. 5.1(a)) and for $R = 0.25$ as a function of μ (Fig. 5.1(b)). All the parameter sets shown in Fig. 5.1 have similar qualitative behavior: at the surface of
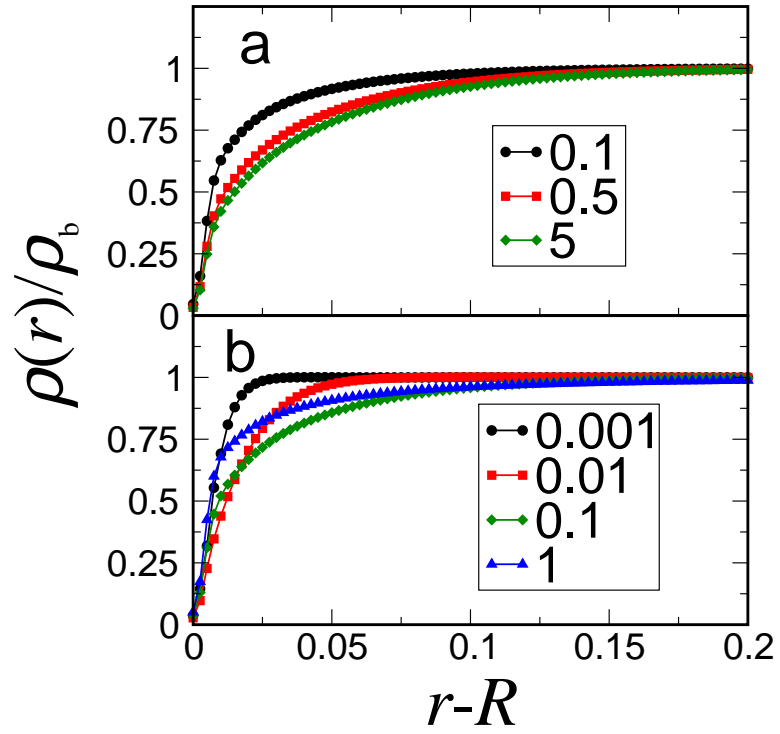
Figure 5.1: Local density profiles generated by SCFT based simulations for a compressible semiflexible polymer melt surrounding a particle. In plot (a) the persistence length (μ) was held fixed at 0.1 while the particle radius (R) was altered from 0.1 to 5. In plot (b) R was fixed at 0.25 and μ was varied from 0.001 to 1.

the particle, the normalized polymer density vanishes. On moving away from the surface of the particle, the density increases to the normalized bulk density value of unity. These results support the hypothesis that introduction of particle fillers lead to regions of depleted polymer, which may in turn promote the enhanced penetrant movement in the polymer composite.

We note that many of the earlier models incorporate interfacial effects through an interfacial "layer" of specified thickness and properties.[189, 190, 36, 191] To facilitate a comparison with such approaches, from our numerical density profiles we computed a depletion thicknesses Δ defined by the equation:

$$\frac{4}{3}\pi \left[(R + \Delta)^3 - R^3\right] = 4\pi \int_R^\infty \left[1 - \phi(r)\right] r^2 dr, \tag{5.2}$$

where $\phi(r)(\equiv \rho(r)/\rho_b)$ is the local density of polymer segments normalized by its bulk density. Eq. (5.2) calculates the volume that the number of monomers depleted (relative to bulk) around the NP would occupy at bulk density. Figs. 5.2(a) and 5.2(b) present the results for Δ/R and Δ as a function of μ for different particle sizes. It is seen that the ratio Δ/R is very small for large particles (*e.g.* $R = 5$) but becomes $O(1)$ for smaller particles ($R = 0.1$). This result confirms that the volume of the interfacial layers become substantial (relative to the particle volume) for the case of nanoparticles. However, Fig. 5.2 (b) clearly demonstrates that there is also an inherent curvature effect, viz., that Δ values do become smaller for smaller particles. This result is seen visually in Fig. 5.1(a), where the depletion of polymer increases as R is increased from 0.1 to 5. Considered in the context of Fig. 5.2(a) our
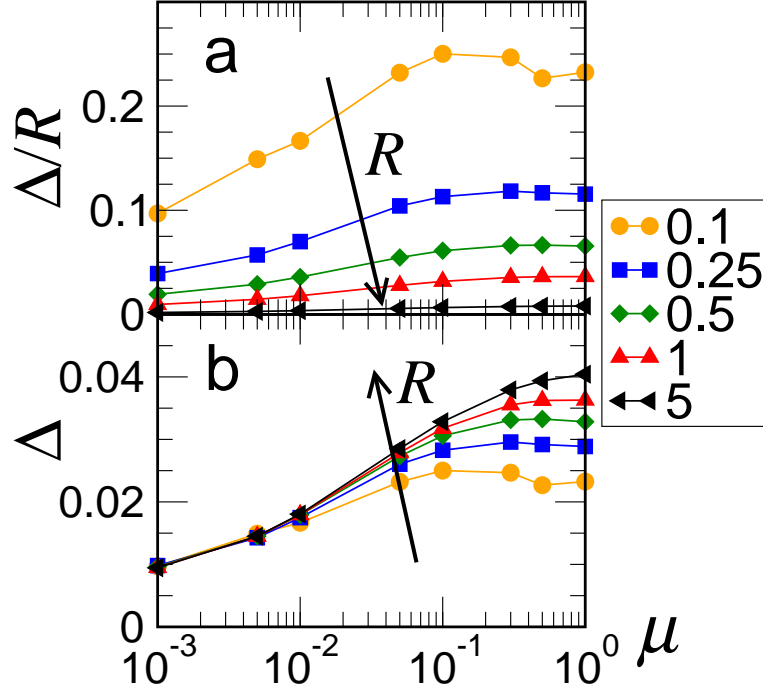
Figure 5.2: Interfacial layer thickness dependence upon particle radius (R) and polymer rigidity (μ), where in (a) Δ is scaled by the particle's radius and in (b) Δ is scaled by the polymer's contour length.

results demonstrates that the relative volumetric effect of the depletion layers dominate the curvature effect for the range of radii and rigidities probed in our simulations.

A second result, which is evident from Fig. 5.2(a), shows that the interfacial thicknesses become larger upon increasing the rigidity of the polymer matrices. This effect is visually observed in Fig. 5.1(b), when holding $R = 0.25$, an increase in the depletion near the particle surface can be seen upon changing μ from 0.001 to 0.1 (in other words, upon transitioning from the flexible polymer limit to the more rigid polymer limit). This result confirms that

introduction of particles lead to a longer length scale disruption of polymer packing in rigid polymers relative to flexible polymers.

5.3.2 Role of Multibody Effects

An important outcome of the results presented in the preceding subsection is that it highlights that multibody interactions may potentially play a significant role in influencing the magnitudes of the macroscopic diffusivities. To elucidate this issue, we first note that for rigid polymers, the interfacial density profiles display long ranged variations in density profiles relative to the size of the particle. Indeed, it is seen from the density profiles displayed in Fig. 5.1(b) for $R = 0.25$ that while the density profiles are perturbed up to a distance $\sim 0.1R$ for $\mu = 0.001$, such profiles display a perturbation extending up to $\sim 0.5R$ for $\mu = 0.1$. While the origins of these perturbations were discussed in Chapter 4, below we point out its implications in the context of the problem considered in this chapter.

The above long ranged variations in densities can lead to two kinds of multibody body effects which influence macroscopic properties such as the penetrant diffusivities. The first kind (MB1) is purely a particle interaction effect and manifests even in the absence of the interfacial layers. This effect arises from the impact of the presence of a second (or more) particles upon the *penetrant* concentration fields set up by a single particle. The latter is responsible for the particle concentration dependence of the penetrant diffusivity noted in models such as the 2-phase MM.[35, 192, 203, 204] In the case

when the particles have an interfacial layer, MB1 effects can be expected to manifest when the penetrant concentration profile set up by a single particle *along with its interfacial layer* start to overlap with the concentration fields set up by other particles (with their interfacial layers). However, such MB1 effects are now expected to manifest at a concentration determined by the volume of the "pseudo particle" comprising of the particle along with its interfacial layer. Due to the relative expanse of the interfacial layers, the particle concentrations at which such MB1 effects manifest are expected to be significantly lower than in the absence of such interfacial layers.

A second kind of multibody effect (MB2) arises due to the potential overlap of polymer interfacial layers. Indeed, the polymer density profiles depicted in Fig. 5.1 are expected to be modified upon the introduction of a second (or more particles) in the vicinity of the first particle.[149] Such effects are expected to become important if the particle concentrations are such that the range of perturbations of the polymer densities around particles start to overlap. Yet again, we expect such effects to manifest at very low particle concentrations for cases involving small particles and/or rigid polymers!

The above observations point to the need to accurately capture the effects of multibody interactions upon macroscopic properties especially for situations involving rigid polymers and/or small particles. Explicitly, the above arguments suggest that an accurate quantification of the interfacial effects upon the diffusivity of penetrants requires an approach to obtain: (i) The polymer density (and penetrant diffusivity) map for a given concentration and con-

figuration of particles while accounting for the overlap of interfacial layers; (ii) The macroscopic diffusivity arising from such a complex polymer density/diffusivity landscape. In the following sections, we detail our approach to address these issues.

As an aside, we note that the above discussed long range effects are severely underestimated in interfacial shell models. Indeed, it is seen from the results depicted Fig 5.2(a) that for $R = 0.25$ and $\mu = 1.0$ we have $\Delta = 0.11R$ (in contrast to the density perturbations that extend up to $\sim 0.5R$). The latter illustrates the pitfall of such shell models, wherein the range of perturbations are underestimated. Consequently, establishing a correspondence to experimental results typically requires the assumption that the interfacial properties differ significantly from the bulk value.[191, 205, 36] We provide more clearer demonstrations of this breakdown in the section on results and discussion where we compare the results of the multibody simulation framework to the corresponding results from the 3-phase MMs which uses such a shell-like description of the interfacial layer.

5.3.3 Transforming Interfacial Layer Properties into A Diffusivity Landscape

We propose a unified framework which incorporates continuously varying interfacial layer properties, overlap of interfacial layers, and free volume theory to estimate the diffusivity landscape for a penetrant. In principle, structurally representative samples of the particle dispersion can be created using

either experimental input and/or simulations wherein the interactions between the nanofillers are specified. For the present work, we relied on a random configuration of particles generated via a Molecular Dynamics simulation of Lennard-Jones particles with potential parameters,[1] σ and ϵ, and mass set to unity.[123]The simulations were run in an NVT ensemble, and several snapshots were saved throughout each simulation. This allowed access to different configurations of particles so that the final predictions for the composite's macroscopic diffusivity (details for this given later in the section) could be averaged over these configurations. Also, using this approach ensured configurations of non-overlapping particles and set the 3D layout for which the interfacial layers would be mapped onto.

The first step in determining the local penetrant diffusivities was to assign the local polymer densities at an arbitrary location in the system. While the interfacial layer's density profiles deduced in SCFT simulations provide information about the local polymer arrangement around a single particle, such densities need to be corrected to account for the superposition effects arising from the neighboring particles. In order to generate 3D density profiles of particles with these overlapping interfacial regions, the composite system is represented as a grid of points, each having a local normalized density ($\phi(\mathbf{r})$) associated with it. The grid size was chosen to be 5% the radius of the NP; this choice assumes any resolution of an interfacial layer below this threshold

---

[1]The MD simulations generated configurations of simple, non-overlapping particles by using a Langevin thermostat with the temperature set at $1.0\epsilon/k$ and the friction coefficient set to $0.5\tau^{-1}$, where $\tau = \sigma(m/\epsilon)^{1/2}$ with m defined as the mass. The length of the cubic simulation box was held at 3.75σ.

is unnecessary to capture in this model. The SCFT local density profiles are then superposed on top of the 3D particle configurations using a superposition approximation:

$$\phi(\mathbf{r}) = \prod_{i=1}^{N} \phi_i(|\mathbf{r} - \mathbf{r}_i|), \qquad (5.3)$$

where $\phi(\mathbf{r})$ denotes the prediction for the normalized density at a position $\mathbf{r}$ and $\phi_i(|\mathbf{r} - \mathbf{r}_i|)$ represents the SCFT determined normalized density profiles at a distance $|\mathbf{r} - \mathbf{r}_i|$ from the ith particle (cf. Fig. 5.1). The above product rule has been previously shown to accurately predict the concentration profile between two spheres immersed in an ideal polymer solution, and we extend the idea here to the case of a polymer melt and for the situation involving many particles.[206]

Combining the local interfacial density profiles with a 3D particle configuration results in a 3D density profile for the polymer composite system. A representative 2D slice of such a density profile is shown in Fig. 5.3; note that the density inside a particle is zero because no monomers exist in this volume. Such 3D density profiles are generated for different parameters R, μ and particle volume fractions (ϕ_d) for different particle configurations. [1]

Once the 3D density profiles are created, the next step is to transform this to a 3D penetrant diffusivity map as input to the homogenization procedure described in the next section. In this regard, our model is identical to that of Hill[35, 207] where the local polymer density is related the local free

---

[1]We note that in reality, the particle size was actually fixed and R effects were accounted through the superposition of appropriate local density profiles for the specific value of R (as well as μ).
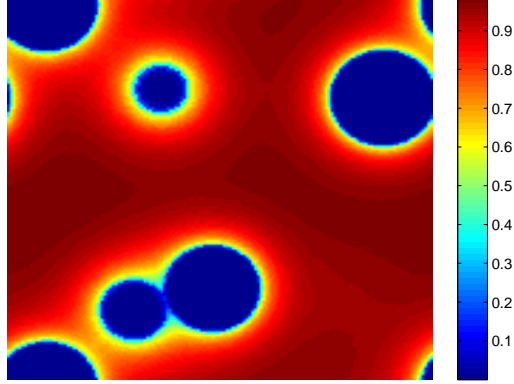
Figure 5.3: A two-dimensional slice of a three-dimensional normalized local density profile for $R = 0.1$, $\mu = 0.1$, and $\Delta = 0.025$.

volume of the matrix, and in turn to the local diffusivity of a penetrant (albeit, Hill implemented this in the context of one body density profiles). Explicitly,

$$\frac{D(\mathbf{r})}{D_b} = \exp\left[-\frac{v_m \phi^* (\phi(\mathbf{r}) - 1)}{(1 - \phi^* \phi(\mathbf{r}))(1 - \phi^*)}\right], \tag{5.4}$$

where $D(\mathbf{r})$ is the local penetrant diffusivity, D_b is the diffusivity in a bulk polymeric material with a homogeneous density, v_m is a parameter that scales as the ratio of the penetrant's volume to the average atomic volume composing the polymer, and $1 - \phi^*$ represents the fractional free volume of the pure polymer. In the present study, $1 - \phi^*$ was fixed at 0.29, which is the fractional free volume of poly-[1-(trimethylsilyl)-1-propyne] (PTMSP). PTMSP was chosen since it was shown experimentally to have an enhancement in free volume upon adding fumed silica NPs.[163] We allow v_m to be 0.7 and 1.6 to study penetrant size effects. Upon choosing these parameters Eq. (5.4), allows the
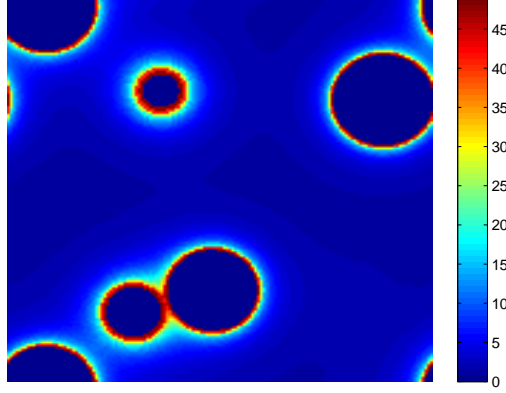
Figure 5.4: A two-dimensional slice of a three-dimensional diffusivity profile attained from using Eq. (5.4) on the 3D local density profile in Fig. 5.3 and setting v_m to 1.6 and $1 - \phi^*$ to 0.29.

3D density map to be trivially converted into a 3D diffusivity map (Fig. 5.4). The latter represents the penetrant diffusivity landscape accounting for continuously varying interfacial layer properties and the multibody effects (MB2) arising from the overlap of interfacial layers (in an approximate manner within the framework of Eq. (5.3)).

As an aside, we note that the functional forms relating the local solubility to the local density can also be used in the above construct to generate a solubility and hence a permeability map. The local permeabilities, can then be embedded in a framework similar to that described in the next section to deduce a macroscopic permeability. In this work however, we restrict ourselves to study the characteristics of the macroscopic diffusivities of penetrants.

5.3.4 From a Diffusivity Map to Macroscopic Diffusivity

To obtain the macroscopic diffusivity for a specified diffusivity map, we use a method termed as the random walker (RW) simulation method. This method, proposed by Van Siclen,[208] has been developed and implemented earlier to predict transport coefficients for finite composite materials (without any interfacial layers). This simulation technique views a composite system as a grid of local properties (in this case local diffusivities) and lets a random walker roam these grid points. Movements of this RW are determined by probabilities proportional to local diffusivities of nearest neighbors,

$$P_{ij} = \frac{D_j}{D_i + D_j}, \qquad (5.5)$$

where P_{ij} is the probability to move from site i on the diffusivity grid to site j and D_i and D_j are the local diffusivities of sites i and j. The diffusion of the walker (D_w) is then extracted from the Einstein's relation,[123]

$$D_w = \frac{\langle R^2 \rangle}{6t}, \qquad (5.6)$$

where t is the time the walker has traveled and $\langle R^2 \rangle$ is the mean-squared distance the walker has traveled. With the walker's diffusivity one can achieve a prediction of the macroscopic diffusivity for the local diffusivities by the simple relation $D = D_w \langle D(\mathbf{r}) \rangle$, where $\langle D(\mathbf{r}) \rangle$ is the volume average of the

local diffusivities from the 3D grid.

A RW simulation was performed on each 3D diffusivity map generated from the procedure stated above in this section. For each parameter set, four different particle configurations and hence diffusivity maps were created, and used in separate simulations allowing for an average of the macroscopic diffusivity. To explicitly delineate the influence of interfacial effects we considered the results of three models:

(i.) *Full Scale Model*: A polymer composite was modeled as particles surrounded by a continuously varying interfacial layer, with the density and diffusivity profiles generated as described in the preceding section.

(ii.) *3-Phase Model*: Interfacial layers modeled as shells with a specified thickness (Δ) and interfacial diffusivity. Regions outside the interfacial region were assumed to have bulk properties. Δ was calculated by using the density profiles (generated from our SCFT based simulations) in Eq,(5.2). The interfacial diffusivity of this region was obtained by setting $\phi(\mathbf{r})$ equal to zero in Eq. (5.4). This model mimics the construct used in the 3-phase MM for which it has been predicted that[190]

$$\frac{D_{3PMM}}{D_b} = \frac{D_{eff} + 2D_b - 2(\phi_d + \phi_I)(D_b - D_{eff})}{D_{eff} + 2D_b + (\phi_d + \phi_I)(D_b - D_{eff})}, \qquad (5.7)$$

where D_{3PMM} is the macroscopic diffusivity determined by the 3-phase MM (3PMM), ϕ_d is the volume fraction of particles, ϕ_I is the volume fraction of interfacial layers, and D_{eff} is the effective diffusivity of the

particle and interfacial layer combined. This effective diffusivity D_{eff} is determined as

$$D_{eff} = D_I \frac{1 - \phi_s}{1 + \phi_s/2},\qquad(5.8)$$

with D_I being the interfacial diffusivity determined from Eq. (5.4) (upon setting $\phi(\mathbf{r}) = 0$ in the interfacial region) and $\phi_s = \phi_d/(\phi_d + \phi_I)$. With the knowledge of Δ from Fig. 5.2(b) (which was calculated from Eq. (5.2)), ϕ_I can easily be determined. As we discuss below, for representative parameters, the results of our RW simulation (when viewed from this shell-like framework) matched very closely with the results of the above 3PMM (Eq. (5.7)). Whence, in the subsequent sections we directly compare our numerical results for the full scale model with that of the analytical result Eq. (5.7).

(*iii.*) *2-Phase Model*: In this model, there is no interfacial layer, and the system is composed of two phases: particle and polymer, with the particle being impenetrable and the polymer phase having bulk properties. This scenario is representative of classical composite models that are typically used to predict the reduction in barrier properties, and whose magnitude depends only upon the volume fraction of fillers. The equation defining this model is given by Eq. (5.8) except in this case $\phi_s = \phi_d$ and $D_I = D_b$. Again, below we demonstrate that upon sing 3D penetrant diffusivity profiles mimicking this setup, the results of our RW simulation approach matched very closely with the predictions of the above 2-phase MM (2PMM) (Eq. (5.8)) and hence in subsequent sections we

134
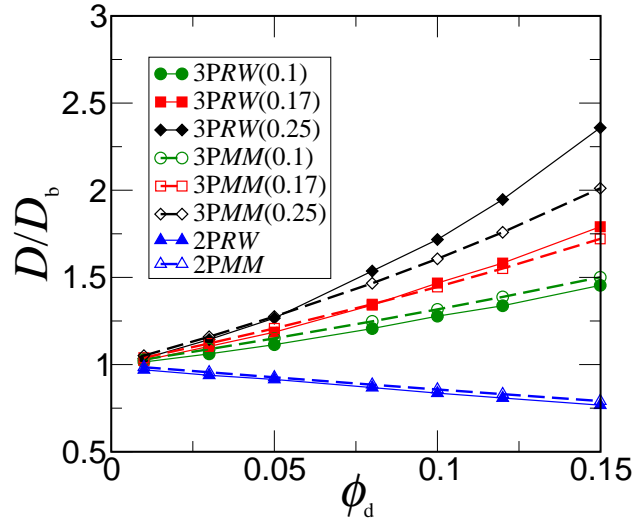
Figure 5.5: A comparison of the results of our multiscale approach to the two-phase (2P) and three-phase (3P) Maxwell model (MM). The filled symbols represent data from random walker (RW) simulations and the unfilled squares show predictions from the MMs. Δ/R values are enclosed in parentheses.

directly compare our numerical results with the analytical prediction of Eq. (5.8).

We tested the RW simulations in a 2-phase scenario (involving just the particles dispersed in a homogeneous polymer system) as well as a 3-phase scenario (where the particles were surrounded by an interfacial layer of specified diffusivity), the numerical results displayed in Fig. 5.5 are seen to match very well with the respective predictions of the 2PMM and 3PMM. The deviations apparent for $\Delta/R = 0.25$ may be rationalized as arising due to the overlap of interfacial layers, an effect not included in the 3PMM. In sum, the results in Fig. 5.5 suggest that the RW simulations can be used fruitfully to obtain the macroscopic diffusivities in our system.

As an aside, we note that alternate numerical homogenization techniques similar in spirit have also been proposed. Notable among these are the RW simulation method developed even earlier by Torquato et al.[209, 210], who used the first-passage-time technique to reduce the computational time required for simulations and applied it with success even to random digitized media. In fact, Torquato and coworkers have criticized the RW method of Van Siclen as being inaccurate for the scenario involving very large fluctuations in local properties.[211] However, since the techniques of Torquato *et al.* are harder to generalize to our system, and moreover, since our system does not exhibit such large fluctuations in properties we decided to adopt the method of Van Siclen. Moreover, the quantitative comparisons presented in Fig. 5.5 to the analytical predictions of 2PMM and 3PMM confirm the applicability of our RW method to the situations considered in this chapter.

5.4   Results and Discussion

In this section we discuss the results obtained for the parametric dependencies of the macroscopic penetrant diffusivities as a function of the particle radius (R), persistence length (μ), penetrant size (v_m), and the particle volume fraction (ϕ_d).

5.4.1 Nanoparticle size effect

In Fig. 5.6, the variation of the macroscopic penetrant diffusivity (relative to its value in a homogeneous polymer matrix) is displayed as a function of the volume fraction of the fillers for different particle radii R, and the inset to this plot gives the same diffusion data for a fixed particle loading corresponding to $\phi_d = 0.1$. In the results displayed, μ (in units of polymer contour length) is held constant at unity and v_m is set to 1.6, while R (in units of polymer contour length) is varied from 0.1 to 5. We have also probed the same particle size parameter range for other set values of μ (ranging from 0.001 to 1), however, we eschew presenting these results here since their behavior is qualitatively similar to the data displayed for $\mu = 1$ (Moreover, the following section discusses explicitly the persistence length effects at a fixed radii). On the same plot, results corresponding to the 3PMM defined by Eq. (5.7) and the 2PMM, defined by Eq. (5.8) are also displayed.

Overall, we observe an interesting dependence of the macroscopic penetrant diffusivity upon the particle size: for a given particle volume fraction ϕ_d, as the particle size R is reduced, we observe that the macroscopic diffusivity of the penetrant in the composite is enhanced (this trend is easily viewed in the inset of Fig. 5.6). Moreover, for the case of small particles, the penetrant diffusivities are seen to exhibit values higher than the diffusivities of the penetrant in the pure polymer matrix, an observation consistent with the "counterintuitive" experimental observations noted in the introduction.[183, 184, 185, 11] To understand the origins of these effects, we note that the role of particle
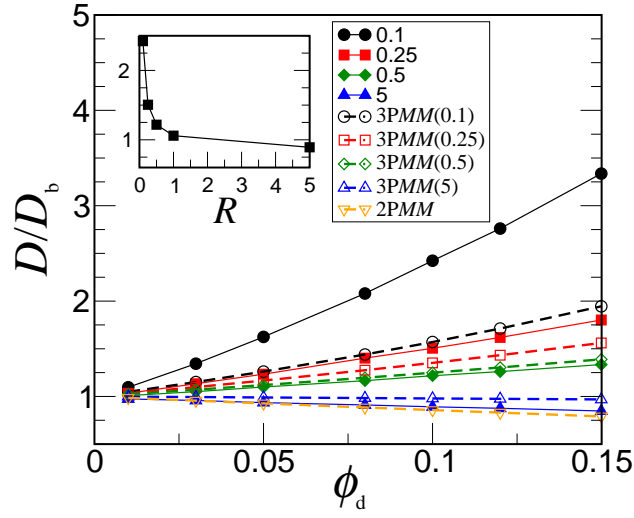
Figure 5.6: Effect of particle radius (R) on the macroscopic diffusivity of a PNC for $\mu = 1$. R was set to various values: 0.1, 0.25, 0.5, and 5; v_m was kept at 1.6. The filled symbols represent predictions from our multiscale model while the unfilled symbols represent predictions from both two-phase (2P) and three-phase (3P) Maxwell models (MMs). The diffusivities for $\phi_d = 0.1$ are shown in the inset as a function of the particle's radius. All R values are given with respect to the polymer's contour length.

fillers manifest in two competing roles: (1) the effect of its volume being an "obstacle" for a penetrant; and (2) the effect of particle generating regions "depleted" of polymers that promote penetrant movement. Moreover, Fig. 5.2(a) demonstrates that the depletion volume (or more explicitly, Δ/R) increases with a reduction in the particle size R. Hence we can conclude that as R decreases (at a constant ϕ_d), the depletion effects become more enhanced, leading to a corresponding increase in the macroscopic penetrant diffusivities that is seen in the inset of Fig. 5.6. For very small particles, the latter effect becomes dominant and leads to penetrant diffusivities which are much higher than the pure polymer matrix.

In comparing the results of our multibody simulations with that of the simplified 2- and 3-phase models, we note that for the case where $R = 5$, both our simulations and the 3PMM show quantitatively comparable results. From our discussion above, it is evident that this situation is representative of the "obstacle" effect, for which case, the interfacial effects, albeit present, are small relative to the overall obstruction offered by the particle. Moreover, due to the relatively small volumes of the interfacial layers, effects arising from the overlap of interfacial layers are also practically unimportant and do not manifest until much higher volume fractions. These features explain the semiquantitative accuracy with which the 2PMM and 3PMM predict our simulation results for large particles.

In contrast, for $R = 0.1$ (particles small relative to the polymers), a situation for which we observe a large enhancement in the macroscopic penetrant

diffusivities upon the addition of particles, it is also apparent that our results deviate significantly from the predictions of the 2PMM and 3PMM. While the deviations from the 2-phase model can be straightforwardly explained as resulting from lack of inclusion of the interfacial characteristics, the deviations from the 3-phase model is indicative of two effects: (i) the long ranged nature of the interfacial layers which are not accurately captured within the interfacial shell model; (ii) the substantial overlap of the interfacial regions and the corresponding multibody effects not captured in Maxwell like models. Parenthetically, we note that 3-phase models in other contexts have also had to some times use unphysically large parametric values for the interfacial properties to match the experimental results.[191, 205] Our results are consistent with such characteristics and shed light on the underlying reasons for such parameter fits.

Finally, for the case of $R = 0.5$ (particles comparable to the size of the polymers) we observe an interplay between the obstruction and the interfacial effects discussed above. Indeed, the results are representative of the scenario where the contrasting effects of "obstruction" vs "enhancement" balance each other for low volume fractions, after which the interfacial effects seem to dominate slightly (leading to an enhancement in the overall penetrant diffusivity by roughly 10% for $\phi_d = 0.15$). As might be expected from the smaller extent and effects of interfacial regions, the overall results are semiquantitatively captured by the 3PMM.

5.4.2 Effects of Polymer Rigidity

To probe the influence of polymer rigidity we fixed $v_m = 1.6$, and varied the persistence length from the flexible limit ($\mu = 0.001$) to the more rigid limit ($\mu = 0.1$). We consider the results for the small particle sizes $R = 0.1$ and larger particles $R = 0.5$ (results displayed in Fig. 5.7). The insets in Fig. 5.7 show the same diffusion data viewed from the $\phi_d = 0.1$ plane. For $R = 0.1$, Fig. 5.7(a), we observe that the macroscopic diffusivity is larger than the bulk value for all the rigidities (μ) probed. In addition, the inset of Fig. 5.7(a) clearly supports the idea that increasing the rigidity can lead to significant increases in the penetrant's macroscopic diffusivity. Indeed, it is already apparent from Fig. 5.2(a) that for the small particle limit, the particles are efficient in disturbing the packing of the polymers (an effect which increases with increasing rigidity) and consequently the depletion thicknesses are typically comparable to the radius of the particle. Consequently, it is not surprising for such small particles that the "obstruction" effect is overwhelmed by the "enhancement" effects.

Also shown in Fig. 5.7(a) is a comparison to the 3PMM (Eq. (5.7)). It is evident that the 2MM cannot predict the enhancements in diffusivities, and hence we refrain from presenting predictions for parameters where the simulations show no such effects. Overall, we observe that situations for which there are large interfacial layers (such as for $\mu = 0.01$ and $\mu = 0.1$), the 3PMM tends to under predict the results. The latter arises from the underestimation of the range of polymer density perturbation and the neglect of overlap effects
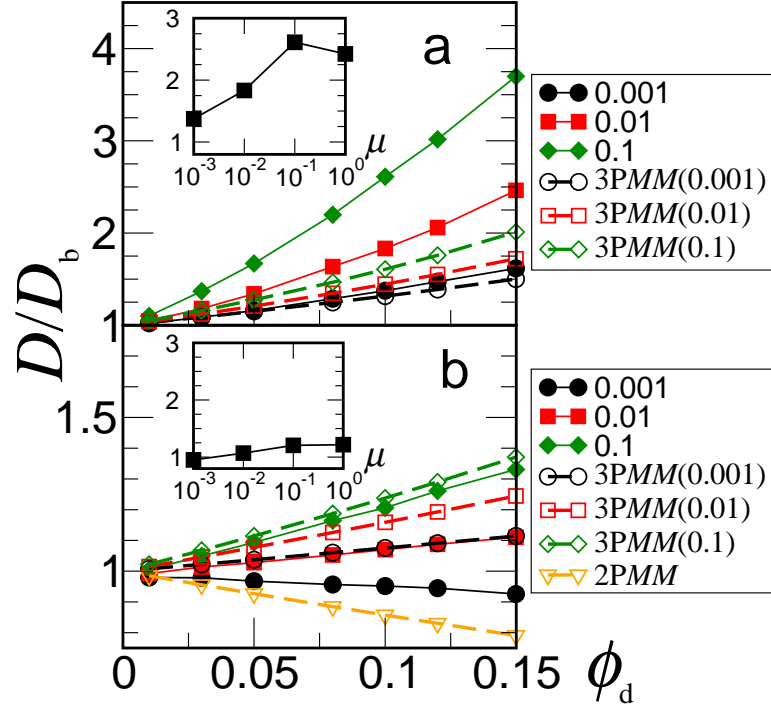
Figure 5.7: Effect of polymer rigidity (μ) on the macroscopic diffusivity of a PNC for (a) $R = 0.1$ and (b) $R = 0.5$. In each plot μ was varied from 0.001 to 0.1 while v_m was fixed at 1.6. The filled symbols represent predictions from our multiscale model and the unfilled symbols show predictions from both two-phase (2P) and three-phase (3P) Maxwell models. The insets display diffusivity data for $\phi_d = 0.1$ at different persistence lengths on a log-scale. All μ values are scaled by the contour length of the polymer.

in the shell models which were discussed earlier. In contrast, for systems which show smaller interfacial layers ($\mu = 0.001$), the 3PMM models tend to capture the results better.

For larger sized particles ($R = 0.5$, Fig. 5.7(b)), we observe an interesting interplay of the obstruction and interfacial effects. For the flexible limit, the interfacial perturbations are reduced and the overall effect of the filler is to act as an obstruction to the penetrant diffusivity. This leads to a lowering of the diffusivity similar to the effects of conventional particle filled membranes. In contrast, for more rigid polymers it is evident that the interfacial effect becomes dominant, leading to an enhancement in the penetrant diffusivities for all filler concentrations. The enhancements in penetrant diffusivity caused by increased polymer rigidity in this larger particle limit is shown in the inset of Fig. 5.7(b), though these enhancements are not as substantial as the case where $R = 0.1$ (inset of Fig. 5.7(a)). These results highlight the subtle, albeit important, role played by the polymer matrix rigidity in influencing the free volume and hence the diffusivity landscapes. Here again the correspondence with the 3PMM follows the general trends noted in the comparisons presented earlier, except that the 3PMM model predictions is found to be less accurate overall for this situation. We believe that this is not necessarily due to any specific feature associated with μ or R values probed, but rather just reflects the fact that the 3PMM tends to overestimate certain effects (such as the strength of the interfacial layer) and underestimate certain effects (such as the range and overlap of the interfacial layers), and hence its quantitative accuracy

depends sensitively on the many parameters which determine the behavior of the macroscopic penetrant diffusivities.

5.4.3   Penetrant size effects

The final effect we probed is that of the size of the penetrant, for which the results are displayed in Fig. 5.8 for $\mu = 0.1$ at two different R values: 0.1 and 1. The results displayed in Fig. 5.8 resembles the experimental observations of reverse selectivity in nanocomposite membranes wherein the diffusivities of larger penetrants are more enhanced compared to the smaller penetrants. The origin of this result (first proposed by Hill[35]) lies in the amplification of the interfacial effects with an increase in the penetrant sizes. We recall that the main role of v_m is in modulating the dependence of the diffusivity in the interfacial layers on the penetrant size. Indeed, in the model we have adopted (Eq. (5.4)), a penetrant with a larger v_m experiences a greater enhancement in its diffusivity in the interfacial regions relative to a penetrant with smaller v_m. Physically, this can be understood as an effect arising from the opening of pathways which were highly restricted to a larger penetrant. In contrast, for a penetrant with smaller v_m, much of these openings were already accessible and hence the effect of lowered polymer densities is much less substantial (a more quantitative way to see this is to consider the derivative dD/dv_m, which can be seen to increase monotonically with v_m). Whence, for smaller penetrants and larger particles (from Fig. 5.8 the case where $v_m = 0.7$ and $R = 1$), the interfacial effects are weak and the particles act more or less as obstacles
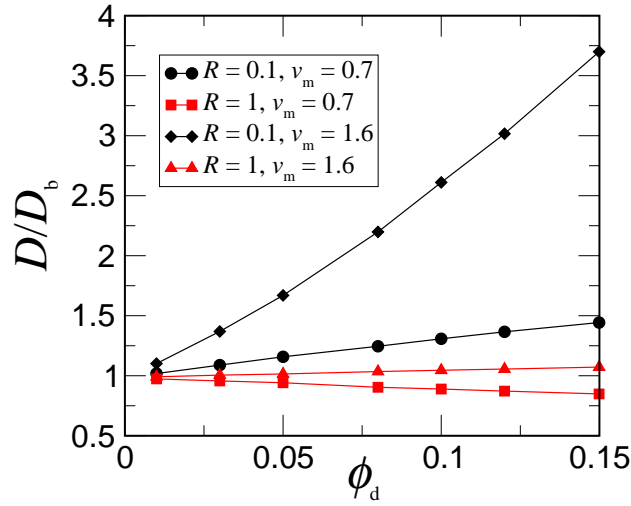
Figure 5.8: Comparing the enhancements of diffusivity upon changing the penetrant's size (measured by v_m) and particle radius (R). v_m was varied from 0.7 to 1.6 and R from 0.1 to 1, while μ was held constant at 0.1.

to the diffusion of penetrants. In contrast, for larger v_m and/or smaller R, the interfacial effects become enhanced and overwhelms the role of particles as obstacles to the penetrant. Interestingly, it is observed from the data for $R = 1$ that for appropriate parameters the same nanofiller composite may act as obstacles to smaller penetrants but may instead promote the diffusivity of larger penetrants (relative to their bulk polymer values). The comparisons to the 3PMM parallels the discussions in the other contexts, and hence we avoid repeating them here.

5.4.4 Comparison to Experiments

One of the main results from our model is that the role of the particle transforms from being an obstacle in the flexible polymer/large particle regime to

a promoter of penetrant movement in the semi-rigid polymer/small particle regime. Such a transition was explicitly shown in work from Merkel et al.[11] where permeability of methane increased in a PMP and fumed silica PNC, whereas propane permeability decreased in a natural rubber and ZnO filler composite.[176] The results of the latter experiments were shown to follow the trend predicted by the 2PMM whereas the former followed trends similar to the ones showed in our model. The other parameters of our study are also comparable to the experimental situation. Explicitly, in Merkel *et al.*[11] the NP was measured to be 13nm, which is approximately an order of magnitude smaller than the typical polymer contour length, thus, making R (relative to the contour length) for these experiments to be possibly near 0.1 (for which our results are shown in Fig. 5.7(a)). The enhancement factor in diffusivity for $\mu = 0.01$ and $R = 0.1$ at $\phi_d = 0.15$ was around 2.5 in our model, which is comparable to the enhancement factor of permeability noted for the fumed silica/PMP PNC at $\phi_d = 0.20$. Therefore, our predictions of our diffusivity enhancements are in the range of results noted in experiments. Moreover, we observe that the reverse selective behavior is also captured in our model as a consequence of the more sensitive dependence of the large penetrant diffusivities to the local polymer densities.

Another effect seen from our results that mimics behavior seen experimentally is the influence of rigidity. Our results demonstrated that as the particle size decreases, the effect of the polymer's rigidity upon diffusion becomes significant enough to enhance the macroscopic diffusivity of the penetrant.

This explanation was also invoked by Merkel et al.[198] who speculated that while flexible polymers may accommodate the volume occupancy of fillers, stiffer polymers may lead to a more substantial disruption of the packing of the polymer's segments. Indeed, in a latter study Merkel et al.[11] used this explanation to rationalize their observations on the particle size dependencies of the enhancements in penetrant diffusivities. The results of our molecular model and the macroscopic penetrant diffusivities are seen to lend support to this hypothesis.

5.4.5 Comparison to Earlier Theoretical Efforts

As noted in the section 5.2, earlier theoretical research by Hill [35, 192] incorporates many of the ingredients we have used in the present effort to model the barrier properties of PNCs. We note that Hill's model also captures many of the experimental observations discussed in the preceding section. Indeed, his results also embody the transformation of the particle from being an obstacle in the large particle regime to a promoter of penetrant movement in the small particle regime. Moreover, since the penetrant diffusivity model we have adopted is identical to that of Hill, the reverse selective behavior is also captured in Hill's model. Finally, we note that Hill demonstrates that the experimental results can be quantitatively fitted by adopting realistic values for parameters in his model.

Owing to the different microscopic polymer model and parameters employed, a quantitative comparison of our results with Hill's model is not possi-

ble. Our research improves upon Hill's work (i) by incorporating a more accurate treatment of the polymer density profiles which accounts for the meltlike nature of the matrix, the rigidity of the polymer chains and the curvature of the dispersed fillers; and (ii) by incorporating a more accurate treatment of the multibody effects arising due to the particle interactions and the overlap of the interfacial layers. The first feature allowed us to explicitly comment on the effect of rigidity, especially its role in influencing the transition from the obstacle to the promoter regimes. These results lend credence to speculations offered by experimentalists (discussed in the preceding section) for explaining the role of rigidity and packing effects. With regards to the second feature, we note that at the low volume fractions probed by experiments, direct multibody effects arising from the particle interactions (MB1) are expected to be less significant. Hence the particle loading dependencies of our diffusivity values can be roughly fitted by a linear or quadratic function similar to the analytical model predictions of Hill. However, as we clearly demonstrated through density profiles and by comparison to the results of 3PMM, effects arising overlap of interfacial layers (absent in Hill's model) do play a significant role in influencing the quantitative details of the results.

Admittedly, the results presented in this chapter improves only the quantitative details of results presented in the earlier model of Hill. However, the methodology we have presented (one of the main objectives of this work) offers the potential to treat complexities not directly addressable by the approximate analytical theories. Explicitly, we note that while our re-

sults were based on a random configuration of the particles created through molecular dynamics simulations, in principle, the methodology was equally applicable to the case where the particle dispersion exhibits structural complexities such as arising from aggregation of the fillers. Also, our numerical methodology is straighforwardly extended to situations involving anisotropic fillers. In contrast, development of continuum composite theories for dispersions of anisotropic fillers proves considerably more difficult relative to their spherical counterparts.[182] Overall, these features highlight the potential of our numerical approach to go beyond the capablities of analytical theories for capturing characteristics representative of experimental situations.

5.5   Conclusion and Future Outlook

In this contribution, a model that included interfacial layer properties in predictions of barrier properties for PNCs and traditional composites was introduced and compared to existing composite theories. The model assembles MD simulations, SCFT based simulations, free volume theory, and a numerical homogenization approach to generate predictions of barrier properties for polymer composites. Our predictions incorporate the influence of polymer rigidity, filler size, penetrant size, and filler volume fraction. By including such effects, we were able to demonstrate that interfacial layers play a significant role upon the macroscopic diffusivity of the penetrant — a result the 2PMM does not capture. Due to the inclusion of continuously varying interfacial layer properties, this predictive model is also able to include the effects of overlapping

interfacial regions, which cannot be accounted for in the 3PMM. Most importantly, the results predicted by our model mirrored trends seen in experimental studies. Overall, our model demonstrates that a combination of highly rigid polymers and/or small NPs are favorable to produce enhancements in diffusivity. Moreover, with the inclusion of penetrant size effects in our model, we were able to see behavior similar to the reverse selective membranes revealed by experiments.

Our approach to predict barrier properties was intended as an illustration of a numerical approach to predict the properties of PNCs. Our approach allows for incorporating more complex structural information about the dispersion, an effect which may prove critical for modeling the properties of PNCs (see Chapter 2). One can also envision extension of our approach to other properties such as conductivity and solubility. For such properties, we note that the local polymer density profiles still serve as a measure of the local properties, and with an appropriate model to quantify such a relationship, many aspects of the present chapter directly carry over to such models.

Chapter 6

On entanglements in polymer nanocomposites

6.1 Introduction

Nanofillers have been shown to have a significant effect on the mechanical properties of polymer nanocomposites (PNC) [23, 45, 43]. It is possible that such effects arise from a change in polymer entanglement length (N_e), a microscopic quantity indicating the number of monomers between entanglement points in the polymer caused by the chain's inability to cross other chains (or, if present, inclusions). The mechanism by which the above occurs is not yet known, though there are viable explanations that have been proposed. One idea is that the polymer can become "stuck" to the surface of the nanofiller which can increase the number of entanglements in the system [43] or even cause bridging of nanofillers [30, 23]. Another idea proposes the nanofiller is an additional "obstacle" that can't be crossed by the polymer, therefore, generating more potential for entanglements [23, 212]. In contrast to these explanations, there is also an idea that a glassy phase around the nanofiller exists

with superior mechanical properties, relative to that of the bulk polymer, that is the cause of this mechanical property enhancement in PNCs [34, 33, 213]

While experimental studies only allow for an indirect description of the topology of the polymer network governing entanglements, simulations can provide direct access to polymer configurations. In fact, computational algorithms have been developed to obtain N_e directly from simulation data [46, 47, 214, 215]. In this chapter, an approach is taken to see if simulations can shed light on how nanofillers influence the entanglements in PNCs. We use a model PNC composed of bead-spring polymers embedded with LJ nanoparticles (of different size), and the polymer-particle interaction between the two is varied from attraction to repulsion for various volume fractions. This model system is chosen since detailed all-atom simulations of a realistic PNC is not pragmatic due to the large length and long time scales inherit of PNCs. Indeed, simplistic models of polymers have shown to accurately explain the critical physics governing such systems [46], and so we leverage this idea here as well.

With our approach, we *first* investigate if the particle-nanoparticle interaction type can influence the entanglement length of the polymer. In this regard, some questions to consider are: If the polymer becomes physically stuck to the surface of the polymer (with an attractive interaction), will the entanglements of the polymer increase as has been suggested others ? If there are no enthalpic effects from the polymer-particle interaction (repulsive interaction), will there be no alteration in entanglement length, which has also been

152

claimed ? *Secondly*, we investigate if increasing the nanoparticle concentration (i.e. increasing confinement) will decrease the entanglement length. If indeed the nanoparticles are creating entanglements by being obstacles for the polymer, then there should be some dependence of N_e on the nanoparticle volume fraction.

Following this introduction, the simulation methods are detailed in Sec. 6.2. After this, the results are presented with a discussion in Sec. 6.3. Finally, a conclusion and future outlook is given in Sec 6.4.

6.2   Simulation Methods

The model PNC used in our simulations was comprised of a bead-spring polymer interacting with an LJ particle of a different size than the monomers. The bead-spring polymer was composed of monomers interacting with other monomers via an LJ interaction,

$$U_{LJ}(r) = 4\epsilon \left[\left(\frac{\sigma}{r - \Delta} \right)^{12} - \left(\frac{\sigma}{r - \Delta} \right)^{6} \right], \quad for \quad r \leq \Delta + R_c, \qquad (6.1)$$

where ϵ, σ, and the monomer mass (m) were set to unity, $R_c = 1.12$, Δ was set to zero, $U_{LJ}(r)$ was shifted so that it is zero at $r = \Delta + R_c$, and $U_{LJ}(r)$ is zero at $r > \Delta + R_c$. All units of measure are relative to ϵ, σ, and m of the monomer. The monomers were held together via a FENE potential of the form,

$$U_b(r) = -\frac{KR_o^2}{2} \ln \left[1 - \left(\frac{r}{R_o} \right)^2 \right], \qquad (6.2)$$

where $K = 30$ and $R_o = 1.5$. The monomer-particle interaction also had the form of Eq. 6.1, with $\sigma_{mp} = 1$, $\epsilon_{mp} = 2$, and $\Delta_{mp} = 1.5$. For the attractive interaction $R_{c,mp} = 2.5$ while for the repulsive interaction the cutoff was $R_{c,mp} = 1.12$. This potential was used to account for the differences in size of the particle and monomer. The particles themselves do not see one another, were randomly dispersed in the simulation box, and were fixed. Each simulation were composed of 250 chains each having a length of $N = 200$ monomers. The volume fractions investigated were 0.1%, 5%, and 10%, with their simulations having 2, 100, and 200 nanoparticles, respectively.

To obtain equilibrium configurations of the PNC, a few steps were taken. First, a pure bead-spring melt was simulated with a Langevin thermostat at a number density (ρ) of 0.85 and temperature (T) of unity, and allowed to equilibrate over a time of $t = 492,000$. The pressure was averaged over a production run of $t = 120,000$ and was calculated to be 4.92. Following this run, an NPT ensemble was used to drive the pressure of each PNC simulation run from $P = 0.3$ to the average pressure obtained from the pure melt simulations over a simulation time of $t = 6,000$. Afterwards, from a simulation run of $t = 6,000$, a configuration is chosen with the closest pressure to the pressure observed in the melt simulation for the start of an NVT simulation with a Langevin thermostat. The time allowed for each PNC to equilibrate was $t = 492,000$, which was long enough for the center of mass of the polymers to move on average many times the size of the polymer. Configurations following this step were then used in the primitive path analysis.

Previous work by Sukumaran et al.[47, 46] on a primitive path analysis (PPA) for the calculation of polymer entanglement length is utilized here. Whereas in the aforementioned study this method was implemented for pure polymer scenarios, here it is used for polymer-particle melt mixtures. A brief explanation of this method is provided here, but we refer the reader to Ref [47] for further details. For each equilibrated configuration obtained from the above described process, the ends of the polymer chains are fixed and the intrachain repulsive LJ interactions removed, while the interchain repulsive LJ interactions between monomers are retained. The temperature is then slowly reduced to nearly zero to allow for the polymer to assume the "primitive path". (Note, the parameters used for this method can be found in Ref [47]) To allow this procedure to work for a PNC, we just removed the attractive tail (if any existed) between the particle-monomer interaction and kept the particles fixed in the simulation. Since the entangled configurations are expected to develop during the equilibration portion of the simulation, the contribution to the entanglement length from the attractive tail during the PPA is assumed here to be negligible. Finally, PPA was performed separately on 100 equilibrium snapshots, providing an average of N_e to be calculated.

6.3   Results and Discussion

To ensure the PPA was being correctly implemented, a pure polymer system was used to determine the entanglement length (N_e), which turned out to be $N_{e,b} = 63 \pm 2$. This is commensurate with what was obtained by Sukumaran

et al. [46] Not only did we want to see how the particle-monomer interaction affected $N_{e,c}$ (the entanglement length for the PNC), but we also investigated how nanoparticle volume fraction (ϕ) played a role on entanglements. To elucidate how ϕ increased the confinement in the system we calculated the average interparticle distance h_p as

$$h_p = 2R_p \left[\left(\frac{0.7}{\phi} \right)^{\frac{1}{3}} - 1 \right], \tag{6.3}$$

where $R_p = \Delta_{mp} + \sigma_{mp}/2$ is the particle's radius and ϕ is the volume fraction of particles; here $R_p = 2$. This interparticle distance was rescaled by an estimate of the distance between entanglements in the pure polymer: $b_e = \sqrt{N_{e,b}R_b^2/N}$, where R_b^2 is the polymer chain's end-to-end distance from the pure polymer simulation.

The entanglement length results for different volume fractions of nanoparticles are shown in Table 6.1. The second column provides the ratio h_p/b_e corresponding to each ϕ as a measure of confinement in the composite, whereas the third and fourth columns provide N_e for an attractive and repulsive monomer-particle interaction, respectively. Our approach was not able to see any entanglement difference for the attractive case. This could be attributed to a possible weak attractive interaction between the monomers and particles. The repulsive case also showed little change in N_e. This result, however, is commensurate with the results discovered by Mackay et al.[45], which also had a ratio $R_p/R_g = 0.3$ (where R_g is the radius of gyration) as we did in our simulations.

ϕ	h_p/b_e	N_e	
		Attractive	Repulsive
0.001	2.18	64 ± 3	60 ± 3
0.05	0.39	63 ± 2	63 ± 3
0.10	0.25	64 ± 2	63 ± 3

Table 6.1: Entanglement predictions for both attractive and repulsive monomer-particle interactions.

To check if the parameters chosen for the attractive/repulsive polymer-nanoparticle interactions actually promoted wetting/dewetting of the polymer, we decided to measure the adsorption characteristics of the polymer. This was done by studying a very similar system, but with one fixed particle in a polymer melt with smaller chain length (500 chains with $N = 20$); this was done to reduce the computational time to accomplish the simulations. A smaller chain length is also reasonable since we do not expect he polymer's molecular weight to significantly influence the adsorption characteristics of the system. The particle-monomer (attractive/repulsive) interaction and polymer-polymer interactions were all kept the same, as well as the pressure and temperature of the system. To measure adsorption, the surface excess[41, 216, 217, 130] was calculated by

$$\Gamma_s = \frac{1}{R_p^2} \int_{R_p}^{\infty} \left(g_{pm}(r) - 1 \right) r^2 \, dr, \tag{6.4}$$

where $g_{pm}(r)$ is the radial distribution function between the particle and monomers. When $\Gamma_s > 0$ this indicates wetting and when $\Gamma_s < 0$ this indicates dewetting. Performing this calculation for both the attractive and repulsive cases, we obtain $\Gamma_s(attractive) = 0.0076$ and $\Gamma_s(repulsive) = -0.0976$. This

measurement clearly indicates the polymer-nanoparticle interaction is creating the effect we intended between the polymer and nanoparticle. However, comparing the order of magnitude of Γ_s between interactions types suggests that the attraction may not have been strong enough.

What is more surprising in Table 6.1 is the lack of confinement effects on N_e, even for $h_p/b_e = 0.25$. To draw more concrete explanations from this set of results, more parameters for particle size, polymer-nanoparticle interaction, and nanoparticle volume fraction must be performed to see their effects on N_e. We speculate the nanoparticles were perhaps too small in size to induce any significant confinement and, perhaps, acted more like a solution than a filler. The nanoparticle size may also explain the lack of effect from the polymer-nanoparticle interaction, as the interfacial area per nanoparticle was too small to generate a significant contribution of polymer attachments to the nanoparticle surface. We reiterate that the above explanations are only *speculative*, and that a more thorough investigation of the parameters in the PNC system would need to be explored in order to support such claims.

6.4   Conclusions and Outlook

In this chapter, we utilize MD simulations of a model PNC composed of bead-spring polymers and LJ nanoparticles to assess the latter's effect on the polymer melt's entanglement length. The polymer-nanoparticle interaction was varied between attraction and repulsion and the nanoparticle's volume fraction was varied to induce confinement in the system. It was found that

158

neither the polymer-nanoparticle interaction or nanoparticle volume fraction affect the entanglement length of the polymer melt for the parameters in this study. However, to draw more conclusive statements, a more extensive parameter set must be evaluated for nanoparticle size and volume fraction as well as polymer-nanoparticle interaction. Results elucidating the adsorption of the polymer onto the nanoparticle surface suggests that perhaps the polymer wetting was not strong enough to influence entanglements. Again, this is speculative as a more detailed study of attraction strength should be performed before claiming the above statement.

Chapter 7

Future Work

While this research utilized a simplistic model of a PNC to develop the methods to predict structure and properties in PNCs, a more thorough investigation of their applicability to realistic PNC systems is required. For instance, utilizing the coarse-graining method on a realistic PNC to predict its mesoscale structure and, then, utilize this structure as input in our numerical approach to calculate the PNC's barrier properties, ultimately comparing these results to experimental measurements. In addition, rheological property predictions of an actual PNC can be directly compared to experimental measurements. Such studies would clarify the accuracy of our approach and whether additional features to our coarse-graining method and/or numerical approach are required. A potential obstacle may be that in a more realistic representation of a PNC, additional detailed intramolecular interactions may be required; for instance, angle and torsional interactions may be necessary to produce the same accuracy we see in our coarse-graining method. Also, the extension of our numerical approach to predict properties such as solubility and conductivity would help reveal if our approach is applicable for more than just penetrant diffusion. Another effort in this regard is to develop relationships between local

structure and local properties so that interfacial layer properties can be taken into account when calculating macroscopic properties. More generally, the ideas derived from our coarse-graining method may provide a means to incorporate many-body interactions in the simulation of other particle containing complex fluids where a coarse-grained representation of the permeating fluid may be used as a means to correct the potential of mean-forces deduced in the dilute limit.

Bibliography

[1] Y. Fukushima and S. Inagaki. Synthesis of an intercalated compound of montmorillonite and 6-polyamide. *Journal of Inclusion Phenomena*, 5 (4):473–482, August 1987.

[2] A. Okada and A. Usuki. The chemistry of polymer-clay hybrids. *Materials Science & Engineering C-biomimetic Materials Sensors and Systems*, 3(2):109–115, November 1995.

[3] M. Biswas and S. S. Ray. Recent progress in synthesis and evaluation of polymer-montmorillonite nanocomposites. *New Polymerization Techniques and Synthetic Methodologies*, 155:167–221, 2001.

[4] J. H. Koo, L. A. Pilato, and G. E. Wissler. Polymer nanostructured materials for propulsion systems. *Journal of Spacecraft and Rockets*, 44 (6):1250–1262, November 2007.

[5] P. C. LeBaron, Z. Wang, and T. J. Pinnavaia. Polymer-layered silicate nanocomposites: an overview. *Applied Clay Science*, 15(1-2):11–29, September 1999.

[6] E. P. Giannelis, R. Krishnamoorti, and E. Manias. Polymer-silicate nanocomposites: Model systems for confined polymers and polymer brushes. *Polymers In Confined Environments*, 138:107–147, 1999.

[7] Q. H. Zeng, A. B. Yu, G. Q. Lu, and D. R. Paul. Clay-based polymer nanocomposites: Research and commercial development. *Journal of Nanoscience and Nanotechnology*, 5(10):1574–1592, October 2005.

[8] F. M. Du, R. C. Scogna, W. Zhou, S. Brand, J. E. Fischer, and K. I. Winey. Nanotube networks in polymer nanocomposites: Rheology and

electrical conductivity. *Macromolecules*, 37(24):9048–9055, November 2004.

[9] T. Ramanathan, S. Stankovich, D. A. Dikin, H. Liu, H. Shen, S. T. Nguyen, and L. C. Brinson. Graphitic nanofillers in pmma nanocomposites - an investigation of particle size influence on nanocomposite and dispersion and their properties. *Journal of Polymer Science Part B-polymer Physics*, 45(15):2097–2112, August 2007.

[10] E. P. Giannelis. Polymer-layered silicate nanocomposites: Synthesis, properties and applications. *Applied Organometallic Chemistry*, 12(10-11):675–680, October 1998.

[11] T. C. Merkel, B. D. Freeman, R. J. Spontak, Z. He, I. Pinnau, P. Meakin, and A. J. Hill. Ultrapermeable, reverse-selective nanocomposite membranes. *Science*, 296(5567):519–522, April 2002.

[12] P. B. Messersmith and E. P. Giannelis. Synthesis and barrier properties of poly(epsilon-caprolactone)-layered silicate nanocomposites. *Journal of Polymer Science Part A-polymer Chemistry*, 33(7):1047–1057, May 1995.

[13] R. J. Xu, E. Manias, A. J. Snyder, and J. Runt. New biomedical poly(urethane urea) - layered silicate nanocomposites. *Macromolecules*, 34(2):337–339, January 2001.

[14] K. Yano, A. Usuki, A. Okada, T. Kurauchi, and O. Kamigaito. Synthesis and properties of polyimide clay hybrid. *Journal of Polymer Science Part A-polymer Chemistry*, 31(10):2493–2498, September 1993.

[15] K. I. Winey and R. A. Vaia. Polymer nanocomposites. *MRS Bulletin*, 32(4):314–319, April 2007.

[16] J. M. Kropka, K. W. Putz, V. Pryamitsyn, V. Ganesan, and P. F. Green.

Origin of dynamical properties in pmma-c-60 nanocomposites. *Macromolecules*, 40(15):5424–5432, July 2007.

[17] T. D. Fornes, D. L. Hunter, and D. R. Paul. Nylon-6 nanocomposites from alkylammonium-modified clay: The role of alkyl tails on exfoliation. *Macromolecules*, 37(5):1793–1798, March 2004.

[18] M. Abdalla, D. Dean, D. Adibempe, E. Nyairo, P. Robinson, and G. Thompson. The effect of interfacial chemistry on molecular mobility and morphology of multiwalled carbon nanotubes epoxy nanocomposite. *Polymer*, 48(19):5662–5670, September 2007.

[19] J. Carretero-Gonzalez, H. Retsos, E. P. Giannelis, T. A. Ezquerra, M. Hernandez, and M. A. Lopez-Manchado. Miscibility-dispersion, interfacial strength and nanoclay mobility relationships in polymer nanocomposites. *Soft Matter*, 5(18):3481–3486, 2009.

[20] S. S. Ray, K. Okamoto, and M. Okamoto. Structure-property relationship in biodegradable poly(butylene succinate)/layered silicate nanocomposites. *Macromolecules*, 36(7):2355–2367, April 2003.

[21] M. Abdalla, D. Dean, M. Theodore, J. Fielding, E. Nyairo, and G. Price. Magnetically processed carbon nanotube/epoxy nanocomposites: Morphology, thermal, and mechanical properties. *Polymer*, 51(7):1614–1620, March 2010.

[22] T. Kimura, H. Ago, M. Tobita, S. Ohshima, M. Kyotani, and M. Yumura. Polymer composites of carbon nanotubes aligned by a magnetic field. *Advanced Materials*, 14(19):1380–1383, October 2002.

[23] Q. Zhang and L. A. Archer. Poly(ethylene oxide)/silica nanocomposites: Structure and rheology. *Langmuir*, 18(26):10435–10442, December 2002.

[24] J. B. Hooper and K. S. Schweizer. Theory of phase separation in polymer nanocomposites. *Macromolecules*, 39(15):5133–5142, July 2006.

164

[25] Y. L. Chen, K. S. Schweizer, and M. Fuchs. Phase separation in suspensions of colloids, polymers and nanoparticles: Role of solvent quality, physical mesh, and nonlocal entropic repulsion. *Journal of Chemical Physics*, 118(8):3880–3890, February 2003.

[26] L. M. Hall and K. S. Schweizer. Many body effects on the phase separation and structure of dense polymer-particle melts. *Journal of Chemical Physics*, 128(23):234901, June 2008.

[27] J. Huh, V. V. Ginzburg, and A. C. Balazs. Thermodynamic behavior of particle/diblock copolymer mixtures: Simulation and theory. *Macromolecules*, 33(21):8085–8096, October 2000.

[28] R. B. Thompson, V. V. Ginzburg, M. W. Matsen, and A. C. Balazs. Predicting the mesophases of copolymer-nanoparticle composites. *Science*, 292(5526):2469–2472, June 2001.

[29] M. Surve, V. Pryamitsyn, and V. Ganesan. Nanoparticles in solutions of adsorbing polymers: Pair interactions, percolation, and phase behavior. *Langmuir*, 22(3):969–981, January 2006.

[30] M. Surve, V. Pryamitsyn, and V. Ganesan. Polymer-bridged gels of nanoparticles in solutions of adsorbing polymers. *Journal of Chemical Physics*, 125(6):064903, August 2006.

[31] S. W. Sides, B. J. Kim, E. J. Kramer, and G. H. Fredrickson. Hybrid particle-field simulations of polymer nanocomposites. *Physical Review Letters*, 96(25):250601, June 2006.

[32] F. W. Starr, J. F. Douglas, and S. C. Glotzer. Origin of particle clustering in a simulated polymer nanocomposite and its impact on rheology. *Journal of Chemical Physics*, 119(3):1777–1788, July 2003.

[33] J. Berriot, H. Montes, F. Lequeux, D. Long, and P. Sotta. Evidence

165

for the shift of the glass transition near the particles in silica-filled elastomers. *Macromolecules*, 35(26):9756–9762, December 2002.

[34] W.-D. Hergeth, U.-J. Steinau, H.-J. Bittrich, G. Simon, and K. Schmutzler. Polymerization in the presence of seeds. part iv: Emulsion polymers containing inorganic filler particles. *Polymer*, 30(2):254 – 258, 1989. ISSN 0032-3861. doi: DOI: 10.1016/0032-3861(89)90114-6. URL `http://www.sciencedirect.com/science/article/B6TXW-48CPBNW-C/2/6ad2f8b8c8afa`

[35] R. J. Hill. Reverse-selective diffusion in nanocomposite membranes. *Physical Review Letters*, 96(21):216001, June 2006.

[36] G. M. Odegard, T. C. Clancy, and T. S. Gates. Modeling of the mechanical properties of nanoparticle/polymer composites. *Polymer*, 46(2): 553–562, January 2005.

[37] E. Hackett, E. Manias, and E. P. Giannelis. Computer simulation studies of peo/layer silicate nanocomposites. *Chemistry of Materials*, 12(8): 2161–2167, August 2000.

[38] M. Vacatello. Monte carlo simulations of polymer melts filled with solid nanoparticles. *Macromolecules*, 34(6):1946–1952, March 2001.

[39] J. B. Hooper, K. S. Schweizer, T. G. Desai, R. Koshy, and P. Keblinski. Structure, surface excess and effective interactions in polymer nanocomposite melts and concentrated solutions. *Journal of Chemical Physics*, 121(14):6986–6997, October 2004.

[40] K. C. Daoulas, D. N. Theodorou, V. A. Harmandaris, N. C. Karayiannis, and V. G. Mavrantzas. Self-consistent-field study of compressible semiflexible melts adsorbed on a solid substrate and comparison with atomistic simulations. *Macromolecules*, 38(16):7134–7149, August 2005.

[41] A. A. Louis, P. G. Bolhuis, E. J. Meijer, and J. P. Hansen. Polymer

induced depletion potentials in polymer-colloid mixtures. *Journal of Chemical Physics*, 117(4):1893–1907, July 2002.

[42] O. Borodin, D. Bedrov, G. D. Smith, J. Nairn, and S. Bardenhagen. Multiscale modeling of viscoelastic properties of polymer nanocomposites. *Journal of Polymer Science Part B-polymer Physics*, 43(8):1005–1013, April 2005.

[43] S. S. Sternstein and A. J. Zhu. Reinforcement mechanism of nanofilled polymer melts as elucidated by nonlinear viscoelastic behavior. *Macromolecules*, 35(19):7262–7273, September 2002.

[44] B. J. Anderson and C. F. Zukoski. Rheology and microstructure of entangled polymer nanocomposite melts. *Macromolecules*, 42(21):8370–8384, November 2009.

[45] M. E. Mackay, T. T. Dao, A. Tuteja, D. L. Ho, B. Van Horn, H. C. Kim, and C. J. Hawker. Nanoscale effects leading to non-einstein-like decrease in viscosity. *Nature Materials*, 2(11):762–766, November 2003.

[46] R. Everaers, S. K. Sukumaran, G. S. Grest, C. Svaneborg, A. Sivasubramanian, and K. Kremer. Rheology and microscopic topology of entangled polymeric liquids. *Science*, 303(5659):823–826, February 2004.

[47] S. K. Sukumaran, G. S. Grest, K. Kremer, and R. Everaers. Identifying the primitive path mesh in entangled polymer liquids. *Journal of Polymer Science Part B-polymer Physics*, 43(8):917–933, April 2005.

[48] S. C. Tjong. Structural and mechanical properties of polymer nanocomposites. *Materials Science & Engineering R-Reports*, 53(3-4):73–197, August 2006.

[49] V. Ganesan. Some issues in polymer nanocomposites: Theoretical and modeling opportunities for polymer physics. *Journal of Polymer Science Part B-Polymer Physics*, 46(24):2666–2671, December 2008.

167

[50] V. Ganesan, C. J. Ellison, and V. Pryamitsyn. Mean-field models of structure and dispersion of polymer-nanoparticle mixtures. *Soft Matter*, DOI: 10.1039/b926992d, 2010. doi: 10.1039/b926992d.

[51] J. P. Hansen and I. R. McDonald. *Theory of Simple Liquids*. New York , NY: Academic Press, 1986.

[52] J. G. Curro, K. S. Schweizer, G. S. Grest, and K. Kremer. A comparison between integral-equation theory and molecular-dynamics simulations of dense, flexible polymer liquids. *Journal of Chemical Physics*, 91(2): 1357–1364, July 1989.

[53] K. G. Honnell, J. G. Curro, and K. S. Schweizer. Local-structure of semi-flexible polymer melts. *Macromolecules*, 23(14):3496–3505, July 1990.

[54] K. S. Schweizer and J. G. Curro. Integral equation theories of the structure, thermodynamics, and phase transitions of polymer fluids. *Advances In Chemical Physics, Vol 98*, 98:1–142, 1997.

[55] A. Yethiraj. Polymer melts at solid surfaces. *Advances In Chemical Physics, Volume 121*, 121:89–139, 2002.

[56] J. B. Hooper and K. S. Schweizer. Contact aggregation, bridging, and steric stabilization in dense polymer-particle mixtures. *Macromolecules*, 38(21):8858–8869, October 2005.

[57] A. Jayaraman and K. S. Schweizer. Effective interactions, structure, and phase behavior of lightly tethered nanoparticles in polymer melts. *Macromolecules*, 41(23):9430–9438, December 2008.

[58] J. B. Hooper and K. S. Schweizer. Real space structure and scattering patterns of model polymer nanocomposites. *Macromolecules*, 40(19): 6998–7008, September 2007.

[59] J. B. Hooper, J. D. McCoy, and J. G. Curro. Density functional theory of simple polymers in a slit pore. i. theory and efficient algorithm. *Journal of Chemical Physics*, 112(6):3090–3093, February 2000.

[60] A. Yethiraj and C. E. Woodward. Monte-carlo density-functional theory of nonuniform polymer melts. *Journal of Chemical Physics*, 102(13): 5499–5505, April 1995.

[61] N. Patel and S. A. Egorov. Interactions between nanocolloidal particles in polymer solutions: Effect of attractive interactions. *Journal of Chemical Physics*, 123(14):144916, October 2005.

[62] R. A. Vaia and E. P. Giannelis. Lattice model of polymer melt intercalation in organically-modified layered silicates. *Macromolecules*, 30(25): 7990–7999, December 1997.

[63] R. A. Vaia and E. P. Giannelis. Polymer melt intercalation in organically-modified layered silicates: Model predictions and experiment. *Macromolecules*, 30(25):8000–8009, December 1997.

[64] V. V. Ginzburg, C. Singh, and A. C. Balazs. Theoretical phase diagrams of polymer/clay composites: The role of grafted organic modifiers. *Macromolecules*, 33(3):1089–1099, February 2000.

[65] M. Surve, V. Pryamitsyn, and V. Ganesan. Dispersion and percolation transitions of nanorods in polymer solutions. *Macromolecules*, 40(2): 344–354, January 2007.

[66] M. Surve, V. Pryamitsyn, and V. Ganesan. Universality in structure and elasticity of polymer-nanoparticle gels. *Physical Review Letters*, 96 (17):177805, May 2006.

[67] J. Baschnagel, K. Binder, P. Doruker, A. A. Gusev, O. Hahn, K. Kremer, W. L. Mattice, F. Muller-Plathe, M. Murat, W. Paul, S. Santos, U. W. Suter, and V. Tries. Bridging the gap between atomistic and

coarse-grained models of polymers: Status and perspectives. *Advances In Polymer Science: Viscoelasticity, Atomistic Models, Statistical Chemistry*, 152:41–156, 2000.

[68] F. Muller-Plathe. Coarse-graining in polymer simulation: From the atomistic to the mesoscopic scale and back. *Chemphyschem*, 3(9):754–769, September 2002.

[69] F. W. Starr, T. B. Schroder, and S. C. Glotzer. Effects of a nanoscopic filler on the structure and dynamics of a simulated polymer melt and the relationship to ultrathin films. *Physical Review E*, 64(2):021802, August 2001.

[70] Q. H. Zeng, A. B. Yu, G. Q. Lu, and R. K. Standish. Molecular dynamics simulation of the structural and dynamic properties of dioctade-cyldimethyl ammoniums in organoclays (vol 108b, pg 10031, 2004). *Journal of Physical Chemistry B*, 109(5):2034–2034, February 2005.

[71] H. P. He, J. Galy, and J. F. Gerard. Molecular simulation of the interlayer structure and the mobility of alkyl chains in hdtma(+)/montmorillonite hybrids. *Journal of Physical Chemistry B*, 109(27):13301–13306, July 2005.

[72] R. C. Picu and A. Rakshit. Dynamics of free chains in polymer nanocomposites. *Journal of Chemical Physics*, 126(14):144909, April 2007.

[73] H. S. Ashbaugh, H. A. Patel, S. K. Kumar, and S. Garde. Mesoscale model of polymer melt structure: Self-consistent mapping of molecular correlations to coarse-grained potentials. *Journal of Chemical Physics*, 122(10):104908, March 2005.

[74] D. Reith, M. Putz, and F. Muller-Plathe. Deriving effective mesoscale potentials from atomistic simulations. *Journal of Computational Chemistry*, 24(13):1624–1636, October 2003.

[75] S. Izvekov and G. A. Voth. Multiscale coarse graining of liquid-state systems. *Journal of Chemical Physics*, 123(13):134105, October 2005.

[76] S. Izvekov and G. A. Voth. A multiscale coarse-graining method for biomolecular systems. *Journal of Physical Chemistry B*, 109(7):2469–2473, February 2005.

[77] M. Praprotnik, L. Delle Site, and K. Kremer. Multiscale simulation of soft matter: From scale bridging to adaptive resolution. *Annual Review of Physical Chemistry*, 59:545–571, 2008.

[78] A. P. Lyubartsev and A. Laaksonen. Calculation of effective interaction potentials from radial-distribution functions - a reverse monte-carlo approach. *Physical Review E*, 52(4):3730–3737, October 1995.

[79] S. J. Marrink, A. H. de Vries, and A. E. Mark. Coarse grained model for semiquantitative lipid simulations. *Journal of Physical Chemistry B*, 108(2):750–760, January 2004.

[80] S. J. Marrink, H. J. Risselada, S. Yefimov, D. P. Tieleman, and A. H. de Vries. The martini force field: Coarse grained model for biomolecular simulations. *Journal of Physical Chemistry B*, 111(27):7812–7824, July 2007.

[81] L. Monticelli, S. K. Kandasamy, X. Periole, R. G. Larson, D. P. Tieleman, and S. J. Marrink. The martini coarse-grained force field: Extension to proteins. *Journal of Chemical Theory and Computation*, 4(5): 819–834, May 2008.

[82] S. Izvekov, M. Parrinello, C. J. Burnham, and G. A. Voth. Effective force fields for condensed phase systems from ab initio molecular dynamics simulation: A new method for force-matching. *Journal of Chemical Physics*, 120(23):10896–10913, June 2004.

[83] F. Ercolessi and J. Adams. Interatomic potentials from 1st-principles calculations - the force-matching method. *Europhysics Letters*, 26(8): 583–588, June 1994.

[84] A. K. Soper. Empirical potential monte carlo simulation of fluid structure. *Chemical Physics*, 202(2-3):295–306, January 1996.

[85] T. Headgordon and F. H. Stillinger. An orientational perturbation-theory for pure liquid water. *Journal of Chemical Physics*, 98(4):3313–3327, February 1993.

[86] P. G. Bolhuis, A. A. Louis, J. P. Hansen, and E. J. Meijer. Accurate effective pair potentials for polymer solutions. *Journal of Chemical Physics*, 114(9):4296–4311, March 2001.

[87] G. Milano and F. Muller-Plathe. Mapping atomistic simulations to meso-scopic models: A systematic coarse-graining procedure for vinyl polymer chains. *Journal of Physical Chemistry B*, 109(39):18609–18619, October 2005.

[88] T. Spyriouni, C. Tzoumanekas, D. Theodorou, F. Muller-Plathe, and G. Milano. Coarse-grained and reverse-mapped united-atom simulations of long-chain atactic polystyrene melts: Structure, thermodynamic properties, chain conformation, and entanglements. *Macromolecules*, 40(10): 3876–3885, May 2007.

[89] H. Fukunaga, J. Takimoto, and M. Doi. A coarse-graining procedure for flexible polymer chains with bonded and nonbonded interactions. *Journal of Chemical Physics*, 116(18):8183–8190, May 2002.

[90] D. Fritz, V. A. Harmandaris, K. Kremer, and N. F. A. van der Vegt. Coarse-grained polymer melts based on isolated atomistic chains: Simulation of polystyrene of different tacticities. *Macromolecules*, 42(19): 7579–7588, October 2009.

[91] C. Peter, L. Delle Site, and K. Kremer. Classical simulations from the atomistic to the mesoscale and back: coarse graining an azobenzene liquid crystal. *Soft Matter*, 4(4):859–869, 2008.

[92] V. A. Harmandaris, D. Reith, N. F. A. Van der Vegt, and K. Kremer. Comparison between coarse-graining models for polymer systems: Two mapping schemes for polystyrene. *Macromolecular Chemistry and Physics*, 208(19-20):2109–2120, October 2007.

[93] V. A. Harmandaris, N. P. Adhikari, N. F. A. van der Vegt, and K. Kremer. Hierarchical modeling of polystyrene: From atomistic to coarse-grained simulations. *Macromolecules*, 39(19):6708–6719, September 2006.

[94] M. Murat and K. Kremer. From many monomers to many polymers: Soft ellipsoid model for polymer melts and mixtures. *Journal of Chemical Physics*, 108(10):4340–4348, March 1998.

[95] W. Tschop, K. Kremer, J. Batoulis, T. Burger, and O. Hahn. Simulation of polymer melts. i. coarse-graining procedure for polycarbonates. *Acta Polymerica*, 49(2-3):61–74, February 1998.

[96] S. Izvekov and G. A. Voth. Solvent-free lipid bilayer model using multiscale coarse-graining. *Journal of Physical Chemistry B*, 113(13):4443–4455, April 2009.

[97] A. P. Lyubartsev. Multiscale modeling of lipids and lipid bilayers. *European Biophysics Journal With Biophysics Letters*, 35(1):53–61, December 2005.

[98] T. Murtola, M. Karttunen, and I. Vattulainen. Systematic coarse graining from structure using internal states: Application to phospholipid/cholesterol bilayer. *Journal of Chemical Physics*, 131(5):055101, August 2009.

[99] D. Bedrov, G. D. Smith, and J. S. Smith. Matrix-induced nanoparticle interactions in a polymer melt: A molecular dynamics simulation study. *Journal of Chemical Physics*, 119(19):10438–10447, November 2003.

[100] J. S. Smith, D. Bedrov, and G. D. Smith. A molecular dynamics simulation study of nanoparticle interactions in a model polymer-nanoparticle composite. *Composites Science and Technology*, 63(11):1599–1605, August 2003.

[101] M. Dijkstra, R. van Roij, R. Roth, and A. Fortini. Effect of many-body interactions on the bulk and interfacial phase behavior of a model colloid-polymer mixture. *Physical Review E*, 73(4):041404, April 2006.

[102] M. Dijkstra, J. M. Brader, and R. Evans. Phase behaviour and structure of model colloid-polymer mixtures. *Journal of Physics-condensed Matter*, 11(50):10079–10106, December 1999.

[103] K. Kremer and G. S. Grest. Dynamics of entangled linear polymer melts - a molecular-dynamics simulation. *Journal of Chemical Physics*, 92(8): 5057–5086, April 1990.

[104] S. Plimpton. Fast parallel algorithms for short-range molecular-dynamics. *Journal of Computational Physics*, 117(1):1–19, March 1995.

[105] URL `lammps.sandia.gov`.

[106] J. P. Hansen, C. I. Addison, and A. A. Louis. Polymer solutions: from hard monomers to soft polymers. *Journal of Physics-condensed Matter*, 17(45):S3185–S3193, November 2005.

[107] A. A. Louis, P. G. Bolhuis, E. J. Meijer, and J. P. Hansen. Density profiles and surface tension of polymers near colloidal surfaces. *Journal of Chemical Physics*, 116(23):10547–10556, June 2002.

[108] P. G. Bolhuis, E. J. Meijer, and A. A. Louis. Colloid-polymer mixtures in the protein limit. *Physical Review Letters*, 90(6):068304, February 2003.

[109] A. Fortini, P. G. Bolhuis, and M. Dijkstra. Effect of excluded volume interactions on the interfacial properties of colloid-polymer mixtures. *Journal of Chemical Physics*, 128(2):024904, January 2008.

[110] P. G. Bolhuis and A. A. Louis. How to derive and parameterize effective potentials in colloid-polymer mixtures. *Macromolecules*, 35(5): 1860–1869, February 2002.

[111] P. G. Bolhuis, A. A. Louis, and J. P. Hansen. Influence of polymer-excluded volume on the phase-behavior of colloid-polymer mixtures. *Physical Review Letters*, 89(12):128302, September 2002.

[112] A. A. Louis, P. G. Bolhuis, R. Finken, V. Krakoviack, E. J. Meijer, and J. P. Hansen. Coarse-graining polymers as soft colloids. *Physica A-statistical Mechanics and Its Applications*, 306(1-4):251–261, April 2002.

[113] A. A. Louis. No free lunch for effective potentials: general comment for faraday fd144. *Faraday Discuss.*, 144:323, 2010.

[114] A. A. Louis. Beware of density dependent pair potentials. *Journal of Physics-condensed Matter*, 14(40):9187–9206, October 2002.

[115] P. Carbone, H. A. K. Varzaneh, X. Y. Chen, and F. Muller-Plathe. Transferability of coarse-grained force fields: The polymer case. *Journal of Chemical Physics*, 128(6):064904, February 2008.

[116] V. Krishna, W. G. Noid, and G. A. Voth. The multiscale coarse-graining method. iv. transferring coarse-grained potentials between temperatures. *The Journal of Chemical Physics*, 131(2):024103, 2009. doi: 10.1063/1.3167797.

[117] J. W. Mullinax and W. G. Noid. Extended ensemble approach for deriving transferable coarse-grained potentials. *Journal of Chemical Physics*, 131(10):104110, September 2009.

[118] E. C. Allen and G. C. Rutledge. Evaluating the transferability of coarse-grained, density-dependent implicit solvent models to mixtures and chains. *Journal of Chemical Physics*, 130(3):034904, January 2009.

[119] M. E. Tuckerman, C. J. Mundy, S. Balasubramanian, and M. L. Klein. Modified nonequilibrium molecular dynamics for fluid flows with energy conservation. *The Journal of Chemical Physics*, 106(13):5615–5621, 1997. doi: 10.1063/1.473582. URL `http://link.aip.org/link/?JCP/106/5615/1`.

[120] R. D. Groot and P. B. Warren. Dissipative particle dynamics: Bridging the gap between atomistic and mesoscopic simulation. *Journal of Chemical Physics*, 107(11):4423–4435, September 1997.

[121] V. Pryamitsyn and V. Ganesan. A coarse-grained explicit solvent simulation of rheology of colloidal suspensions. *Journal of Chemical Physics*, 122(10):104906, March 2005.

[122] V. Pryamitsyn and V. Ganesan. Origins of linear viscoelastic behavior of polymer-nanoparticle composites. *Macromolecules*, 39(2):844–856, January 2006.

[123] M. P. Allen and D. J. Tildesley. *Computer Simulation of Liquids*. Oxford, 2006.

[124] P.-G. de Gennes. *Scaling Concepts in Polymer Physics*. Oxford University Press, 1979.

[125] P.-G. de Gennes. *C. R. Hebd. Seances Acad. Sci., Ser. A B, Sci. Math. Sci. Phys*, 288:359, 1979.

[126] J. F. Joanny, L. Leibler, and de Gennes P.-G. *Polym. Sci., Polym. Phys. Ed.*, 17:1073, 1979.

[127] E. J. Meijer and D. Frenkel. Computer-simulation of polymer-induced clustering of colloids. *Physical Review Letters*, 67(9):1110–1113, August 1991.

[128] A. Hanke, E. Eisenriegler, and S. Dietrich. Polymer depletion effects near mesoscopic particles. *Physical Review E*, 59(6):6853–6878, June 1999.

[129] T. Odijk. Protein-macromolecule interactions. *Macromolecules*, 29(5): 1842–1843, February 1996.

[130] M. Fuchs and K. S. Schweizer. Structure of colloid-polymer suspensions. *Journal of Physics-condensed Matter*, 14(12):R239–R269, April 2002.

[131] R. R. Netz and J. F. Joanny. Complexation between a semiflexible polyelectrolyte and an oppositely charged sphere. *Macromolecules*, 32 (26):9026–9040, December 1999.

[132] Y. Mao, P. Bladon, H. N. W. Lekkerkerker, and M. E. Cates. Density profiles and thermodynamics of rod-like particles between parallel walls. *Molecular Physics*, 92(1):151–159, September 1997.

[133] Y. Mao, M. E. Cates, and H. N. W. Lekkerkerker. Theory of the depletion force due to rodlike polymers. *Journal of Chemical Physics*, 106(9):3721–3729, March 1997.

[134] Y. L. Chen and K. S. Schweizer. Depletion interactions in suspensions of spheres and rod-polymers. *Journal of Chemical Physics*, 117(3):1351–1362, July 2002.

[135] Y. L. Chen and K. S. Schweizer. Collective structure and dynamics in dense colloid-rod polymer suspensions. *Langmuir*, 18(20):7354–7363, October 2002.

[136] D. W. SCHAEFER, J. F. JOANNY, D. W. PINCUS, P. Schaefer, J. F. Joanny, and P. Pincus. Dynamics of semiflexible polymers in solution. *Macromolecules*, 13(5):1280–1289, 1980.

[137] A. N. Semenov. Adsorption of a semiflexible wormlike chain. *European Physical Journal E*, 9(4):353–363, November 2002.

[138] N. L. Abbott, D. Blankschtein, and T. A. Hatton. Protein partitioning in 2-phase aqueous polymer systems .1. novel physical pictures and a scaling-thermodynamic formulation. *Macromolecules*, 24(15):4334–4348, July 1991.

[139] E. W. Merrill, K. A. Dennison, and C. Sung. Partitioning and diffusion of solutes in hydrogels of poly(ethylene oxide). *Biomaterials*, 14(15): 1117–1126, December 1993.

[140] B. Amsden. Solute diffusion within hydrogels. mechanisms and models. *Macromolecules*, 31(23):8382–8395, November 1998.

[141] K. Lubyphelps. Physical-properties of cytoplasm. *Current Opinion In Cell Biology*, 6(1):3–9, February 1994.

[142] R. J. Phillips, W. M. Deen, and J. F. Brady. Hindered transport of spherical macromolecules in fibrous membranes and gels. *Aiche Journal*, 35(11):1761–1769, November 1989.

[143] M. W. Matsen. Melts of semiflexible diblock copolymer. *Journal of Chemical Physics*, 104(19):7758–7764, May 1996.

[144] A. J. Spakowitz and Z. G. Wang. Semiflexible polymer solutions. i. phase behavior and single-chain statistics. *Journal of Chemical Physics*, 119 (24):13113–13128, December 2003.

[145] N. Saito, K. Takahashi, and Y. Yunoki. Statistical mechanical theory of stiff chains. *Journal of the Physical Society of Japan*, 22(1):219, 1967.

[146] G. H. Fredrickson. *The Equilibrium Theory of Inhomogeneous Polymers.* Oxford University Press, Oxford, 2006.

[147] M. Doi and S. Edwards. *The Theory of Polymer Dynamics.* Oxford University Press, Oxford, 1986.

[148] G. H. Fredrickson, V. Ganesan, and F. Drolet. Field-theoretic computer simulation methods for polymers and complex fluids. *Macromolecules,* 35(1):16–39, January 2002.

[149] M. Surve, V. Pryamitsyn, and V. Ganesan. Depletion and pair interactions of proteins in polymer solutions. *Journal of Chemical Physics,* 122 (15):154901, April 2005.

[150] G. J. Fleer, A. M. Skvortsov, and R. Tuinier. Mean-field equation for the depletion thickness. *Macromolecules,* 36(20):7857–7872, October 2003.

[151] J. D. Jackson. *Classical Electrodynamics.* Wiley, New York, 1975.

[152] F. Drolet and G. H. Fredrickson. Combinatorial screening of complex block copolymer assembly with self-consistent field theory. *Physical Review Letters,* 83(21):4317–4320, November 1999.

[153] W. H. Press, B. P. Flannery, S. A. Teukolsky, and W. T. Vetterling. *Numerical Recipes in C: The Art of Scientific Computing, 2nd Ed.* Cambridge University Press, Cambridge, 1992.

[154] R. J. LeVeque. *Numerical Methods for Conservation Laws.* Birkauser-Verlag, Basel, 1992.

[155] T. Shimada, M. Doi, and K. Okano. Concentration fluctuation of stiff polymers .3. spinodal decomposition. *Journal of Chemical Physics,* 88 (11):7181–7186, June 1988.

[156] C. M. Marques and G. H. Fredrickson. Rigid gaussian chains i: the scattering function. *Journal De Physique Ii*, 7(12):1805–1816, December 1997.

[157] P. Friedel, A. John, D. Pospiech, D. Jehnichen, and R. R. Netz. Modelling of the phase separation behaviour of semiflexible diblock copolymers. *Macromolecular Theory and Simulations*, 11(7):785–793, October 2002.

[158] J. S. Rowlinson. *Molecular Theory of Capillarity*. Clarendon Press, Oxford, 1982.

[159] J. C. Maxwell. *A Treatise on Electricity and Magnetism*. Clarendon Press, Oxord, 1873.

[160] S. Torquato. *Random Heterogeneous Materials: Microstructure and Macroscopic Properties*. Springer, 2002.

[161] S. Whitaker. *The Method of Volume Averaging (Theory and Applications of Transport in Porous Media)*. Springer, 1998.

[162] T. C. Choy. *Effective Medium Theory: Principles and Applications*. Oxford University Press, 1999.

[163] T. C. Merkel, L. G. Toy, A. L. Andrady, H. Gracz, and E. O. Stejskal. Investigation of enhanced free volume in nanosilica-filled poly(1-trimethylsilyl-1-propyne) by xe-129 nmr spectroscopy. *Macromolecules*, 36(2):353–358, January 2003.

[164] L. S. Schandler, L. C. Brinson, and W. G. Sawyer. Polymer nanocomposites: A small part of the story. *Jom*, 59(3):53–60, March 2007.

[165] D. W. Schaefer and R. S. Justice. How nano are nanocomposites? *Macromolecules*, 40(24):8501–8517, November 2007.

[166] M. Alcoutlabi and G. B. McKenna. Effects of confinement on material behaviour at the nanometre size scale. *Journal of Physics-condensed Matter*, 17(15):R461–R524, April 2005.

[167] R. A. L. Jones. The dynamics of thin polymer films. *Current Opinion In Colloid & Interface Science*, 4(2):153–158, April 1999.

[168] Y. Huang and D. R. Paul. Effect of film thickness on the gas-permeation characteristics of glassy polymer membranes. *Industrial & Engineering Chemistry Research*, 46(8):2342–2347, April 2007.

[169] R. D. Priestley, L. J. Broadbelt, and J. M. Torkelson. Physical aging of ultrathin polymer films above and below the bulk glass transition temperature: Effects of attractive vs neutral polymer-substrate interactions measured by fluorescence. *Macromolecules*, 38(3):654–657, February 2005.

[170] C. M. Stafford, B. D. Vogt, C. Harrison, D. Julthongpiput, and R. Huang. Elastic moduli of ultrathin amorphous polymer films. *Macromolecules*, 39(15):5095–5099, July 2006.

[171] R. Auras, B. Harte, and S. Selke. An overview of polylactides as packaging materials. *Macromolecular Bioscience*, 4(9):835–864, September 2004.

[172] J. M. S. Henis and M. K. Tripodi. The developing technology of gas separating membranes. *Science*, 220(4592):11–17, 1983.

[173] W. J. Koros and G. K. Fleming. Membrane-based gas separation. *Journal of Membrane Science*, 83(1):1–80, August 1993.

[174] S. A. Stern. Polymers for gas separations - the next decade. *Journal of Membrane Science*, 94:1–65, September 1994.

[175] R. W. Baker. Future directions of membrane gas separation technology. *Industrial & Engineering Chemistry Research*, 41(6):1393–1411, March 2002.

[176] R. M. Barrer, J. A. Barrie, and M. G. Rogers. Heterogeneous membranes: Diffusion in filled rubber. *J. Polym. Sci., Part A*, 1:2565–2586, 1963.

[177] J. E. Bara, A. K. Kaminski, R. D. Noble, and D. L. Gin. Influence of nanostructure on light gas separations in cross-linked lyotropic liquid crystal membranes. *Journal of Membrane Science*, 288(1-2):13–19, February 2007.

[178] T. Yamaguchi, L. M. Boetje, C. A. Koval, R. D. Noble, and C. N. Bowman. Transport-properties of carbon-dioxide through amine functionalized carrier membranes. *Industrial & Engineering Chemistry Research*, 34(11):4071–4077, November 1995.

[179] S. Bai, S. Sridhar, and A. A. Khan. Metal-ion mediated separation of propylene from propane using ppo membranes. *Journal of Membrane Science*, 147(1):131–139, August 1998.

[180] J. H. Petropoulos. A comparative-study of approaches applied to the permeability of binary composite polymeric materials. *Journal of Polymer Science Part B-polymer Physics*, 23(7):1309–1324, 1985.

[181] W. R. Falla, M. Mulski, and E. L. Cussler. Estimating diffusion through flake-filled membranes. *Journal of Membrane Science*, 119(1):129–138, October 1996.

[182] G. H. Fredrickson and J. Bicerano. Barrier properties of oriented disk composites. *Journal of Chemical Physics*, 110(4):2181–2188, January 1999.

[183] J. Y. Ahn, W. J. Chung, I. Pinnau, and M. D. Guiver. Poly sulfone/silica

nanoparticle mixed-matrix membranes for gas separation. *Journal of Membrane Science*, 314(1-2):123–133, April 2008.

[184] P. Winberg, K. Desitter, C. Dotremont, S. Mullens, I. F. J. Vankelecom, and F. H. J. Maurer. Free volume and interstitial mesopores in silica filled poly(i-trimethylsilyl-l-propyne) nanocomposites. *Macromolecules*, 38(9):3776–3782, May 2005.

[185] D. Gomes, S. P. Nunes, and K. V. Peinemann. Membranes for gas separation based on poly(1-trimethylsilyl-1-propyne)-silica nanocomposites. *Journal of Membrane Science*, 246(1):13–25, January 2005.

[186] S. Matteucci, R. D. Raharjo, V. A. Kusuma, S. Swinnea, and B. D. Freeman. Gas permeability, solubility, and diffusion coefficients in 1,2-polybutadiene containing magnesium oxide. *Macromolecules*, 41(6): 2144–2156, March 2008.

[187] R. Landauer. The electrical resistance of binary metallic mixtures. *J. Appl. Phys.*, 23:779, 1952.

[188] C. M. Zimmerman, A. Singh, and W. J. Koros. Tailoring mixed matrix composite membranes for gas separations. *Journal of Membrane Science*, 137(1-2):145–154, December 1997.

[189] L. J. Broutman and B. D. Agarwal. Theoretical study of effect of an interfacial layer on properties of composites. *Polymer Engineering and Science*, 14(8):581–588, 1974.

[190] T. T. Moore, R. Mahajan, D. Q. Vu, and W. J. Koros. Hybrid membrane materials comprising organic polymers with rigid dispersed phases. *Aiche Journal*, 50(2):311–321, February 2004.

[191] L. P. Xue, O. Borodin, and G. D. Smith. Modeling of enhanced penetrant diffusion in nanoparticle-polymer composite membranes. *Journal of Membrane Science*, 286(1-2):293–300, December 2006.

183

[192] R. J. Hill. Diffusive permeability and selectivity of nanocomposite membranes. *Industrial & Engineering Chemistry Research*, 45(21):6890–6898, October 2006.

[193] G. Tsagaropoulos and A. Eisenberg. Dynamic-mechanical study of the factors affecting the 2 glass-transition behavior of filled polymers - similarities and differences with random ionomers. *Macromolecules*, 28(18): 6067–6077, August 1995.

[194] B. J. Ash, L. S. Schadler, and R. W. Siegel. Glass transition behavior of alumina/polymethylmethacrylate nanocomposites. *Materials Letters*, 55(1-2):83–87, July 2002.

[195] A. Morisato and I. Pinnau. Synthesis and gas permeation properties of poly(4-methyl-2-pentyne). *Journal of Membrane Science*, 121(2):243–250, December 1996.

[196] T. Masuda, E. Isobe, T. Higashimura, and K. Takada. Poly[1-(trimethylsilyl)-1-propyne] - a new high polymer synthesized with transition-metal catalysts and characterized by extremely high gas-permeability. *Journal of the American Chemical Society*, 105(25):7473–7474, 1983.

[197] Y. Yampolskii, I. Pinnau, and B. D. Freemand, editors. *Materials Science of Membranes for Gas and Vapor Separation*. Wiley, 2006.

[198] T. C. Merkel, B. D. Freeman, R. J. Spontak, Z. He, I. Pinnau, P. Meakin, and A. J. Hill. Sorption, transport, and structural evidence for enhanced free volume in poly(4-methyl-2-pentyne)/fumed silica nanocomposite membranes. *Chemistry of Materials*, 15(1):109–123, January 2003.

[199] V. Ganesan, L. Khounlavong, and V. Pryamitsyn. Equilibrium characteristics of semiflexible polymer solutions near probe particles. *Physical Review E*, 78(5):051804, November 2008.

[200] O. Kratky and G. Porod. X-ray investigation of dissolved chain molecules. *Rec. Trav. Chim. Pay.*, 68:1106, 1949.

[201] E. Helfand and A. M. Sapse. Theory of unsymmetric polymer-polymer interfaces. *Journal of Chemical Physics*, 62(4):1327–1331, 1975.

[202] E. Helfand and Z. R. Wasserman. Block copolymer theory .5. spherical domains. *Macromolecules*, 11(5):960–966, 1978.

[203] D. J. Jeffrey. Conduction through a random suspension of spheres. *Proceedings of the Royal Society of London Series A-mathematical Physical and Engineering Sciences*, 335(1602):355–367, 1973.

[204] G. K. Batchelor. Transport properties of two-phase materials with random structure. *Annu. Rev. Fluid Mech.*, 6:227–255, 1974.

[205] H. Liu and L. C. Brinson. A hybrid numerical-analytical method for meodling the viscoelastic properties of polymer nanocomposites. *J. Appl. Mech.*, 73:758–768, 2006.

[206] R. Tuinier, G. A. Vliegenthart, and H. N. W. Lekkerkerker. Depletion interaction between spheres immersed in a solution of ideal polymer chains. *Journal of Chemical Physics*, 113(23):10768–10775, December 2000.

[207] M. H. Cohen and D. Turnbull. Molecular transport in liquids and glasses. *J. Chem. Phys.*, 31:1164–1169, 1959.

[208] C. D. Van Siclen. Walker diffusion method for calculation of transport properties of composite materials. *Physical Review E*, 59(3):2804–2807, March 1999.

[209] I. C. Kim and S. Torquato. Determination of the effective conductivity of heterogeneous media by brownian-motion simulation. *Journal of Applied Physics*, 68(8):3892–3903, October 1990.

[210] S. Torquato, I. C. Kim, and D. Cule. Effective conductivity, dielectric constant, and diffusion coefficient of digitized composite media via first-passage-time equations. *Journal of Applied Physics*, 85(3):1560–1571, February 1999.

[211] I. C. Kim, D. Cule, and S. Torquato. Comment on "walker diffusion method for calculation of transport properties of composite materials". *Physical Review E*, 61(4):4659–4660, April 2000.

[212] R. A. Riggleman, G. Toepperwein, G. J. Papakonstantopoulos, J. L. Barrat, and J. J. de Pablo. Entanglement network in nanoparticle reinforced polymers. *Journal of Chemical Physics*, 130(24):244903, June 2009.

[213] G. J. Papakonstantopoulos, M. Doxastakis, P. F. Nealey, J. L. Barrat, and J. J. de Pablo. Calculation of local mechanical properties of filled polymers. *Physical Review E*, 75(3):031803, March 2007.

[214] C. Tzoumanekas and D. N. Theodorou. Topological analysis of linear polymer melts: A statistical approach. *Macromolecules*, 39(13):4592–4604, June 2006.

[215] M. Kroger. Shortest multiple disconnected path for the analysis of entanglements in two- and three-dimensional polymeric systems. *Computer Physics Communications*, 168(3):209–232, June 2005.

[216] M. Fuchs and K. S. Schweizer. Structure and thermodynamics of colloid-polymer mixtures: A macromolecular approach. *Europhysics Letters*, 51 (6):621–627, September 2000.

[217] M. Fuchs and K. S. Schweizer. Macromolecular theory of solvation and structure in mixtures of colloids and polymers. *Physical Review E*, 64 (2):021514, August 2001.

Vita

Youthachack Landry Khounlavong was born in Florida, and is the son of Phanh and Evelyn Khounlavong. In the Fall of 2001, he began attendance at the University of Florida in Gainesville. He graduated summa cum laude with a Bachelors of Science in Chemical Engineering in the Spring of 2005. Following this, he began graduate school in the chemical engineering department at The University of Texas at Austin in the Fall of 2005. Here, he worked on his doctoral research under the guidance of Prof. Venkat Ganesan.

Permanent Address: 740 Delmonico St. NE

Palm Bay, FL 32907

This dissertation was typeset with $\text{\LaTeX}\,2_\varepsilon$[1] by the author.

---

[1]$\text{\LaTeX}\,2_\varepsilon$ is an extension of $\text{\LaTeX}$. $\text{\LaTeX}$ is a collection of macros for $\text{\TeX}$. $\text{\TeX}$ is a trademark of the American Mathematical Society. The macros used in formatting this dissertation were written by Dinesh Das, Department of Computer Sciences, The University of Texas at Austin, and extended by Bert Kay, James A. Bednar, and Ayman El-Khashab.